

**AEDC-TR-80-3**

# **Development of Mie Scattering Techniques for In-Situ Particle Diagnostics at AEDC**

**B. P. Curry, D. P. Weaver, and J. W. L. Lewis  
ARO, Inc.**

**November 1980**

**Final Report for Period October 1, 1978 — September 30, 1979**

**Property of U. S. Air Force  
AEDC LIBRARY  
F40600-81-C-0004**

**TECHNICAL REPORTS  
FILE COPY**

**Approved for public release, distribution unlimited.**

**ARNOLD ENGINEERING DEVELOPMENT CENTER  
ARNOLD AIR FORCE STATION, TENNESSEE  
AIR FORCE SYSTEMS COMMAND  
UNITED STATES AIR FORCE**

## NOTICES

When U. S. Government drawings, specifications, or other data are used for any purpose other than a definitely related Government procurement operation, the Government thereby incurs no responsibility nor any obligation whatsoever, and the fact that the Government may have formulated, furnished, or in any way supplied the said drawings, specifications, or other data, is not to be regarded by implication or otherwise, or in any manner licensing the holder or any other person or corporation, or conveying any rights or permission to manufacture, use, or sell any patented invention that may in any way be related thereto.

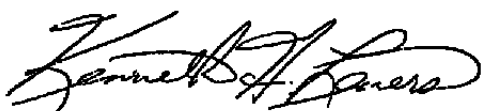
Qualified users may obtain copies of this report from the Defense Technical Information Center.

References to named commercial products in this report are not to be considered in any sense as an indorsement of the product by the United States Air Force or the Government.

This report has been reviewed by the Office of Public Affairs (PA) and is releasable to the National Technical Information Service (NTIS). At NTIS, it will be available to the general public, including foreign nations.

## APPROVAL STATEMENT

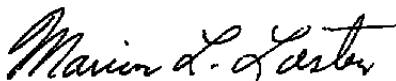
This report has been reviewed and approved.



KENNETH H. LENERS, Captain, USAF  
Project Manager, Research Division  
Directorate of Technology

Approved for publication:

FOR THE COMMANDER



MARION L. LASTER  
Director of Technology  
Deputy for Operations

# UNCLASSIFIED

REPORT DOCUMENTATION PAGE		READ INSTRUCTIONS BEFORE COMPLETING FORM												
1 REPORT NUMBER <b>AEDC-TR-80-3</b>	2 GOVT ACCESSION NO.	3 RECIPIENT'S CATALOG NUMBER												
4 TITLE (and Subtitle) <b>DEVELOPMENT OF MIE SCATTERING TECHNIQUES FOR IN-SITU PARTICLE DIAGNOSTICS AT AEDC</b>		5 TYPE OF REPORT & PERIOD COVERED <b>Final Report--October 1, 1978 to September 30, 1979</b>												
7 AUTHOR(s) <b>B. P. Curry, D. P. Weaver, and J. W. L. Lewis, ARO, Inc., a Sverdrup Corporation Company</b>		6 PERFORMING ORG REPORT NUMBER												
9 PERFORMING ORGANIZATION NAME AND ADDRESS <b>Arnold Engineering Development Center/DOT Air Force Systems Command Arnold Air Force Station, Tennessee 37389</b>		8 CONTRACT OR GRANT NUMBER(s)												
11 CONTROLLING OFFICE NAME AND ADDRESS <b>Arnold Engineering Development Center/DOS Air Force Systems Command Arnold Air Force Station, Tennessee 37389</b>		10 PROGRAM ELEMENT, PROJECT, TASK AREA & WORK UNIT NUMBERS <b>Program Elements 65807F and 62302</b>												
14 MONITORING AGENCY NAME & ADDRESS (if different from Controlling Office)		12 REPORT DATE <b>November 1980</b>												
		13 NUMBER OF PAGES <b>90</b>												
		15 SECURITY CLASS. (of this report) <b>UNCLASSIFIED</b>												
		15a DECLASSIFICATION/DOWNGRADING SCHEDULE <b>N/A</b>												
16 DISTRIBUTION STATEMENT (of this Report)  <b>Approved for public release; distribution unlimited.</b>														
17 DISTRIBUTION STATEMENT (of the abstract entered in Block 20, if different from Report)														
18 SUPPLEMENTARY NOTES  <b>Available in Defense Technical Information Center (DTIC)</b>														
19. KEY WORDS (Continue on reverse side if necessary and identify by block number) <table style="width: 100%; border: none;"> <tr> <td style="width: 33%;">mathematical analysis</td> <td style="width: 33%;">distribution</td> <td style="width: 33%;">density</td> </tr> <tr> <td>particulates</td> <td>chemical composition</td> <td>Mie scattering</td> </tr> <tr> <td>flow</td> <td>histograms</td> <td>computer programs</td> </tr> <tr> <td>particle size</td> <td>refractive indices</td> <td></td> </tr> </table>			mathematical analysis	distribution	density	particulates	chemical composition	Mie scattering	flow	histograms	computer programs	particle size	refractive indices	
mathematical analysis	distribution	density												
particulates	chemical composition	Mie scattering												
flow	histograms	computer programs												
particle size	refractive indices													
20 ABSTRACT (Continue on reverse side if necessary and identify by block number) <p>Various experimental and analytical techniques have been developed at Arnold Engineering Development Center (AEDC) for diagnosing particulate-laden flows with very rapid time resolution. These procedures allow determining the average particle size, the distribution of particles by chemical species, and the size distribution histograms for single particle species with known complex refractive indices. If transmission measurements are made,</p>														

# UNCLASSIFIED

**UNCLASSIFIED**

**20. ABSTRACT (Continued)**

then the particle number density average along the line of sight can be determined as well. This report describes these particle diagnostic procedures and discusses some of their applications to specific Air Force needs.

**UNCLASSIFIED**

## PREFACE

The work reported herein was conducted by ARO Inc., AEDC Division (a Sverdrup Corporation Company), operating contractor for the AEDC, AFSC, Arnold Air Force Station, Tennessee. This work was done under ARO Project Nos. P32M-01 and P34M-26. Project P32M-01 was sponsored by the AEDC/DOTR, and the Air Force project manager was Capt. Kenneth Leners. Project P34M-26 was sponsored by the Air Force Rocket Propulsion Laboratory (AFRPL), and the AFRPL project manager was Dr. T. D. McCay.

The authors express their appreciation to L. C. Voorhees, D. A. Waldrop, J. H. Jones, and W. E. Dorrel of ARO, Inc., for programming and computational assistance and to N. W. Wright for experimental assistance during the course of the work reported herein.

## CONTENTS

	<u>Page</u>
<b>1.0 INTRODUCTION</b>	
1.1 Review of AEDC Mie Scattering Particle Diagnostics Applications . . . . .	7
1.2 Summary of AEDC Mie Scattering Particle Diagnostic Methods . . . . .	8
<b>2.0 THEORY</b>	
2.1 Background . . . . .	9
2.2 Measurement of the Average Size Parameter Using the Mie Scattering Functions . . . . .	11
<b>3.0 SIZE DECONVOLUTION ANALYSIS . . . . .</b>	17
<b>4.0 AVERAGE SIZE AND SPECIES MOLE FRACTION     DETERMINATION FOR A PARTICLE MIXTURE . . . . .</b>	18
<b>5.0 CONCLUDING REMARKS . . . . .</b>	22
<b>REFERENCES . . . . .</b>	22

## ILLUSTRATIONS

### Figure

1. Comparison of Mie Theory with Experimental Scattered Light Intensity from Monodisperse Polystyrene Latex Spheres in Water Suspension (from Ref. 4) . . . . .	25
2. Comparison of Mie Theory with Experimental Scattered Light Intensity from a Narrow Polydispersion of Spherical Aerosols . . . . .	26
3. Mie Scattering Experimental Configuration Similar to that Used in the AFRPL BATES Motor Tests . . . . .	27
4. Flow Chart of AEDC Mie Scattering Particle Diagnostics Program . . . . .	28
5. Spherical Coordinate Geometry for the Multiangular Scattering of Light by a Dielectric Sphere . . . . .	29
6. Size Dependence of the Degree of Polarization of Light Scattered by Water Droplets in the Geometry of Ref. 3 . . . . .	30
7. Size Dependence of ANGER Functions for Iron in the Geometry of Ref. 3 . . . . .	31
8. Size Dependence of the Extinction Cross Sections for Copper Particles and Iron Particles: 0.5145- $\mu$ Light . . . . .	32
9. Size Dependence of the Extinction Efficiencies for Carbon Soot and Calcite: Visible Light . . . . .	33

<u>Figure</u>	<u>Page</u>
10. Size Dependence of the Backscattering Efficiencies for Carbon Soot and Calcite: Visible Light . . . . .	34
11. Dependence of Backscattering Efficiency on Modal Diameter for Polydisperse Soot Particles at Visible and Infrared Wavelengths . . . . .	35
12. Effect of Absorptive Index on Size Dependence of ANGER Functions for Copper (Perpendicular Polarization) in the Geometry of Ref. 3 . . . . .	36
13. Size Dependence of the Degree of Polarization of Light Scattered by Copper Spheres in the Geometry of Ref. 3 . . . . .	37
14. Size Dependence of the Degree of Polarization of Light Scattered by Iron Spheres in the Geometry of Ref. 3 . . . . .	38
15. Effect of Collection Optics Subtended Solid Angle on Size Dependence of the Degree of Polarization for Light Scattering from $Al_2O_3$ Spheres at 90-deg Scattering Angle and Incident Polarization Parallel to the Scattering Plane . . . . .	39
16. Size Dependence of the Parallel Mie Scattering Intensity Functions in the Geometry of Ref. 7 . . . . .	40
17. Size Dependence of the Perpendicular Mie Scattering Intensity Functions in the Geometry of Ref. 7 . . . . .	41
18. Size Dependence of the Degree of Polarization of Light Scattered by Very Small Droplets in the Geometry of Ref. 7 . . . . .	42

## APPENDIXES

A. SIZFRED: A Computer Program for Size Distribution Deconvolution by Fredholm Inversion of Mie Scattering Data . . . . .	43
B. Measurement of Particle Sizes and Complex Refractive Indices by Use of Mie Scattering Techniques (Paper Presented at Smoke Symposium II, Harry Diamond Laboratory, Adelphi, Md., April 25-26, 1978) . . . . .	77
NOMENCLATURE . . . . .	87

## 1.0 INTRODUCTION

Rapid, time-resolved diagnostics of various particle-laden flows are of much importance in specific Air Force applications. In aerodynamic simulation facilities, the presence of dust, dirt, erosion products, and condensate can adversely affect both the operation of the test facilities and the interpretation of measurements made in those facilities. For such activities, knowledge of the particle size distribution function (PSDF) is valuable. Occasionally, the presence of natural particulate matter in a test facility is desirable, as is the case when using laser velocimetry to determine the velocity in unseeded flow fields. Even then, a knowledge of the PSDF is required to characterize the gas-particle interaction and, especially, to indicate whether the particles being observed can be expected to follow the flow sufficiently well to permit accurate measurements.

Rocket exhaust diagnostics and spacecraft contamination studies also require a known PSDF and particle number density within local flow regions. In the case of rocket exhausts, it is desirable to know the total number density, chemical species distribution, and the PSDF of the particulate effluent (1) to understand primary and secondary smoke formation and to validate prediction models of these phenomena and (2) to characterize the particulate exhaust effluents of both liquid- and solid-propellant rockets. Such characterization is required to assess the contaminant potential of such effluents.

Also, the diagnostic techniques discussed in this report provide a unique means of studying one of the most important and least understood aspects of two-phase flow fields — the formation of liquid droplets and small solid particles from the primitive molecular clusters (dimers, trimers, tetramers, and so forth) which can sometimes result in massive condensation in hypersonic flow expansions.

Before the development program discussed in this report was begun, it was decided that the proposed diagnostics scheme should meet the following requirements:

1. The technique should not be restricted to the requirement that a single particle be present in the focal volume, but, rather, the method should be capable of yielding accurate results when a polydisperse size distribution is present.
2. Both average particle sizes and PSDF's should be obtainable from the technique, and submicron particles should be measurable.
3. Time resolution should be possible to within milliseconds.



4. It should be possible to evaluate uncertainties in the measurements and to estimate the quantitative effect of measurement imprecision on the particle size results.
5. Insofar as possible, the technique should require only standard laser sources and detectors (rather than requiring dramatic advances in the state of the art of optical and electronic instrumentation).
6. The technique should not require absolute intensity measurements.
7. Although originally intended to size particles of a single chemical species with known complex indices of refraction, the technique should be capable of generalization (1) to the measurement of the PSDF of a single species of unknown refractive index and (2) to the determination of effective complex refractive indices for a particle mixture whose chemical identities are not known a priori. In addition to the latter, the technique should permit the deconvolution of both particle species and size distributions.

To satisfy these requirements, it was decided that the program of particle diagnostics should be based on multiangular or multispectral Mie scattering measurements or, perhaps, on a combination of both types of measurements. Although only the multiangular measurements and analyses have been used, the combination of measurements may well be required by some future applications. Mie scattering measurements have a distinct advantage over measurements based on more approximate analysis schemes, since the Mie theory is an exact solution for the polarized, single scattering of light by a dielectric sphere of arbitrary size. However, the optical depth for Mie scattering must be small enough to ensure that multiple-scattering events contribute no more than from approximately 10 to 20 percent to the scattering signal at any given detector location. Also, departure from sphericity affects the accuracy of interpretation of the polarized measurements in the backscattering hemisphere. In addition, the refractive indices of the measured particles must be known or be iteratively determinable within the sizing analysis procedure. Various procedures exist to approximate nonspherical scatterers, and an assessment of their use, in conjunction with the sizing procedures discussed in this report, is underway. However, a complete assessment of the effects of nonspherical scattering is beyond the scope of this report; the results discussed pertain only to scattering from spheres. Subsequent sections of this report describe and summarize the analytical procedures that have been developed or extended at AEDC for Mie scattering PSDF determinations.

## 1.1 REVIEW OF AEDC MIE SCATTERING PARTICLE DIAGNOSTICS APPLICATIONS

The development of the particle diagnostic procedures occurred in several stages, the first of which was the development of a comprehensive Mie angular scattering computer code (Ref. 1) that was based on routines reported in Ref. 2. To be applied to particle diagnostics problems at AEDC, the program had to be modified in several ways; consequently, a family of codes, collectively known as MIESTEP, was generated. These codes compute, plot, and store on tape files the Mie scattering functions, which are integrated over specified angles, and ancillary scattering functions for a specified range of size parameters. These analytical procedures and a primitive version of the size deconvolution code discussed in Appendix A were used to analyze Mie scattering data obtained in the particulate-laden flow of an arc-driven hypervelocity wind tunnel at AEDC. These results, reported in Ref. 3 and Appendix B, established the average particle size, a four-bin histogram approximation to the PSDF, and the particle number density of these submicron particles. Also, the results obtained with the measurements and analysis procedure were used to eliminate water and iron as possible dominant scattering species and to establish limits for the mass fractions of the dominant scatterers, which were copper and tungsten produced by the arc. Furthermore, these results were consistent with a posttest chemical analysis of electrode weight loss (See Appendix B.)

After this successful application of Mie scattering principles to particle diagnostics in an AEDC test facility, a series of laboratory measurements of the scattering from a suspension of polystyrene spheres was made at both single- and multiple-scattering conditions. The purpose of this work [performed under the sponsorship of the Air Force Rocket Propulsion Laboratory (AFRPL) and reported in Ref. 4] was to validate a multiple-scattering code that was developed by an AFRPL contractor, under conditions of simulated scattering from solid-propellant rocket motor (SRM) plumes. Figure 1, taken from Ref. 4, shows the agreement of Mie theory with the single-scattering, monodisperse scattering data obtained in Ref. 4. Figure 2 shows a similar comparison to results that were reported in Ref. 5 and that were obtained from a narrow, log-normal distribution of spherical aerosols.

Also, a series of flow visualization measurements was made for the MIT Lincoln Laboratory under the sponsorship of the Air Force Space and Missile Systems Organization (SAMSO). These experiments (reported in Ref. 6) involved using an image intensifier to permit high-speed photography of the flow field surrounding particles ejected from a model into a hypervelocity flow field. Although Mie scattering sizing measurements were not made, Mie calculations based on approximate and independent pretest size measurements permitted the quantitative interpretation of isointensity

contours (obtained with computerized densitometry of the photographs of the image-intensifier surface) as contours of constant particle number densities.

One of the procedures was applied to sizing particles with diameters of about  $0.1\ \mu$  in conjunction with tests of a small liquid-bipropellant thruster. An image intensifier, located at a 90-deg scattering angle, was used for flow visualization of a laser-illuminated exhaust plume. Analysis of the degree-of-polarization of the scattering signal yielded a quantitative measure of the order of magnitude of the particle size of the exhaust. These results were reported in Ref. 7.

The particle diagnostics procedures discussed in this report are also currently being applied in the BATES motor test program at the AFRPL. These measurements of the exhaust plumes of SRM's are being made with various diagnostics techniques, one of which is a Mie scattering determination of the PSDF involving the experimental configuration shown in Fig. 3. Data obtained from these experiments will be analyzed using the size deconvolution procedures presented in this report. Computer simulations indicate that six-bin histograms of the PSDF having acceptable accuracy can be obtained if the imprecision in the scattering ratios (which are inputs to the deconvolution procedure) can be restricted to average values (for all the scattering channels) no larger than approximately  $\pm 3$  percent. A larger input imprecision of, for example,  $\pm 5$  percent will reduce the attainable size resolution to no more than five size bins, which span the range of diameters from less than  $0.1$  to approximately  $1.6\ \mu$ .

## 1.2 SUMMARY OF AEDC MIE SCATTERING PARTICLE DIAGNOSTIC METHODS

Before detailing the parameters that are determined by the AEDC particle diagnostic procedure, it is worthwhile to summarize the present form of the particle diagnostics approach and options; Fig. 4 is a flow chart of these procedures. Figure 4 shows that several parallel paths provide a degree of redundancy in particle diagnostics. Measurements made at several scattering angles of both the degree of polarization and of a set of functions, called ANGER functions (Angular/Extinction Ratios), provide a means of estimating a weighted average particle size, which, if the PSDF is not determined, is to be interpreted as a surface mean diameter.

The lower half of the flow chart indicates the procedures used for deconvolving the PSDF. Input scattering ratios (DECRATS) are used to deconvolve the PSDF in a histogram representation. The computer program that accomplishes this deconvolution is detailed in Appendix A. Outputs from the deconvolution histogram can be used as initial guesses to perform regression procedures currently under development. These procedures will permit reconstructing the normalized PSDF as one of the following three

single-mode, parametric size distributions: (1) a three-parameter, Deirmendjian modified-gamma distribution (Ref. 8); (2) a two-parameter, log-normal distribution; and (3) a two-parameter, truncated Gaussian distribution that is normalized on a semi-infinite size interval. If the size deconvolution histogram indicates the occurrence of either a bimodal or a higher-order, multimodal distribution, then these direct regression procedures are generally inappropriate.

Determining the average diameter or the PSDF permits estimating the total particle number density by convolving the computed extinction cross-section and transmission measurements. This method for measuring the particle number density is discussed in Ref. 3.

## 2.0 THEORY

### 2.1 BACKGROUND

The Mie scattering theory is detailed in many textbooks on optics or electromagnetic theory; Refs. 9 through 11 are especially useful. To understand the properties of the scattering ratios used in the AEDC particle diagnostics program, one must first consider the application of Mie theory to the interpretation of light-scattering measurements.

First, one should consider the angular distribution of single scattering of polarized radiation that is incident on a monodisperse distribution of particles of diameter  $D$ . If the incident beam power is  $\Phi_0$ , then flux, which is scattered with polarization vector perpendicular to the plane of scattering into a given solid angle subtended by the detection optics scheme, is written as follows:

$$\Phi_1(\theta_i, \psi_i, x, \eta) = \Phi_0 \int_0^\ell n(x, \ell') \int_{\psi_i - \Delta\psi_i/2}^{\psi_i + \Delta\psi_i/2} \int_{\theta_i - \Delta\theta_i/2}^{\theta_i + \Delta\theta_i/2} \frac{d\sigma_1}{d\Omega}(x, \theta, \psi, \eta) \sin \theta d\theta d\psi d\ell' \quad (1)$$

It is assumed that the incident beam is along the z-axis and that the incident polarization direction is the x-axis (see Fig. 5). The parallel polarization component is described by

$$\Phi_2(\theta_i, \psi_i, x, \eta) = \Phi_0 \int_0^\ell n(x, \ell') \int_{\psi_i - \Delta\psi_i/2}^{\psi_i + \Delta\psi_i/2} \int_{\theta_i - \Delta\theta_i/2}^{\theta_i + \Delta\theta_i/2} \frac{d\sigma_2}{d\Omega}(x, \theta, \psi, \eta) \sin \theta d\theta d\psi d\ell' \quad (2)$$

In these equations the solid angle,  $\Delta\Omega$ , subtended by the detector at the scattering volume of length  $\ell$  is given by

$$\Delta\Omega = \sin\theta \Delta\theta \Delta\psi$$

One more equation completes the set of equations that describes the single scattering and attenuation by spheres\*. The transmitted flux is given by

$$\Phi_{Tr}(x, \eta)/\Phi_0 = \exp\left[-\int_0^{\tilde{L}} n(x, \ell) \sigma_{ext}(x, \eta) d\ell\right] \equiv T(x, \eta) \quad (3)$$

where  $\sigma_{ext}$  is the total extinction cross section

$$\sigma_{ext}(x, \eta) = \sigma_{scat}(x, \eta) + \sigma_{abs}(x, \eta)$$

and  $\tilde{L}$  is the total distance over which scattering and absorption occur. The total scattering cross section is the integral of the differential cross section for scattering unpolarized light over the entire spherical solid angle,  $4\pi$  sr; i.e.,

$$\sigma_{scat}(x, \eta) = \int_0^{4\pi} \frac{d\sigma_U}{d\Omega}(x, \theta, \psi, \eta) d\Omega$$

where

$$\frac{d\sigma_U}{d\Omega} = \frac{d\sigma_1}{d\Omega} + \frac{d\sigma_2}{d\Omega}$$

The absorption cross section and the total scattering cross section are the products of the particle's geometric cross section,  $\pi(D/2)^2$ , and the dimensionless scattering and absorption efficiency factors,  $Q_{scat}$  and  $Q_{abs}$ , respectively. These two analytical functions are obtained directly (as functions of particle size and complex refractive index) from the Mie scattering series solution, without the need for numerical integration. It should be noted that Eqs. (1) through (3) have been written in terms of the dimensionless size parameter  $x = \pi D/\lambda$ , where  $\lambda$  is the wavelength of the incident radiation. The size parameter is, obviously, the ratio of the particle circumference to the light wavelength.

The differential scattering cross sections are related to angular Mie intensity functions, which are obtained from the Mie scattering computer codes, according to

---

\*Only the first two Stokes parameters of scattered light — the intensity and the degree-of-polarization — are considered. For nonspherical scatterers, it may be necessary to measure the remaining two Stokes parameters, the ellipticity and orientation of the polarization ellipse. Such additional measurements are also desirable when dealing with multiple scattering. However, in this work, these additional complications are ignored.

$$\frac{d\sigma_1}{d\Omega}(\mathbf{x}, \theta, \psi, \eta) = i_1(\mathbf{x}, \theta, \eta) \sin^2 \psi / k^2 \quad (4)$$

and

$$\frac{d\sigma_2}{d\Omega}(\mathbf{x}, \theta, \psi, \eta) = i_2(\mathbf{x}, \theta, \eta) \cos^2 \psi / k^2 \quad (5)$$

where  $k = 2\pi/\lambda$  is the wave number of the incident light. In these equations,  $\eta = \eta_r - i\kappa$  is the complex index of refraction of the particle species relative to that of the medium in which they are embedded (in this case, air, whose index is unity).

When a polydispersion of sizes must be considered, Eqs. (1) through (3) should be replaced by analogous forms in which  $\partial n(\mathbf{x}, \ell)/\partial \mathbf{x}$  is substituted for  $n(\mathbf{x}, \ell)$ , and the right-hand sides of Eqs. (1) and (2), as well as the exponent of Eq. (3), are then integrated over the interval  $0 \leq x \leq \infty$ . Usually the scattering volume is sufficiently small that variations in number density and/or size distribution can be ignored through the distance  $\ell_i$  (the length of the focal volume corrected for viewing angle effects), in which case  $\partial n(\mathbf{x}, \ell)/\partial \mathbf{x}$  can be replaced in Eqs. (1) and (2) by  $nf(\mathbf{x})$ , where  $f(\mathbf{x})$  is the normalized size distribution function. The scattering length,  $\ell_i$ , is different for each angle [i.e.,  $\ell_i = \ell(\theta_i)$ ]. The number density,  $n$ , is taken to be the average of the particle number density throughout the scattering volume.

The essence of the AEDC Mie scattering technique is to measure and interpret suitably defined scattering ratios from which the computer-based analytical procedures can then deconvolve the particle size distribution and determine the average particle size and number density. The use of such ratios avoids the difficulty of estimating beforehand the (usually unknown) particle number density and avoids the attendant experimental difficulties associated with making accurate, absolute measurements of scattered radiation signals.

## 2.2 MEASUREMENT OF THE AVERAGE SIZE PARAMETER USING THE MIE SCATTERING FUNCTIONS

Several functional ratios can be formed that yield a measure, albeit ambiguous, of the average size parameter of a polydisperse PSDF. The degree-of-polarization function, an example of such a ratio, can be defined as

$$P(\theta_i, \psi_i, \bar{\mathbf{x}}, \eta) = \frac{\langle i_1(\bar{\mathbf{x}}, \theta_i, \eta) \rangle \langle \sin^2 \psi_i \rangle - \langle i_2(\bar{\mathbf{x}}, \theta_i, \eta) \rangle \langle \cos^2 \psi_i \rangle}{\langle i_1(\bar{\mathbf{x}}, \theta_i, \eta) \rangle \langle \sin^2 \psi_i \rangle + \langle i_2(\bar{\mathbf{x}}, \theta_i, \eta) \rangle \langle \cos^2 \psi_i \rangle} \quad (6)$$

where

$$\langle i_{1,2}(\bar{x}, \theta_i, \eta) \rangle = \int_{\theta_{i'}}^{\theta_{i''}} i_{1,2}(\bar{x}, \theta_i, \eta) \sin \theta \, d\theta \quad (7)$$

and

$$\left\langle \frac{\sin^2 \psi_i}{\cos^2 \psi_i} \right\rangle = \left( 1/\Delta\psi_i \right) \int_{\psi_{i'}}^{\psi_{i''}} \left( \frac{\sin^2 \psi}{\cos^2 \psi} \right) d\psi \quad (8)$$

The integration limits for  $\theta$  and  $\psi$  are defined as

$$\theta_{i''} = \theta_i + (\Delta\theta_i/2) \quad \theta_{i'} = \theta_i - (\Delta\theta_i/2)$$

and

$$\psi_{i''} = \psi_i + (\Delta\psi_i/2) \quad \psi_{i'} = \psi_i - (\Delta\psi_i/2)$$

where  $\sin \theta_i \Delta\theta_i \Delta\psi_i$  represents the included solid angle subtended by the collection system at the scattering volume. The resulting integrations for  $\langle \sin^2 \psi_i \rangle$ ,  $\langle \cos^2 \psi_i \rangle$  are given by

$$\langle \sin^2 \psi_i \rangle = \sin^2 \psi_i - (\cos 2\psi_i / 2\Delta\psi_i) (\sin \Delta\psi_i - \Delta\psi_i)$$

and

$$\langle \cos^2 \psi_i \rangle = \cos^2 \psi_i + (\cos 2\psi_i / 2\Delta\psi_i) (\sin \Delta\psi_i - \Delta\psi_i) \quad (8a)$$

Shown in Fig. 6 is the variation of  $P(\theta_i, \psi_i, \bar{x}, \eta)$  with size parameter  $\bar{x}$  for water ( $H_2O$ ) at two backscattering angles near the rainbow angle for  $H_2O$ . The azimuthal angle of  $\pi/4$  was assumed.

Comparison of Eqs. (1), (2), (4), and (5) with Eq. (6) shows that the experimentally determined degree-of-polarization,  $P^{\text{exp}}(\theta_i, \psi_i)$ , can be written as

$$P^{\text{exp}}(\theta_i, \psi_i) = \left[ \Phi_1(\theta_i, \psi_i) - \Phi_2(\theta_i, \psi_i) \right] / \left[ \Phi_1(\theta_i, \psi_i) + \Phi_2(\theta_i, \psi_i) \right] \quad (9)$$

If a value of  $P^{\text{exp}}$  is assumed  $(\theta_i, \psi_i)$ , for which the parenthetical parameters  $\bar{x}$  and  $\eta$  have been suppressed, it can be seen (Fig. 6) that ambiguity results in the determination

of  $\bar{x}$ . For example, if  $P^{\text{exp}}(\theta_i, \psi_i)$  were found to be 0.60 in Fig. 6a, the value of the measured size parameter would be 5.15, 5.48, 6.2, 6.75, 7.48, or 7.85. Another factor contributing to the uncertainty  $\Delta\bar{x}$  in the size parameter results from experimental uncertainties in the measured flux values,  $\Phi_{1,2}$ . Specifically, the uncertainty  $\delta P$  in  $P^{\text{exp}}(\theta_i, \psi_i)$ , resulting from uncertainties in the flux values, is given by

$$\delta P(\theta_i, \psi_i)/P(\theta_i, \psi_i) = 2(B/A) \left[ (\delta A/A)^2 + (\delta B/B)^2 \right]^{1/2} / \left[ 1 - (B/A)^2 \right] \quad (10)$$

where

$$A = \Phi_1(\theta_i, \psi_i)/\Phi_0$$

and

$$B = \Phi_2(\theta_i, \psi_i)/\Phi_0$$

Because the steepness of the oscillatory functions shown in Fig. 6 is greatly dependent on the three parameters  $\theta$ ,  $\bar{x}$ , and  $\eta$ , it is difficult to determine the exact relationship between the imprecision of the degree-of-polarization measurements and the propagated imprecision of the inferred average size parameter. Nevertheless, from the application described in Ref. 3, it was found that an imprecision in  $P$  of from approximately 10 to 15 percent resulted in a derived size parameter imprecision of from about 15 to 20 percent.

Because of the non-uniqueness demonstrated in Fig. 6 and because of the effect of propagated measurement imprecision, it is apparent that either additional angular measurements of the degree of polarization or additional, independent, measured ratios of the Mie functions are required to decrease the ambiguity in  $\bar{x}$ . Two such functions (ANGER) are the ratios formed by the polarization-specific, angular scattering signal and the transmission signal:

$$R_1 = \langle i_1(\bar{x}, \theta_i, \psi_i, \eta) \rangle / \bar{x}^2 Q_{\text{ext}}(\bar{x}, \eta) \quad (11)$$

and

$$R_2 = \langle i_2(\bar{x}, \theta_i, \psi_i, \eta) \rangle / \bar{x}^2 Q_{\text{ext}}(\bar{x}, \eta) \quad (12)$$

where

$$Q_{\text{ext}}(\bar{x}, \eta) = \sigma_{\text{ext}}(\bar{x}, \eta) / \pi (\bar{D}/2)^2 = Q_{\text{scat}}(\bar{x}, \eta) + Q_{\text{abs}}(\bar{x}, \eta) \quad (13)$$



is the extinction efficiency. The corresponding experimental quantities  $R_1^{\text{exp}}$  and  $R_2^{\text{exp}}$  are defined to be

$$R_1^{\text{exp}} = \left( \pi / \langle \sin^2 \psi_i \rangle \Delta \psi_i \right) (\bar{L} / \ell_i) \left[ \Phi_1(\theta_i, \psi_i) / \Phi_0 \right] / (-\ln \bar{T}) \quad (14)$$

$$R_2^{\text{exp}} = \left( \pi / \langle \cos^2 \psi_i \rangle \Delta \psi_i \right) (\bar{L} / \ell_i) \left[ \Phi_2(\theta_i, \psi_i) / \Phi_0 \right] / (-\ln \bar{T}) \quad (15)$$

where  $\bar{T}$  is the experimental value of the transmission ratio as measured for an effective extinction length  $\bar{L}$ .  $\bar{L}$  is a "lumped" parameter that incorporates the effect of particle density gradients; it is defined as

$$\bar{L} = \int_0^{\bar{L}} \int_0^\infty \frac{\partial n(x, \ell)}{\partial x} dx d\ell / \left[ \frac{1}{\ell_i} \int_0^{\ell_i} \int_0^\infty \frac{\partial n(x, \ell)}{\partial x} dx d\ell \right]$$

Figures 7a and b show the variations of  $R_1$  and  $R_2$ , respectively, with  $\bar{x}$  for iron in a particular scattering geometry. Again, ambiguity in the determination of  $\bar{x}$  results.

Now, however, the task at hand is to determine whether common  $\bar{x}$  values result from measurement of the  $P^{\text{exp}}$  and  $R_{1,2}^{\text{exp}}$  signals. Prior to this search of the set of allowed  $\bar{x}$  values, the experimental uncertainty values  $\delta R_{1,2}^{\text{exp}}$  are required to determine the corresponding uncertainty in  $\bar{x}$ . These relations can be shown to be

$$\frac{\delta R_{1,2}}{R_{1,2}} = \left[ (\delta \Phi_{1,2} / \Phi_{1,2})^2 + (\delta \ln \bar{T} / \ln \bar{T})^2 \right]^{1/2} + \frac{\delta \bar{L}}{\bar{L}} \quad (16)$$

where  $\delta \Phi_{1,2}$  and  $\delta \ln \bar{T}$  are the estimated imprecision values for the corresponding measured quantities, and  $\delta \bar{L}$  is the uncertainty in  $\bar{L}$ .

The combination of  $P^{\text{exp}}$  and  $R_{1,2}^{\text{exp}}$  for determining  $\bar{x}$  was used in Ref. 3; the diameter of the particles measured in Ref. 3 was found to be  $0.8 \pm 0.1 \mu$ . In this case, the predominant contribution to the uncertainty of  $\bar{x}$  was the uncertainty in the extinction length  $\bar{L}$ , and, relative to  $\delta \bar{L}$ , both  $\delta \Phi_{1,2}$  and  $\delta \bar{T}$  were negligible.

For those situations in which the measurement of the transmission ratio  $\bar{T}$  is impractical, an additional scattering function ratio can be defined wherein the transmission measurement is replaced by a backscattering channel. This Angular/Backscattering ratio (ANGBAR) can be defined, for the independent polarization states, as

$$R_{B1,2}(\bar{x}, \theta_i, \eta) = \langle i_{1,2}(\bar{x}, \theta_i, \eta) \rangle / \bar{x}^2 Q_B(\bar{x}, \eta) \quad (17)$$

where  $Q_B$  is the backscattering efficiency factor. The experimental counterparts to Eq. (17) are obvious.

Once the average size has been determined with any of the sizing procedures discussed here, particle number density can be determined from Eq. (3), if transmission measurements are available. The result is a spatially averaged number density along the line of sight. Of course, an alternative is to measure the absolute scattering intensity. If transmission measurements are available, then the spatially averaged number density of the scatterers can be determined from Eq. (3) by convolution with the cross sections, such as those shown in Fig. 8. This type of analysis was demonstrated in Ref. 3.

It can be seen by referring to Eqs. (11), (12), and (17) that the ANGER and ANGBAR scattering ratios depend upon the extinction and backscattering efficiency factors  $Q_{ext}$  and  $Q_B$ , respectively. A better appreciation of these scattering ratios is achieved by noting some of the qualitative dependencies of  $Q_{ext}$  and  $Q_B$  on the parameters  $\bar{x}$  and  $\eta$ . Shown in Fig. 9 is the variation of  $Q_{ext}$  with  $\bar{x}$  for transparent ( $\kappa = 0$ ) and absorptive ( $\kappa \neq 0$ ) particles. For absorptive particles (Ref. 9)  $\lim_{\bar{x} \rightarrow \infty} Q_{ext}(\bar{x}, \eta) = 2$ . Figure 9 shows that convergence to the limit is rapid for  $\bar{x}$ . Clearly, this asymptotic convergence is the mathematical expression of the transition in scattering theory from the exact Mie theory to the geometrical optics limit. No such limit occurs for transparent particles (Ref. 12). In fact, oscillations about the limit, 2, persist for size parameters as large as several thousand. Figure 9 shows that there are several scales of oscillations corresponding to resonances in different terms in the Mie series. Surface waves, generated by the last few terms in the Mie series just before convergence, are the sources of the smallest scale of oscillations. These oscillations are characterized by size parameter periodicity much less than unity, and they disappear altogether when the absorptive index is as large as 0.001 (Ref. 13).

The backscattering efficiency has a similar geometrical optics limit:

$$\lim_{\bar{x} \rightarrow \infty} Q_B(\bar{x}, \eta) = \left| (\eta - 1) / (\eta + 1) \right|^2 \quad (18)$$

As is shown by Fig. 10, this limit also occurs at comparatively small size parameters for absorptive particles but not for transparent particles. As is the case for  $Q_{ext}$ , the oscillations become damped with an average value that approximates the geometrical optics limit at size parameters on the order of a few thousand (Ref. 10). For a polydisperse PSDF, the oscillations persist with respect to the modal diameter, as is shown by Fig. 11.

As a consequence of this behavior of the efficiencies, the ANGER and ANGBAR functions vary considerably for transparent and absorptive particles. Figure 12 shows the ANGER functions for copper particles and for imaginary particles having the same real refractive index, but zero absorptive index. These results indicate that, because of the sensitivity of this function to the absorptive index, Mie scattering can be used to determine  $\eta$  in an iterative fashion.

Unlike  $Q_{ext}$  and  $Q_B$ , the degree-of-polarization measurements are insensitive to the absorptive index, but they are quite sensitive to the real refractive index. This can be seen by comparing Fig. 6 with Figs. 13 and 14, which show the degree-of-polarization versus size parameter for copper and iron, respectively, at the same conditions as for Fig. 6. Again, these results suggest that the real refractive index can be determined, iteratively, from analysis of Mie scattering measurements. For iterative determination of the refractive indices, angular scattering measurements should be concentrated near the rainbow angle of the suspected particle constituents. The rainbow angle is a function of only the real refractive index in the geometrical optics limit. As the size parameter decreases, the rainbow angle increases slowly until it ceases to have physical significance. This occurs when the particle diameter becomes too small to permit internal reflections to occur (i.e., the radiation wavelength either equals or exceeds the particle radius).

The preceding discussion of properties of the Mie scattering ratios used in the AEDC particle diagnostics scheme was illustrated by the use of calculations that assume an azimuthal angle of  $\pi/4$  and solid angles equal to those stated in Ref. 3. However, when it is suspected that only submicron particles are present, then degree-of-polarization measurements made at the scattering and azimuthal angles of  $\pi/2$  and either 0 or  $\pi$ , respectively, can be extremely useful, as shown by Fig. 15. These graphs illustrate the transition from Rayleigh to Mie scattering; this behavior permits unique determination of the average size of particles for size parameters between limits that depend on the collection optics solid angles and the real refractive index. Figure 15 shows the effect of progressively increasing the subtended solid angle. The basis for this method of size determination can be explained as follows: In the Rayleigh scattering limit, the parallel polarization state is completely suppressed at a scattering angle of  $\pi/2$ , as shown in Figs. 16 and 17 (Ref. 7). As shown in Fig. 16, the parallel Mie intensity decreases very rapidly as the size parameter approaches zero. In contrast, as shown in Fig. 17, the perpendicular Mie function decreases much less rapidly with size parameter. The use of incident polarization parallel or anti-parallel to the scattering plane, however, suppresses the perpendicular component, as suggested by Eq. (4), except for terms proportional to the subtended azimuthal angle. [See Eq. (8a).] With a decrease in particle size, the degree of polarization increases from its asymptotic limit of -1 because the parallel polarization component becomes comparable to the azimuthally suppressed perpendicular component.

This behavior, shown in Fig. 18, results from the transition of the scattering process into the Rayleigh scattering regime. Reference 7 describes the use of this transition to determine the size of very small droplets present in the exhaust of a liquid-propellant rocket engine. In this configuration, measured degree-of-polarization values greater than -1 are indisputable evidence that the PSDF occupies predominantly the size range below the limit at which asymptotic behavior begins.

### 3.0 SIZE DECONVOLUTION ANALYSIS

A histogram representation of the PSDF can be obtained with use of multiangular measurements of the Mie-scattered signals. The PSDF deconvolution of the integral scattering equations [the polydisperse forms of Eqs. (1) and (2)] can be accomplished, in principle, with a direct inversion of the equations as well as with a multivariate nonlinear regression analysis. These options are shown in Fig. 4.

The inversion scheme discussed in Appendix A yields a histogram representation of the PSDF,  $f(x)$ . This representation is defined for each of several equal-sized bins as the result of integrating the PSDF over the size bin. Thus, the results of deconvolution represent the mole fraction of particles in each size bin. Consequently, the histogram approximation to the PSDF is defined as the result of dividing the deconvolved mole fractions for each size bin by the bin size. The DECRATS and the deconvolved histogram are shown and discussed in Appendix A for this deconvolution using simulated scattering data. The ultimate size resolution (the number of size bins in the histogram) that is attainable by this size deconvolution procedure is limited by the level of both experimental and computational error in each DECRAT; this is detailed in Appendix A.

One might generally expect accurate deconvolution into a number of size bins equal to the number of forward scattering angles plus twice the number of backscattering angles (excluding the reference angle) at which scattering data are taken. Actually, the number of bins that can be deconvolved accurately is somewhat smaller than this approximation. Whether an accurate deconvolution into a specified number of size bins can be accomplished, for a given experimental configuration, can be determined, as explained in Appendix A, by comparing eigenvalues of the Mie-scattering kernels (the results of quadrature of the Mie functions in each size bin) with the computed residual error which is obtained without smoothing the kernels. If this test fails, then the number of size bins must be reduced.

The choice to invert the scattering equations by this deconvolution procedure, rather than to invert directly by nonlinear regression, was made on the basis of the strong non-monotonicity of the Mie functions. For such functions unique results are difficult to obtain by nonlinear regression analysis.

Another technique is being developed that will combine the virtues of both the Fredholm deconvolution and direct regression procedures. An existing AEDC multivariate nonlinear regression scheme (Ref. 14) is being adapted for these purposes. The resulting overall regression can be organized into the following steps:

1. The histogram approximation to the PSDF is obtained, as described in Appendix A.
2. Parameters of the PSDF are obtained by regression of the histogram approximation.
3. The Mie scattering functions corresponding to the regressed PSDF are then computed and compared with the experimental data to see whether the computed scattering ratios lie within the experimental imprecision bands.
4. Numerical derivatives can also be evaluated for the direct regression of the scattering equations, and direct regression of the scattering data can be undertaken, using the results of the previous regression as initial guesses to the full-scale, direct regression.

Obviously, steps 3 and 4 must be repeated until a satisfactory regression is obtained. However, the stability characteristics of this technique are at present unknown and must be determined in the course of developing this method of inversion.

#### **4.0 DETERMINING THE AVERAGE SIZE PARAMETERS AND MOLE FRACTIONS OF PARTICULATE MIXTURES**

In principle, it is possible to use Mie scattering for determining the average particle size parameters and species mole fractions of a polydisperse, multispecies particulate mixture of known indices of refraction. The only requirement is that there be an adequate number of Mie scattering measurements consisting of the polarization state, angular distribution, and wavelength variation of the scattered radiation. These independent variables may be taken singly (such as taking only the angular variation measurements) or in combinations (such as taking both wavelength and polarization variations of the angular scattering dependence of the Mie signal). For simplicity, the following derivation will assume the use of both states of polarization, multiangular measurements, and the use of a single wavelength. In consideration of the existing uncertainties in deconvolving the PSDF of a single-species particulate sample, the initial development of a multispecies deconvolution has been the application of Mie scattering theory to a binary particulate mixture of known refractive indices; the individual species distribution functions of this mixture are treated as though they were monodisperse with respect to size parameter.

One can easily generalize the degree of polarization,  $P$ , as given by Eq. (6), to apply to a binary particulate mixture of mole fractions and size parameters,  $a_s$  and  $x_s$ ,  $s = 1,2$ , respectively. For scattering angles  $\theta_i$ ,  $\psi_i = \pi/4$ , the degree of polarization can be written as

$$P(\theta_i, \pi/4) = \sum_{s=1}^2 [(I_{is} - J_{is}) a_s] / \sum_{s=1}^2 [(I_{is} + J_{is}) a_s] \quad (19a)$$

where the elements of the matrices  $\tilde{I}$  and  $\tilde{J}$  are given by

$$\tilde{I}_{is} = \langle i_1(\theta_i, \eta_s, x_s) \rangle \quad (19b)$$

and

$$\tilde{J}_{is} = \langle i_2(\theta_i, \eta_s, x_s) \rangle \quad (19c)$$

Obviously, the range of the subscript  $i$  depends upon the number of scattering angles used for the measurement. If  $P(\theta_i, \pi/4)$  is defined as  $P_i$ , then Eq. (19a) can be rewritten as

$$\sum_{s=1}^2 \tilde{T}_{is} a_s = 0 \quad (20a)$$

where

$$\tilde{T}_{is} = (P_i - 1) \tilde{I}_{is} + (P_i + 1) \tilde{J}_{is} \quad (20b)$$

When two angular measurements have been obtained ( $i = 1,2$  for the binary mixture), then the set of homogeneous equations of Eq. (20a), usually an overdetermined set, becomes a completely determined set. By expanding Eq. (20a) for the stated case, one finds that

$$\tilde{T}_{11} a_1 + \tilde{T}_{12} a_2 = 0 \quad (20c)$$

and

$$\tilde{T}_{21} a_1 + \tilde{T}_{22} a_2 = 0 \quad (20d)$$

The ratio of mole fractions  $\beta = a_1/a_2$  is, of course, found to be

$$\beta = -\tilde{T}_{12}/\tilde{T}_{11} = -\tilde{T}_{22}/\tilde{T}_{21} \quad (21a)$$

It is appropriate to recall that  $P_i$  is an experimentally determined parameter. With use of Eq. (20b), one sees that  $\beta$  depends not only on  $P_i$  but also on the quantities  $\tilde{I}_{is}$  and  $\tilde{J}_{is}$ , both of which are functions of the unknown size parameters  $x_s$ ,  $s = 1, 2$ . Consequently, an iterative solution of Eq. (21a) for  $\beta$  is required for which values of the size parameter pair  $x_{1,2}$  are assumed. Eqs. (19b) and (19c) are used to compute  $\tilde{I}_{is}$  and  $\tilde{J}_{is}$ , respectively. Finally, since the solutions for  $a_s$ ,  $s = 1, 2$ , are mole fractions of the binary mixture, the solution set  $\{a_s\}$  is subject to the following constraints:

$$a_s \geq 0 \quad (21b)$$

and

$$\sum_{s=1}^2 a_s = 1 \quad (21c)$$

Since the process of solving Eq. (20a) is both numerical and iterative, the parameters  $\{x_s^{(k)}\}$ ,  $s = 1, 2$ , are defined to be the  $k$ th set of assumed size parameters, and  $x_s$ ,  $s = 1, 2$ , represent the actual size parameters of the mixture. Further, in anticipation of the round-off error that will be encountered in the numerical solution, the constraint of Eq. (21c) is relaxed to be

$$\left| \sum_{s=1}^2 a_s^{(k)} - 1 \right| < \epsilon < 1$$

where the superscript  $k$  on all quantities denotes their values appropriate to the  $k$ th choice of the set  $\{x_s^{(k)}\}$ .

The iterative determination of the actual size parameters of the mixture is begun by casting Eq. (21a) into the form of an inequality

$$\left| \frac{P_1 - P_{11}^{(k)}}{P_2 - P_{22}^{(k)}} - \frac{M_1^{(k)}}{M_2^{(k)}} \frac{P_1 - P_{12}^{(k)}}{P_2 - P_{22}^{(k)}} \right| \leq \epsilon < 1 \quad (22)$$

where the auxiliary functions  $M_i^{(k)}$  and  $P_{is}^{(k)}$  are defined for the  $k$ th set of size parameters,  $\{x_s^{(k)}\}$ , as

$$M_i^{(k)} = \left( \tilde{\Gamma}_{is}^{(k)} + \tilde{J}_{is}^{(k)} \right) / \left( \tilde{\Gamma}_{i1}^{(k)} + \tilde{J}_{i1}^{(k)} \right)$$

$$P_{is}^{(k)} = \left( \tilde{\Gamma}_{is}^{(k)} - \tilde{J}_{is}^{(k)} \right) / \left( \tilde{\Gamma}_{is}^{(k)} + \tilde{J}_{is}^{(k)} \right) \quad (23)$$

If the  $k$ th set of size parameters,  $\{x_s^{(k)}\}$ , satisfies Eq. (22), the corresponding species mole fractions are found from Eq. (21a) and

$$\alpha_1^{(k)} = \frac{\beta^{(k)}}{1 + \beta^{(k)}} \quad \text{and} \quad \alpha_2^{(k)} = \frac{1}{1 + \beta^{(k)}} \quad (24)$$

Clearly, the correct size parameters and species mole fractions are those choices that satisfy both Eqs. (21b) and (22).

Because of uncertainties in the measurements, there will be a range of size parameters and species mole fractions that satisfies both Eqs. (21b) and (22). The propagation of data imprecision into the analysis is taken into account when choosing the set of experimental values  $\{P_i\}$  so that they lie within the imprecision intervals stated in Eq. (10). If the  $j$ th such set is denoted  $\{P_i^{(j)}\}$ , then each  $P_i^{(j)}$  must satisfy

$$P_i^{\text{exp}} - \delta P_i \leq P_i^{(j)} \leq P_i^{\text{exp}} + \delta P_i$$

For each  $\{P_i^{(j)}\}$  chosen the entire algorithm must be used to determine the allowed particle sizes and species mole fractions. The number of samples of  $\{P_i^{(j)}\}$  which should be investigated represents a compromise between (1) the requirement of a large number of samples to assure adequate sampling statistics and (2) the limitations of the computer.

This analysis was applied in Ref. 3 (see Appendix B) to determine species concentrations of copper particles and tungsten particles in the AEDC von Kármán Gas Dynamics Facility (VKF) Tunnel F. The analysis indicated that the Mie scattering measurements performed at two angular stations were consistent with particulate mole fraction ranges of from 100% copper/0% tungsten to 79% copper/21% tungsten. Posttest analysis of a sample of collected particles indicated the composition to be 75% copper/25% tungsten. In addition, the two-species average size parameters were within the uncertainty range of the average size parameter for the case of 100% copper, and the



total mass of particulate matter, estimated with use of the analytical procedures reported herein was consistent with measurements of electrode metal loss in the Tunnel F arc-chamber, the source of the particles.

## 5.0 CONCLUDING REMARKS

This report has described and summarized the systematic development of the analytical procedures used for Mie scattering particle diagnostics. It is believed that this program will prove to be useful in a variety of applications at AEDC and other agencies. The strengths of the approach are (1) its ability to resolve the PSDF for an ensemble of many particles present in the focal volume of each detector, (2) time-resolution capability on the order of milliseconds, (3) ability to resolve particle chemical species distribution (if species refractive indices are known), (4) limited capability to determine effective indices of refraction in an iterative fashion for samples of unknown properties, and (5) the ability for implementation using available laser sources, detectors, and associated electronic and data recording systems. The program relies heavily on analytical procedures performed with a large-scale computer, but aspects of it have also been successfully performed on a microcomputer, the results of which demonstrate that the overall diagnostics scheme is versatile enough to permit incorporating portions of it into portable instrumentation and data analysis packages.

Future work will concentrate on improvement and additional testing of the techniques developed and completion of those portions of the program that remain under development. Incorporation of multispectral capability into the basic diagnostic procedures discussed here will also be investigated. Other potential extensions of the program include such obvious areas as Raman scattering and fluorescence from structured particles. In addition, generalization to permit diagnostics of aspherical particles is currently under consideration, and the effectiveness of these basic diagnostic methods in multiple-scattering environments will be considered.

## REFERENCES

1. Mundy, W. C., Roux, J. A., and Smith, A. M. "Mie Scattering by Spheres in an Absorbing Medium." Journal of the Optical Society of America, Vol. 64, No. 12, December 1974, pp. 1593-1597.
2. Dave, J. V. "Subroutines for Computing the Parameters of the Electromagnetic Radiation Scattered by a Sphere." Report 320 3237, IBM Scientific Center, Palo Alto, California, May 1968.

3. Lewis, J. W. L., Curry, B. P., and Weaver, D. P. "Determination of the Size Distribution for Particles in a Hypersonic Flow Field." AEDC-TR-77-101 (AD-A056923), July 1978.
4. Weaver, D. P., Curry, B. P., and Lewis, J. W. L. "Experimental Studies of Multiple-Scattered Light from Latex Spheres." AEDC-TR-79-60 (AD-A076322), August 1979.
5. Pinnick, R. G., Carroll, D. E., and Hofmann, D. J. "Polarized Light Scattered from Monodisperse Randomly Oriented Nonspherical Aerosol Particles: Measurements." Applied Optics, Vol. 15, No. 2, February 1976, pp. 384-393.
6. McGuire, R. L., Lewis, J. W. L., Weaver, D. P., and Curry, B. P. "Particle Diagnostics Using Mie Scattering and Image Intensification Techniques." AEDC-TR-79-42, December 1979.
7. Powell, H. M., Price, L. L., and Alt, R. E. "Bipropellant Engine Plume Contamination Program. Vol. 9: Chamber Measurements-Phase II." AEDC-TR-79-28. (To be published.)
8. Deirmendjian, D. Electromagnetic Scattering on Spherical Polydispersions. American Elsevier Publishing Co., New York, 1969.
9. Hulst, Hendrick Christoffel van de. Light Scattering by Small Particles. John Wiley and Sons, Inc., New York, 1969.
10. Kerker, Milton. The Scattering of Light, and Other Electromagnetic Radiation. Academic Press, New York, 1969.
11. Born, Max and Wolf, Emil. Principles of Optics: Electromagnetic Theory of Propagation, Interference and Diffraction of Light. Pergamon Press, New York, 1959.
12. Chýlek, Petr, "Large-Sphere Limits of the Mie-Scattering Functions." Journal of the Optical Society of America, Vol. 63, No. 6, June 1973, pp. 699-706.
13. Chýlek, Petr, Kiehl, J. T., and Ko, M. K. W. "Narrow Resonance Structure in the Mie Scattering Characteristics." Applied Optics, Vol. 17, No. 19, 1 October 1978, pp. 3019-3021.
14. Dorrell, E. W., Jr. "A Method for the Solution of the Generalized Nonlinear Least Squares Problem." Master's thesis, University of Tennessee, March 1975.

15. Tingey, D. L. "An Inversion Technique Developed to Determine the Characteristics of Mie Scatterers Differing in Index of Refraction Interspersed in the Stratosphere." Presented at the Conference on Atmospheric Radiation, Fort Collins, Colorado, August 7-9, 1972.

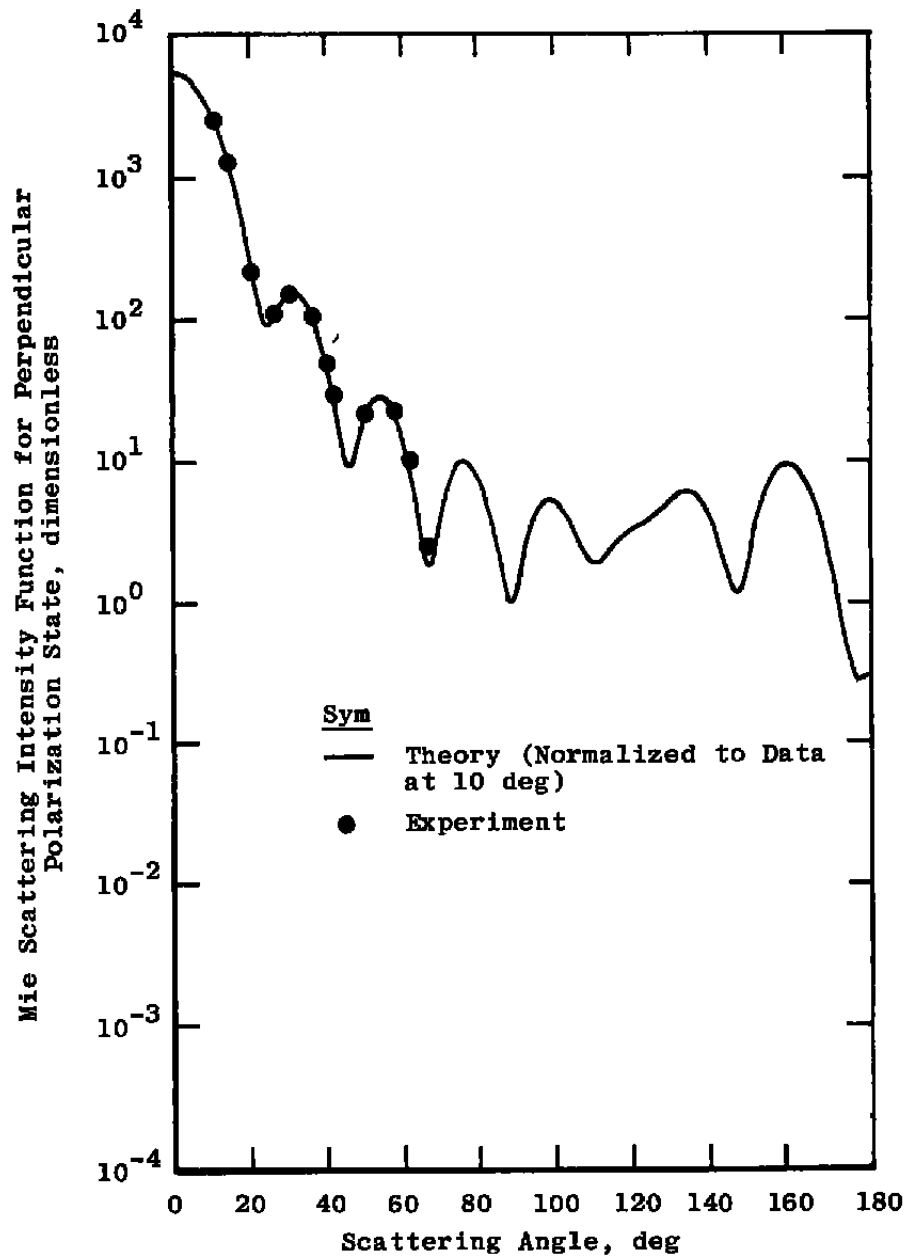
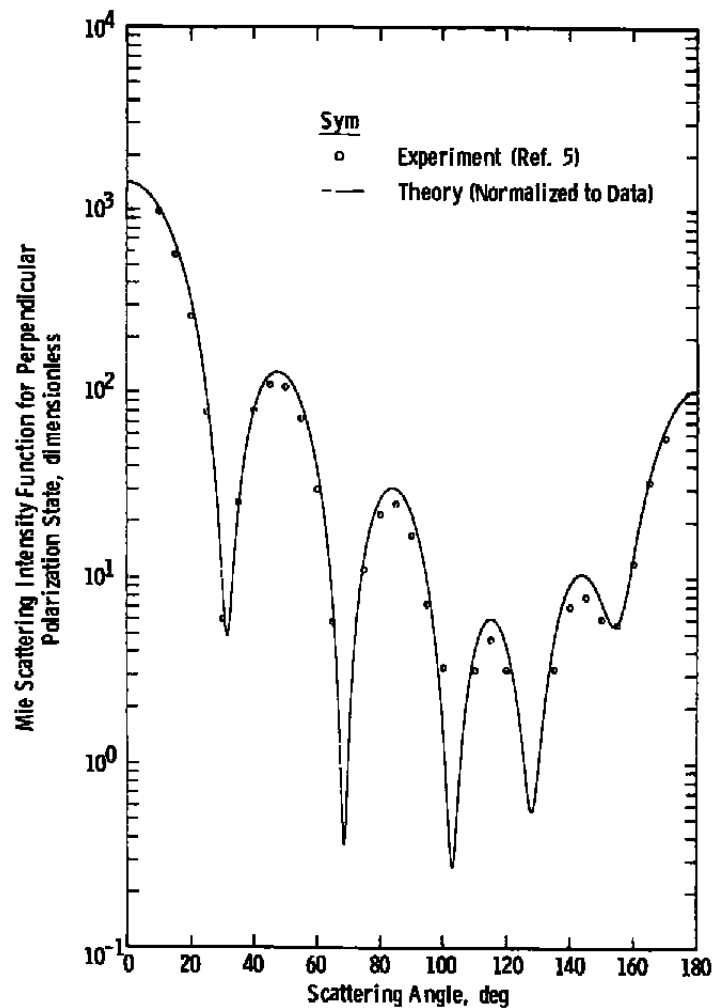
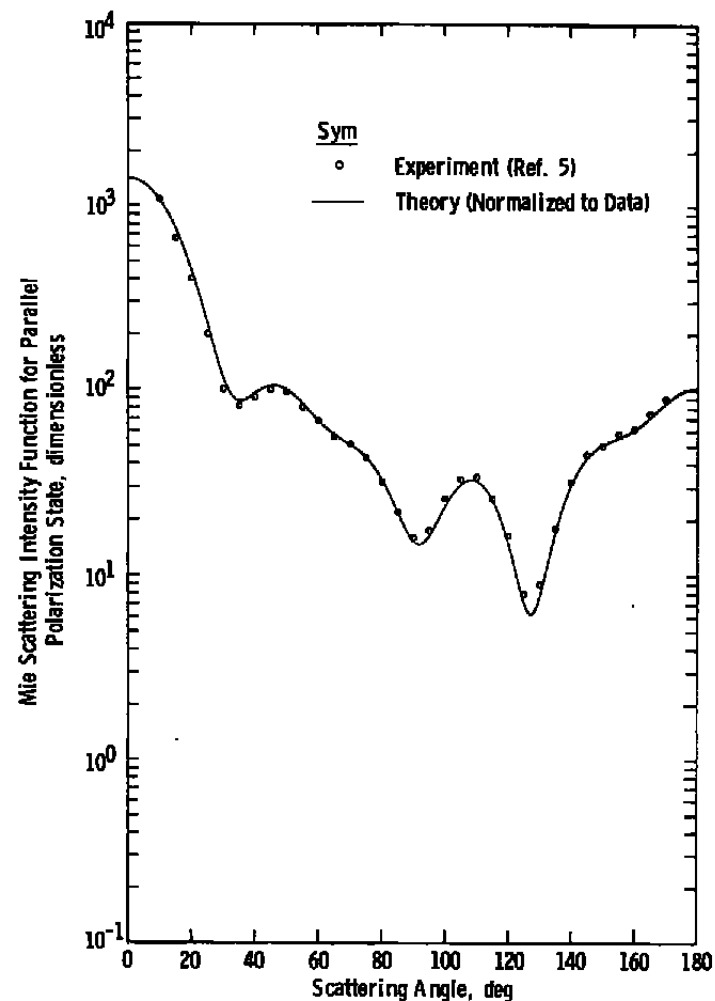


**Figure 1. Comparison of Mie theory with experimental scattered light intensity from monodisperse polystyrene latex spheres in water suspension (from Ref. 4).**



a. Perpendicular polarization state



b. Parallel polarization state

Figure 2. Comparison of Mie theory with experimental scattered light intensity from a narrow polydispersion of spherical aerosols.

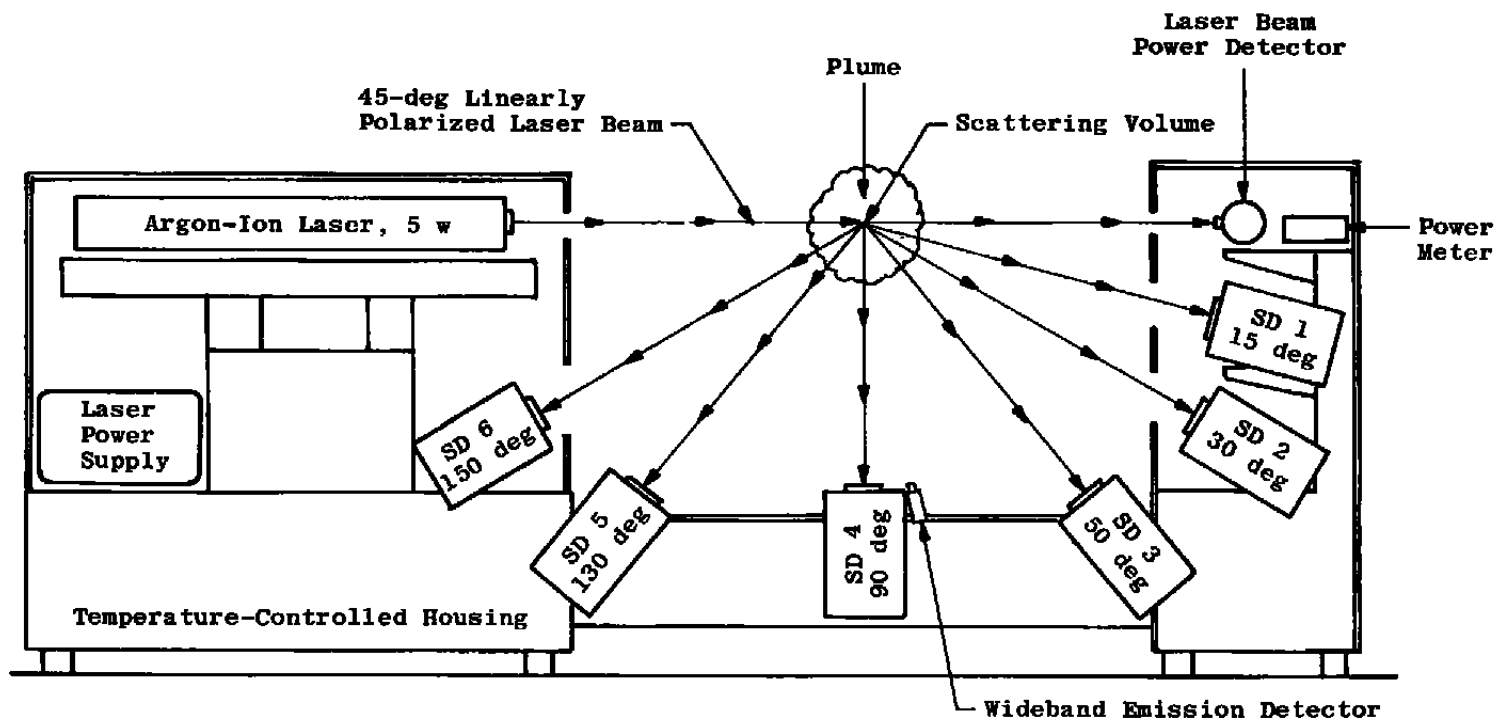


Figure 3. Mie scattering experimental configuration similar to that used in the AFRPL BATES motor tests.

## Particle Diagnostics Flow Chart

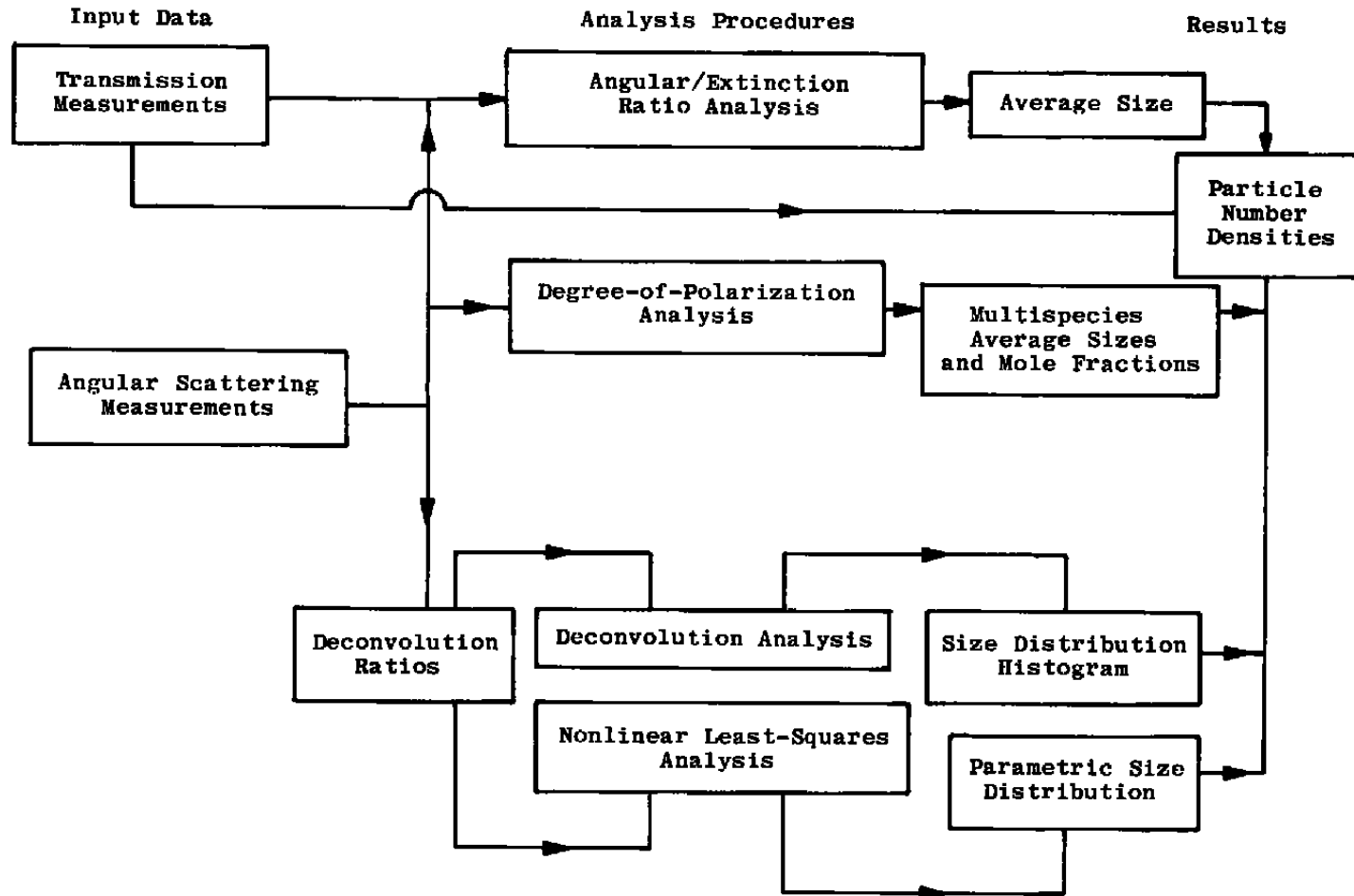
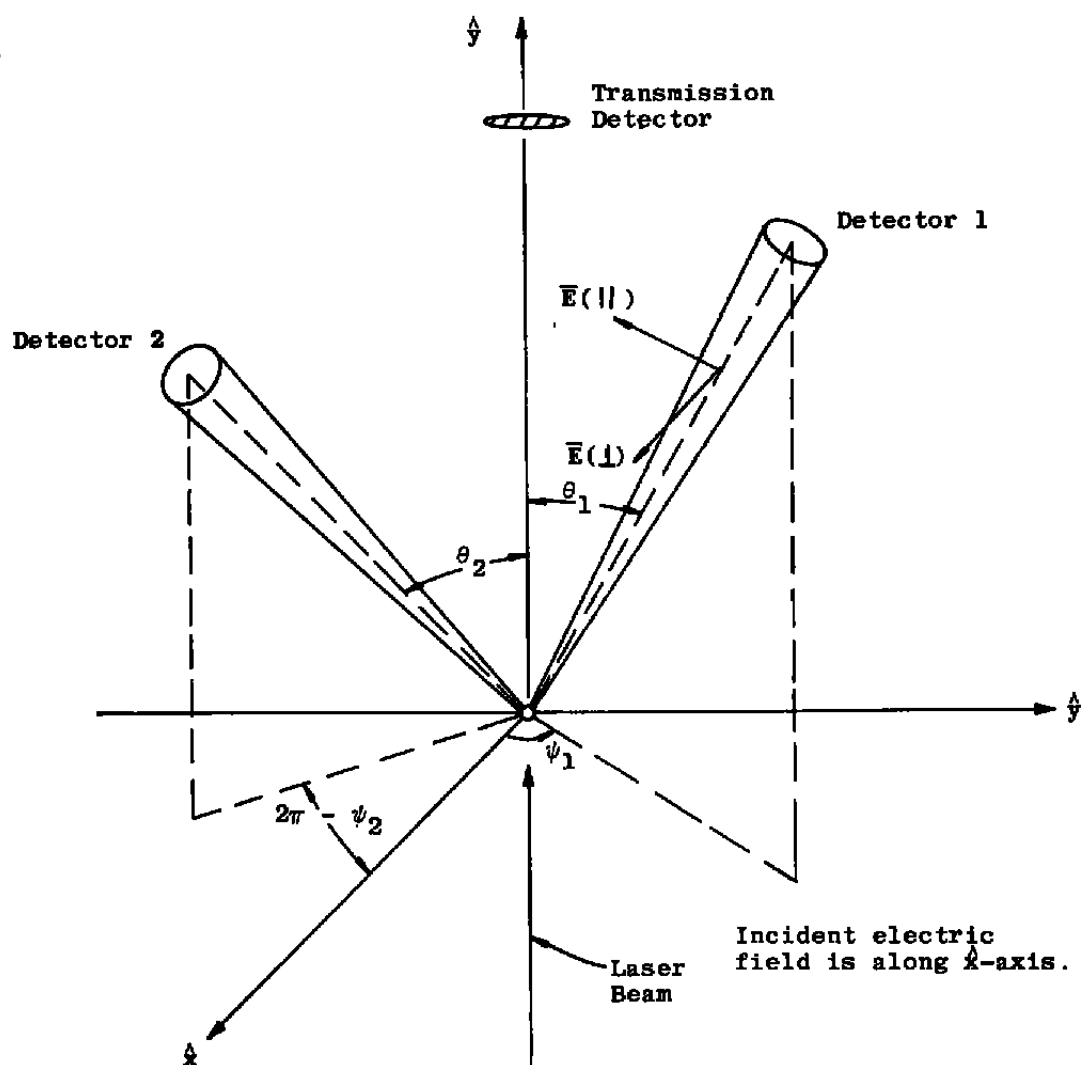
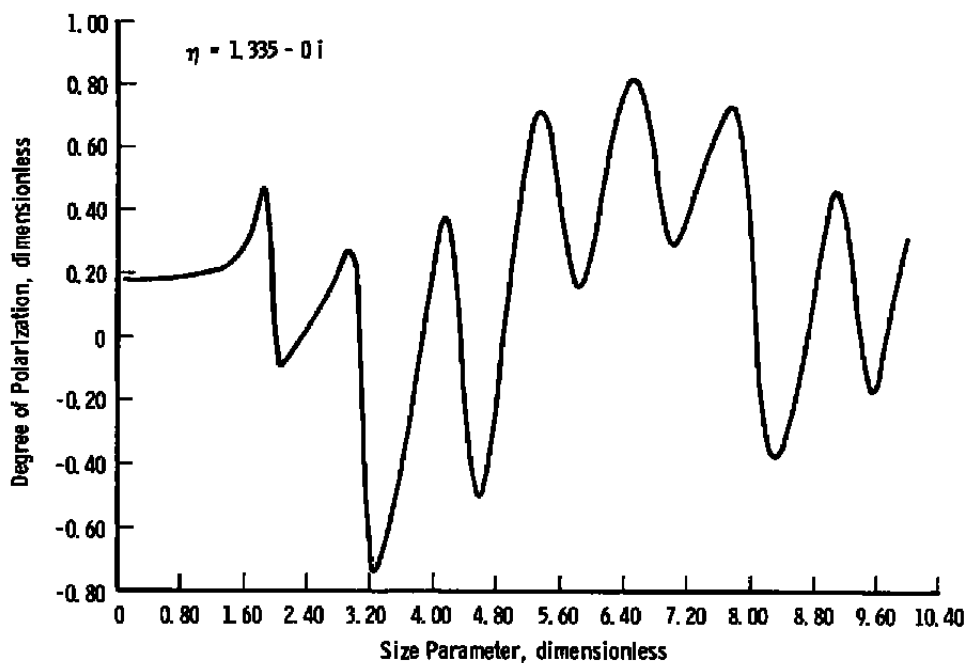


Figure 4. Flow chart of AEDC Mie scattering particle diagnostics program.

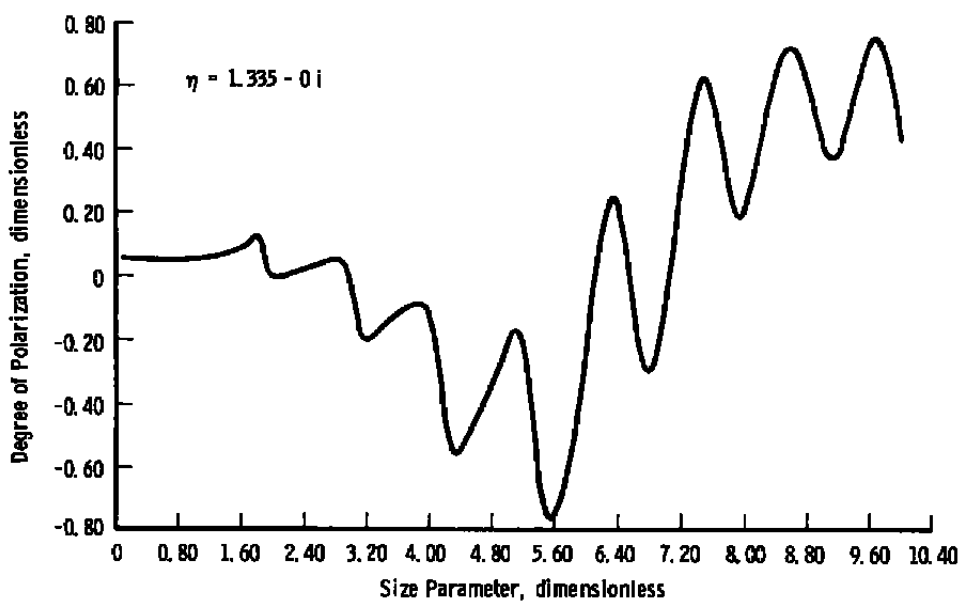


**Figure 5. Spherical coordinate geometry for the multiangular scattering of light by a dielectric sphere.**



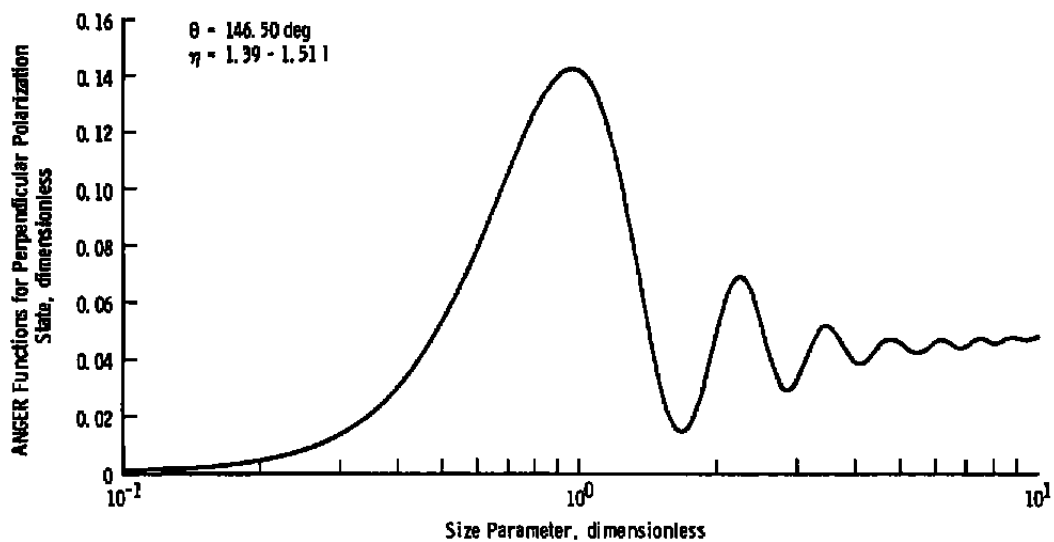


a.  $\theta = 146.50$  deg

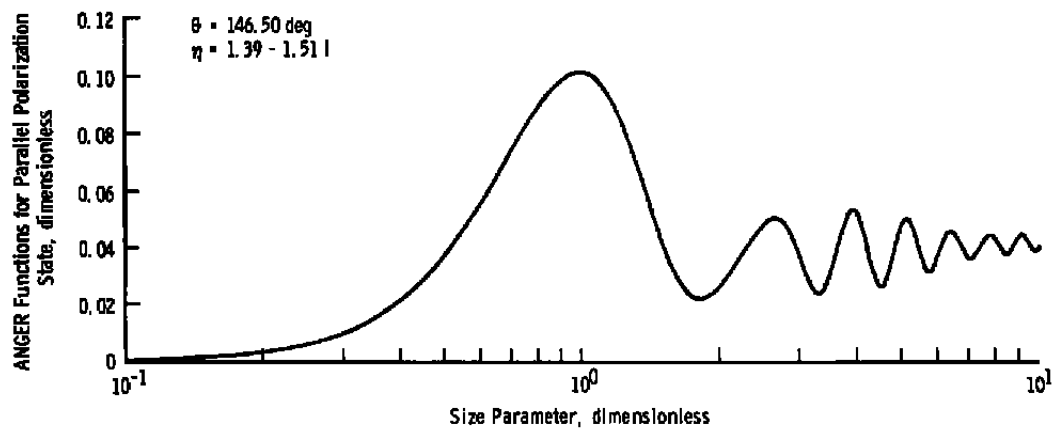


b.  $\theta = 161.90$  deg

**Figure 6. Size dependence of the degree of polarization of light scattered by water droplets in the geometry of Ref. 3.**



a. Perpendicular polarization



b. Parallel polarization

**Figure 7. Size dependence of ANGER functions for iron in the geometry of Ref. 3.**

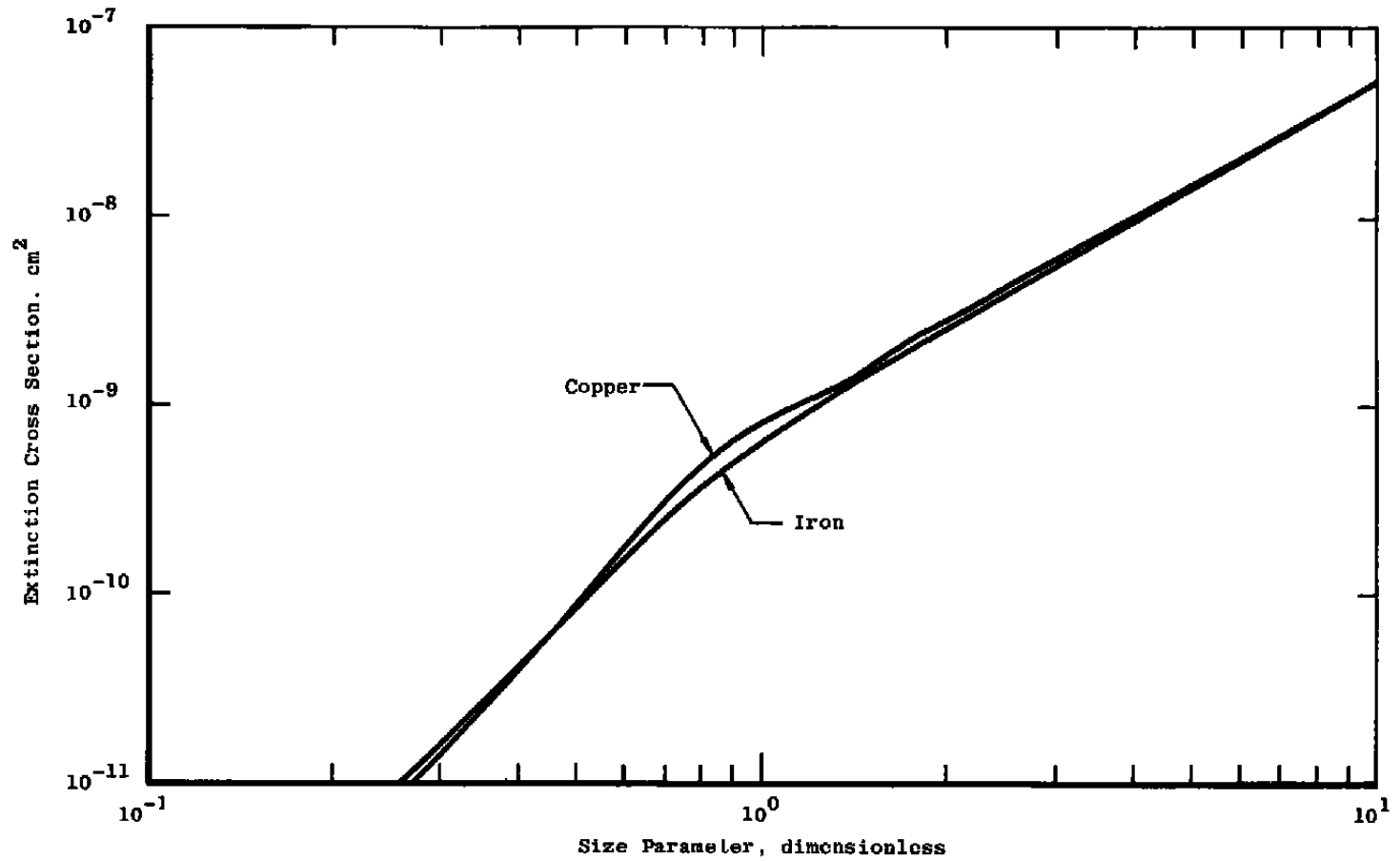
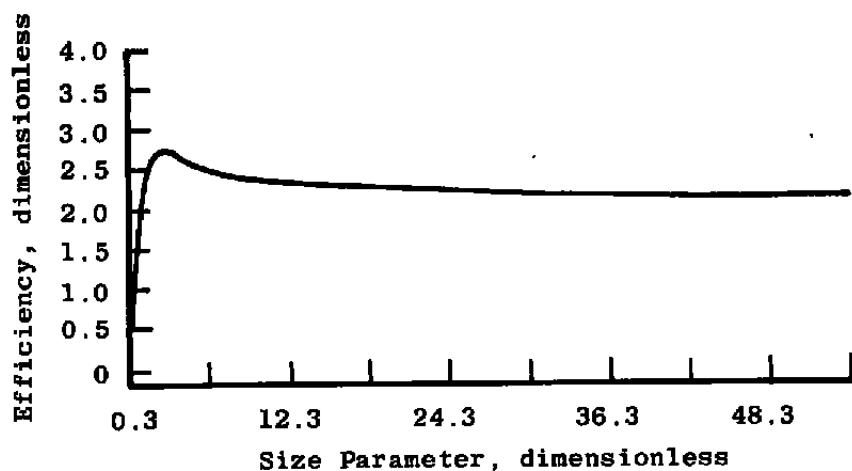
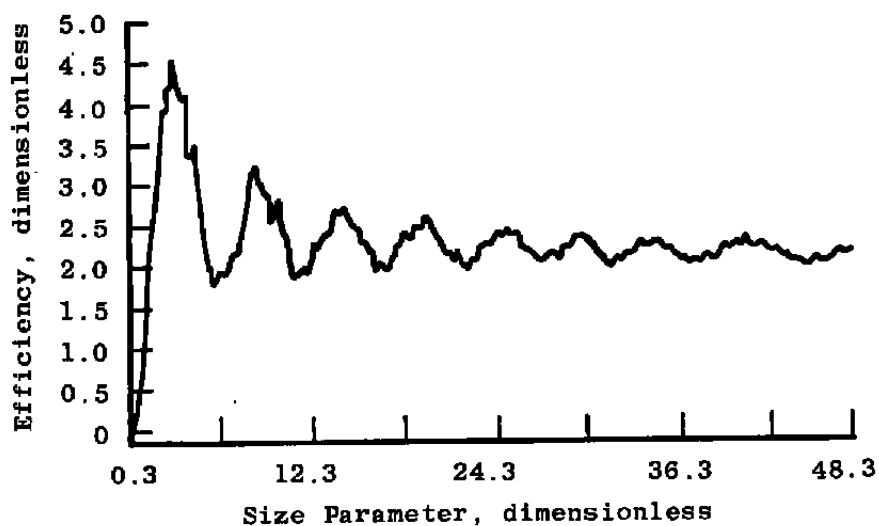


Figure 8. Size dependence of the extinction cross sections for copper particles and iron particles: 0.5145- $\mu$  light.

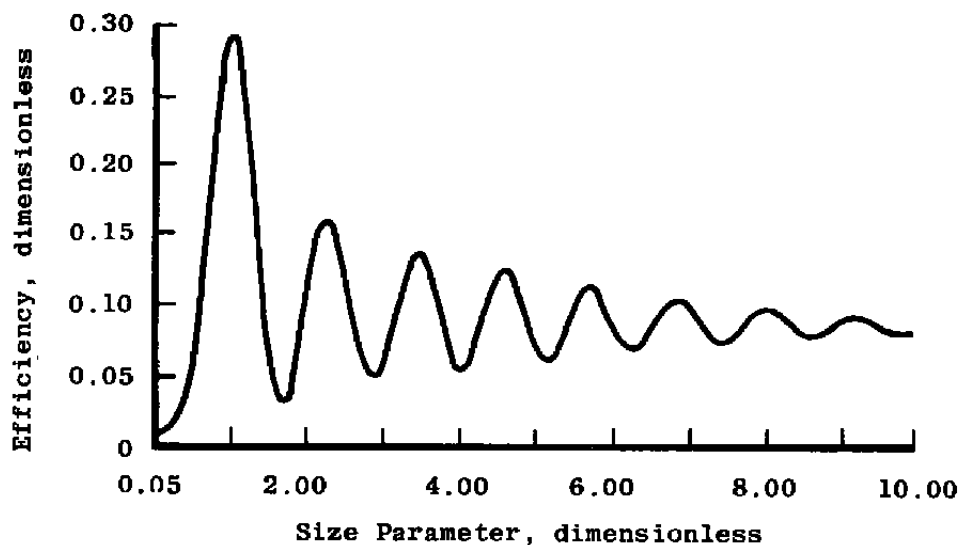


a. Carbon soot —  $\eta = 1.56 - 0.46 i$

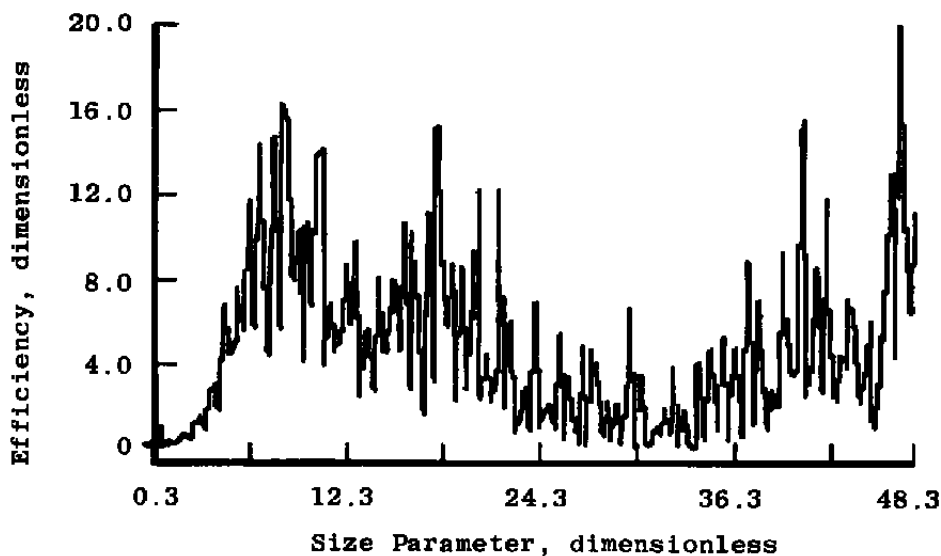


b. Calcite ( $\text{CaCO}_3$ ) —  $\eta = 1.6 - 0 i$

Figure 9. Size dependence of the extinction efficiencies for carbon soot and calcite: visible light.



a. Carbon soot -  $\eta = 1.56 - 0.46 i$



b. Calcite ( $\text{CaCO}_3$ ) -  $\eta = 1.6 - 0 i$

Figure 10. Size dependence of the backscattering efficiencies for carbon soot and calcite: visible light.

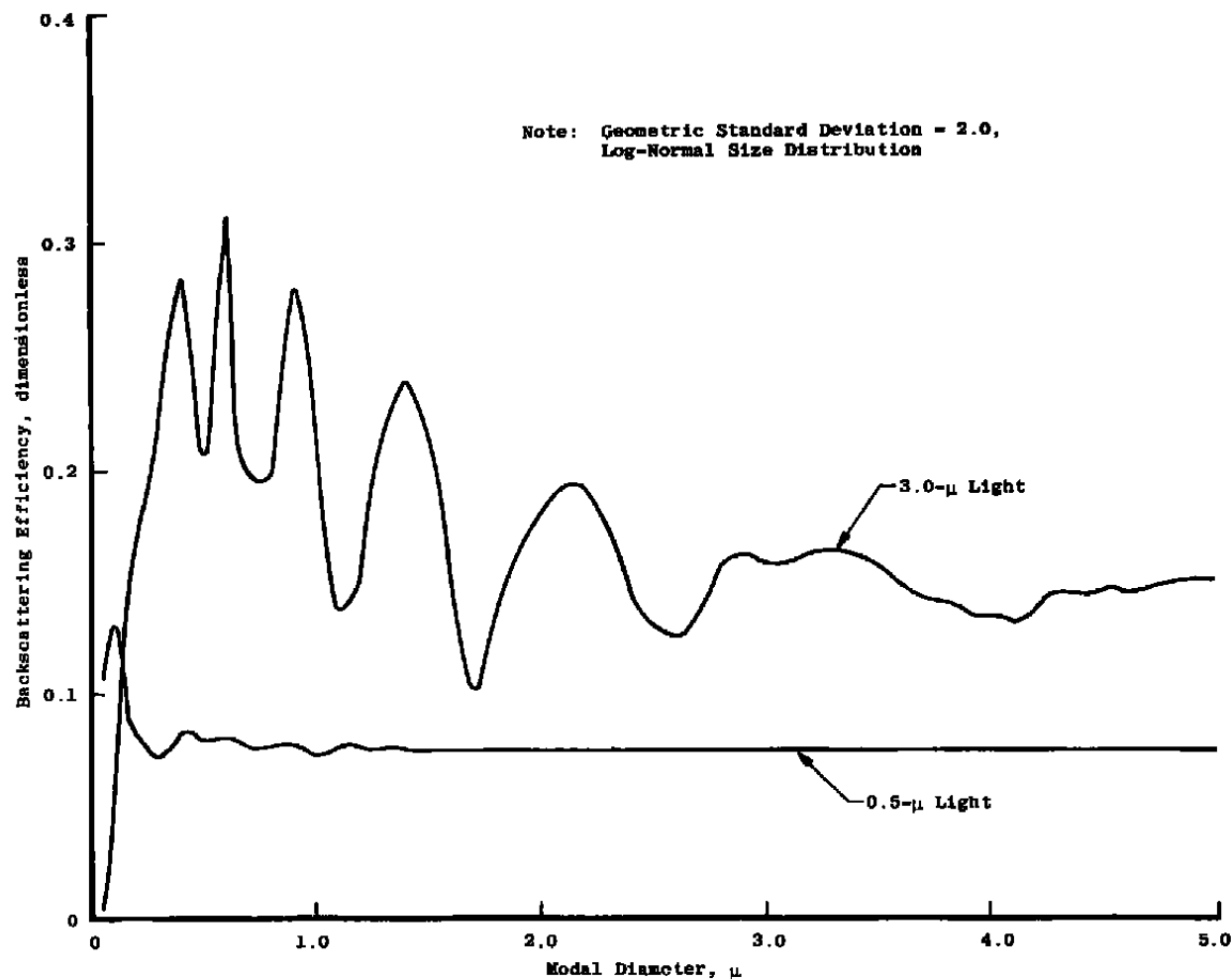
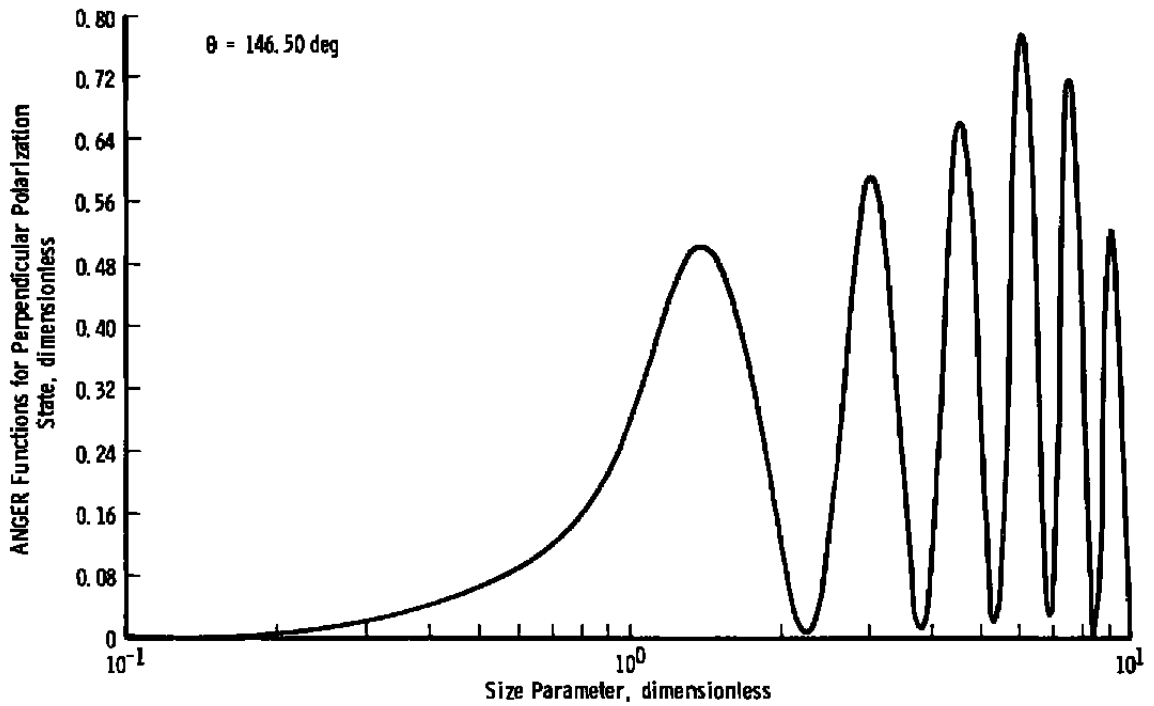
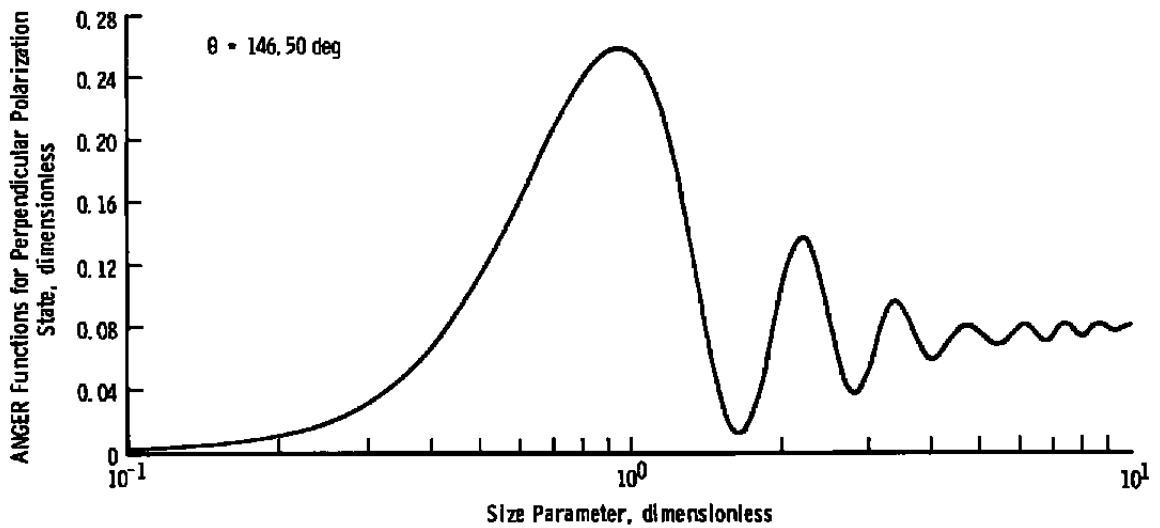


Figure 11. Dependence of backscattering efficiency on modal diameter for polydisperse soot particles at visible and infrared wavelengths.

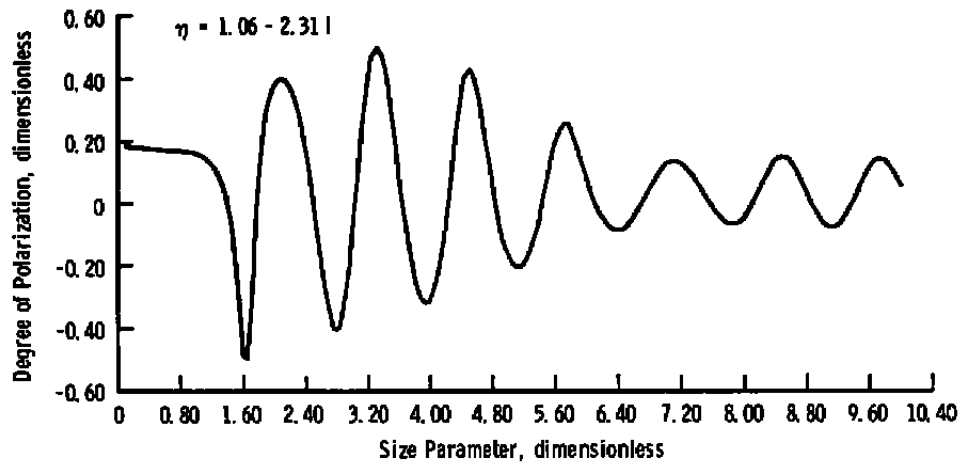


a.  $\eta = 1.06 - 0i$

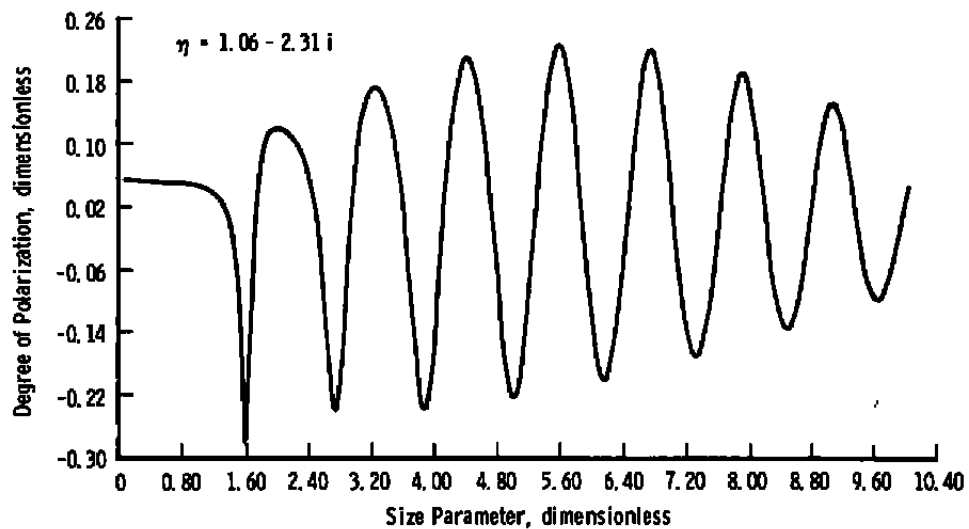


b.  $\eta = 1.06 - 2.31i$

Figure 12. Effect of absorptive index on size dependence of ANGER functions for copper (perpendicular polarization) in the geometry of Ref. 3.



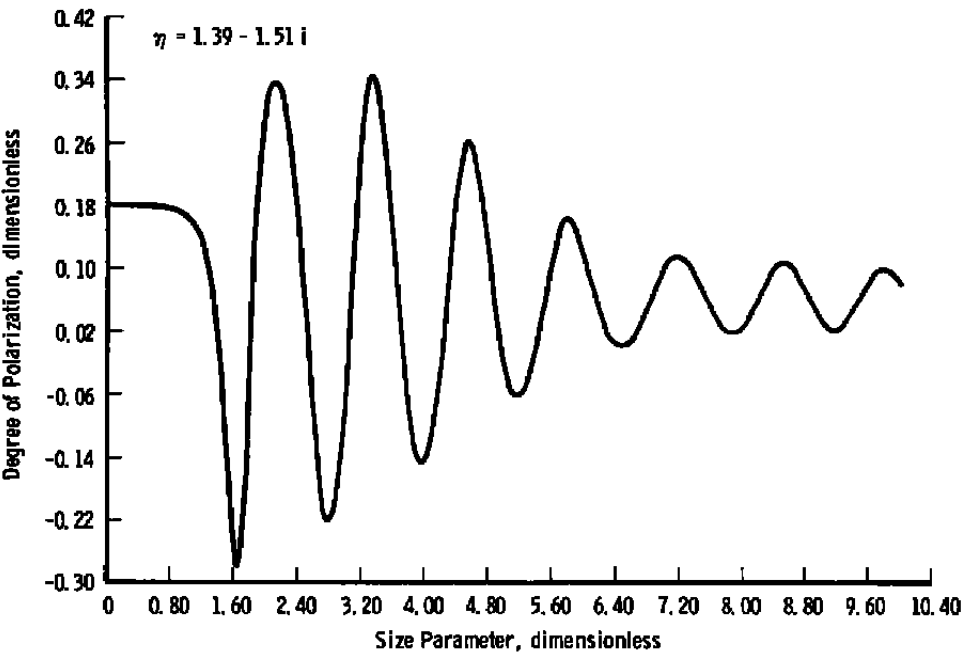
**a.  $\theta = 146.50$  deg**



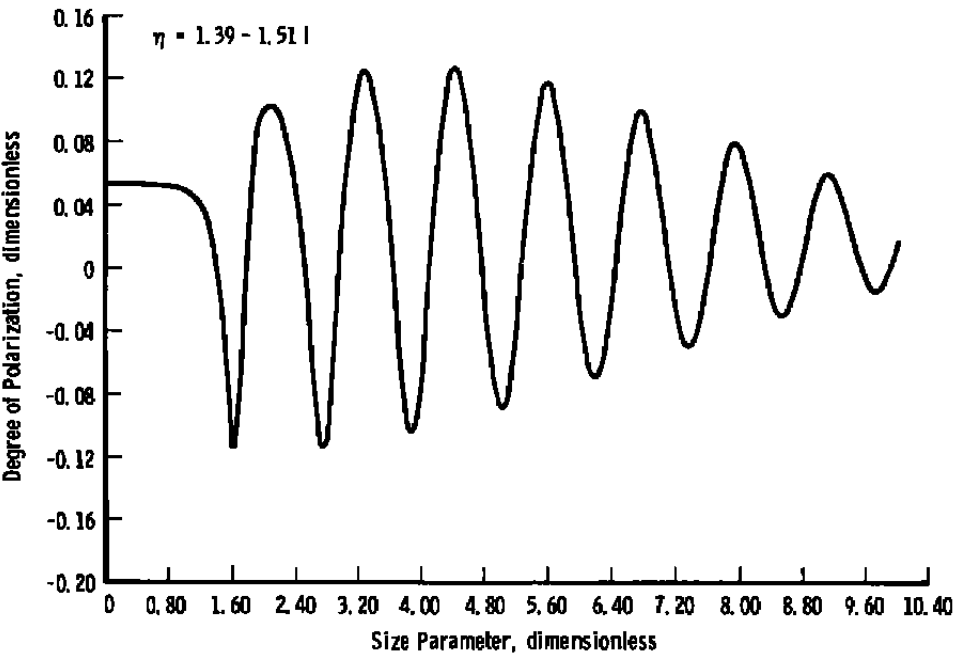
**b.  $\theta = 161.90$  deg**

**Figure 13. Size dependence of the degree of polarization of light scattered by copper spheres in the geometry of Ref. 3.**





a.  $\theta = 146.50$  deg



b.  $\theta = 161.90$  deg

**Figure 14. Size dependence of the degree of polarization of light scattered by iron spheres in the geometry of Ref. 3.**

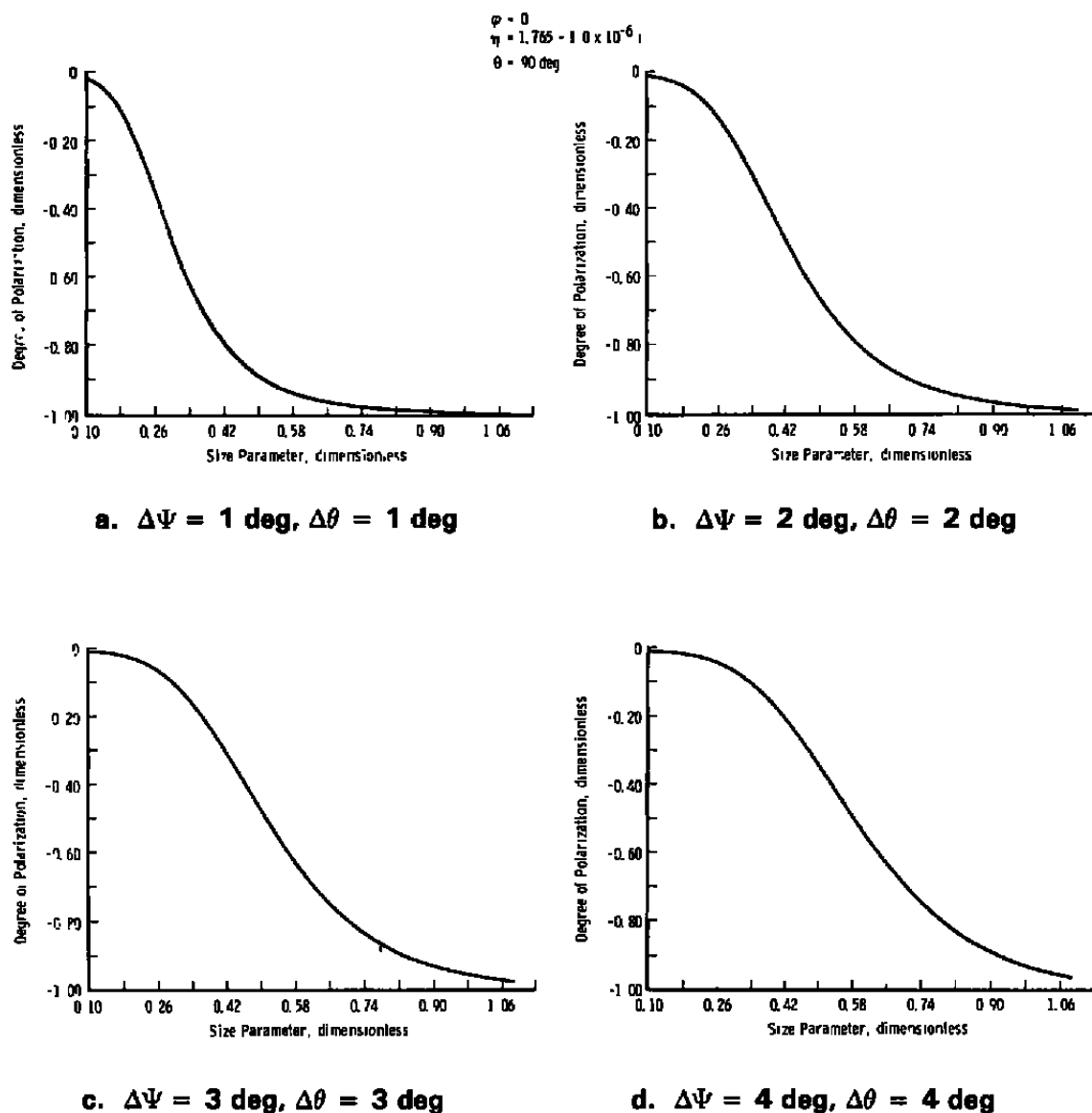


**Figure 15.** Effect of collection optics subtended solid angle on size dependence of the degree of polarization for light scattering from  $\text{Al}_2\text{O}_3$  spheres at 90-deg scattering angle and incident polarization parallel to the scattering plane.

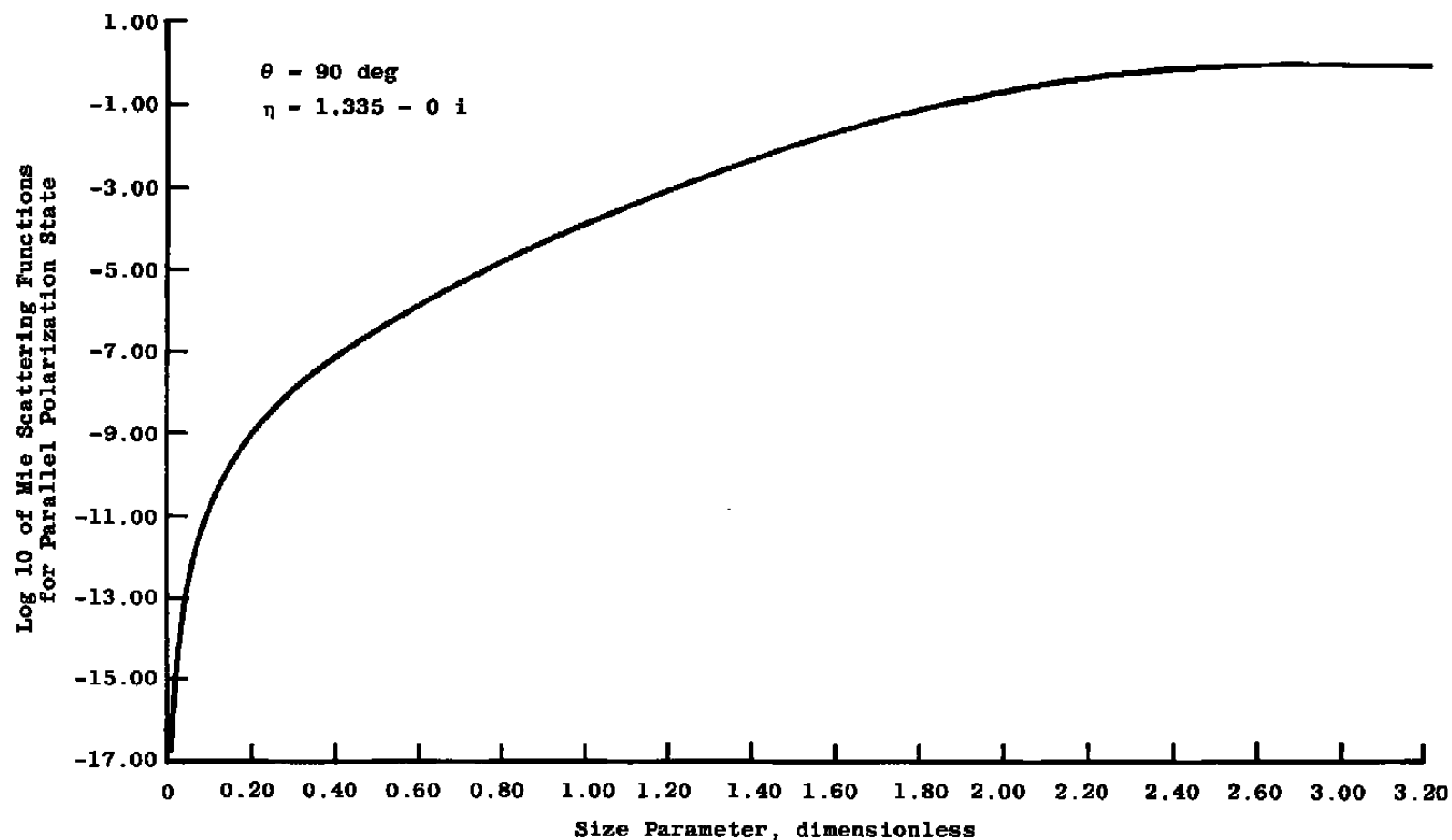


Figure 16. Size dependence of the parallel Mie scattering intensity functions in the geometry of Ref. 7.

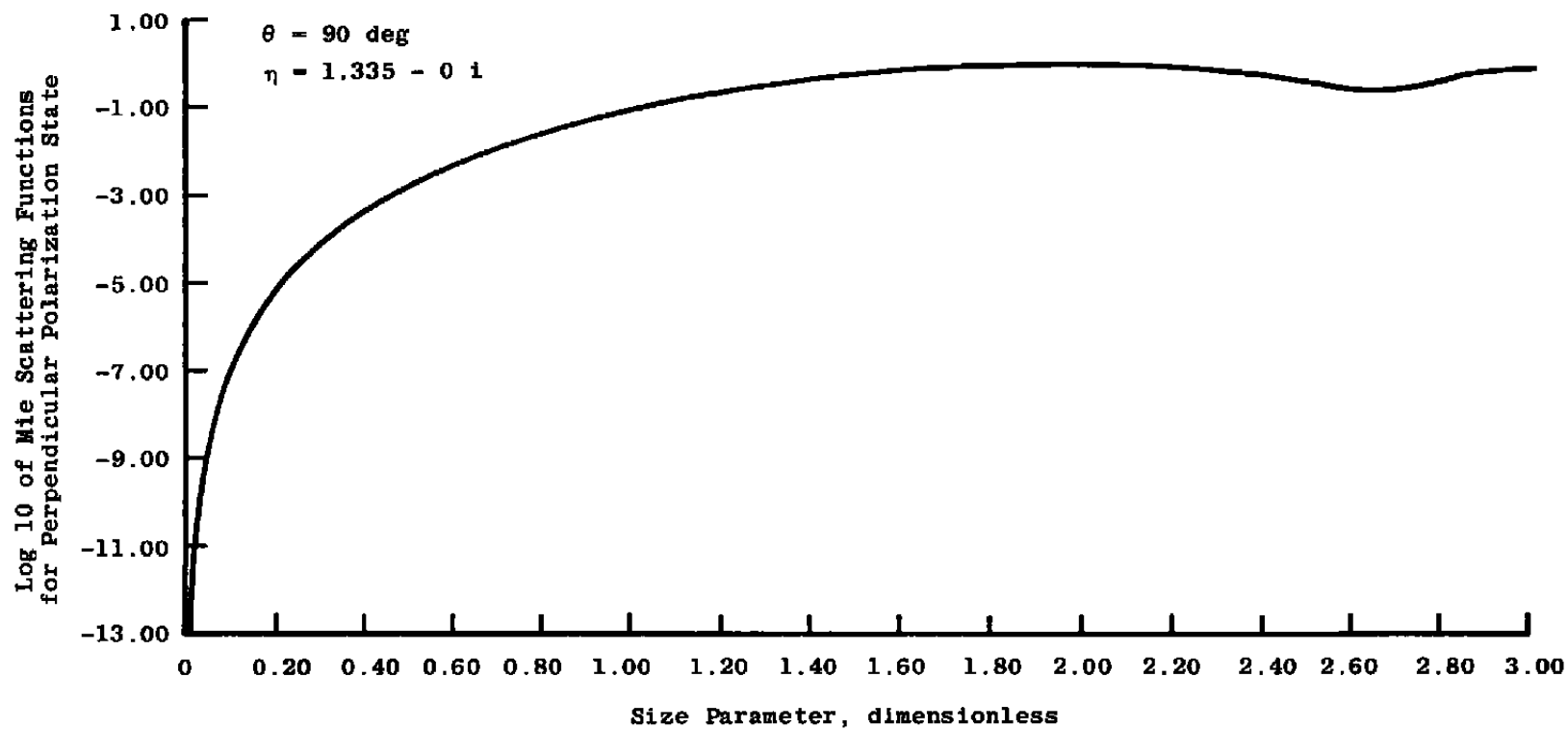
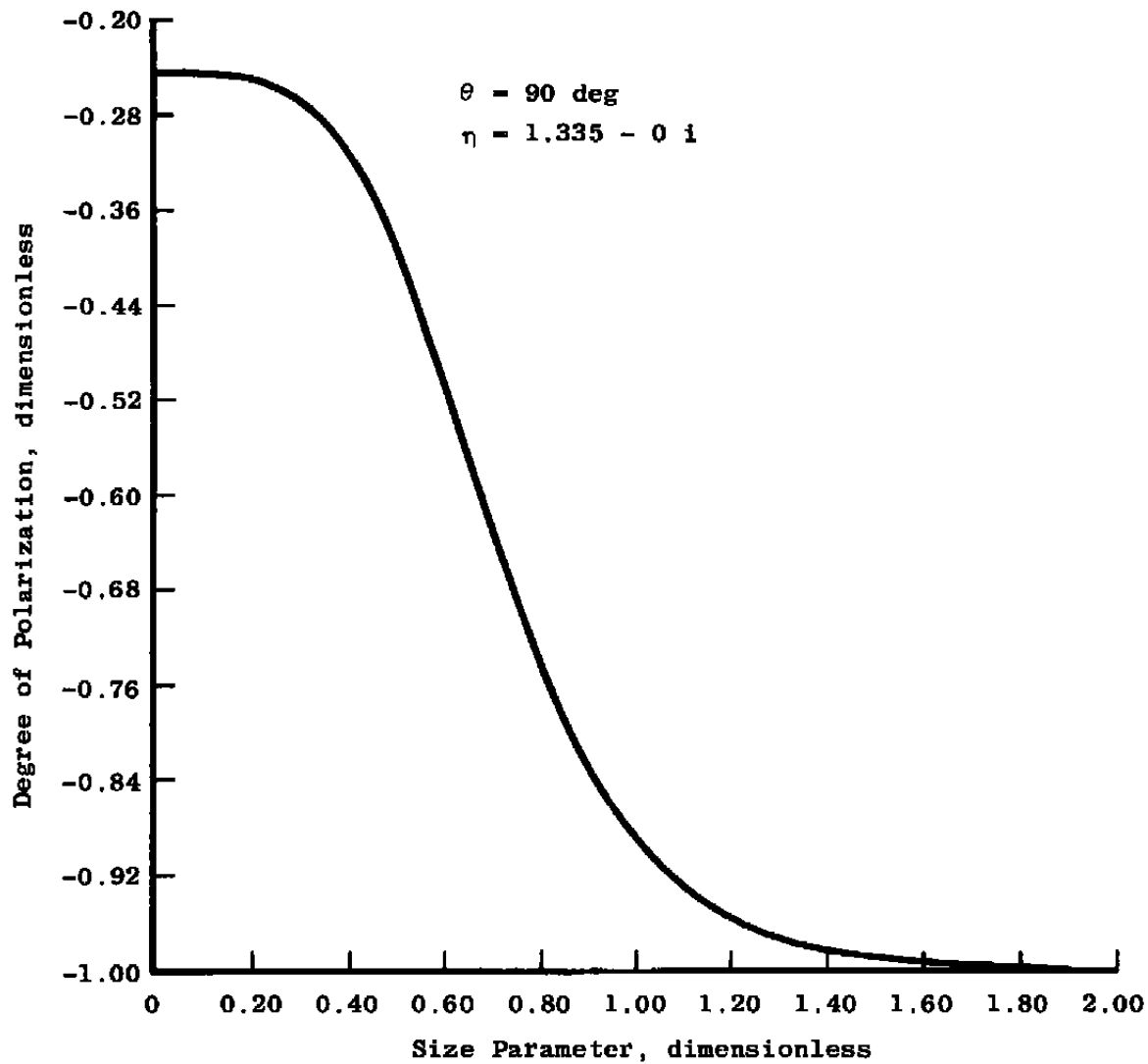


Figure 17. Size dependence of the perpendicular Mie scattering intensity functions in the geometry of Ref. 7.



**Figure 18. Size dependence of the degree of polarization of light scattered by very small droplets in the geometry of Ref. 7.**

**APPENDIX A**

**SIZFRED:  
A COMPUTER PROGRAM FOR SIZE DISTRIBUTION  
DECONVOLUTION BY  
FREDHOLM INVERSION OF MIE SCATTERING DATA**

B. P. Curry  
ARO, Inc.

## SUMMARY

This appendix is a user's manual for code SIZFRED, a program developed at AEDC for deconvolution of particle size distribution histograms obtained by single-wavelength, multiple-angle Mie scattering measurements. The experimental inputs to the code are Deconvolution Ratios (DECRATS), which are defined to be the calibrated signal in each orthogonal polarization state at each angular position, normalized by the unpolarized scattering signal in the 90-deg scattering channel. The incident laser polarization is assumed to be 45 deg with respect to the scattering plane.

Use of this code permits particle size deconvolution into as many as 30 size bins by using a maximum of 40 input ratios (DECRATS). The code incorporates error propagation analysis, and it includes a provision for estimating the upper bounds on the imprecision of each separate size bin in the deconvolved histograms. This option is activated whenever the estimated imprecision of each DECRAT is punched on the same input card as the corresponding DECRAT. The resulting deconvolution is a least-squares solution in which greatest weight is given the DECRATS having least imprecision. If DECRAT imprecision values are not specified, the code defaults to an option in which all DECRATS are equally weighted.

## A1.0 INTRODUCTION

Development and application of rapid, time-resolved in-situ particle diagnostics are essential for a complete understanding of rocket exhausts, wind tunnel flows, and other particulate-laden flows. Accurate diagnostics of polydisperse particle size distributions with diameters mainly in the micron and submicron range requires the use of experimental Mie scattering measurement techniques and appropriate computational procedures to deconvolve the distribution. This study was undertaken to provide a size deconvolution code (SIZFRED) that incorporates error propagation analysis and includes a procedure for identifying the optimum smoothing level of the deconvolved particle size histogram.

This appendix explains the theory and application of code SIZFRED to deconvolving particle size distribution functions from angular scattering data taken in both orthogonal polarization states. These states are defined as the scattered-light states in which the polarization vectors are perpendicular to and parallel to the plane containing the incident and scattered-light propagation direction (i.e., the scattering plane). SIZFRED assumes that the data in each polarization state from each angular channel have been normalized by the unpolarized signal from the 90-deg scattering channel.

The deconvolution ratios are input as follows: First, ratios for the perpendicular state are read into elements (1, N) of the DECRAT vector; the remaining elements ( $N + 1, 2N$ ) are the ratios corresponding to the parallel polarization state. Thus,  $2N$  DECRAT cards must be read in. (N is the number of angular channels, excluding the 90-deg reference channel.)

This program differs from an earlier computation in three important respects:

1. It has a provision for including estimated imprecision in the input deconvolution ratios.
2. It weights the scattering kernel matrix elements with the reciprocal of the variance of the appropriate signal, and it determines, with standard statistical procedures, the propagation of these estimated imprecision values into the final solution imprecision bands. Thus, 1-sigma input imprecision values produce solution imprecision bands which are the upper bounds to the corresponding 68-percent confidence limits.
3. It provides for estimating the optimum level of smoothing through locating the minimum in either or both of two goodness-of-fit criteria (GOOF). If there is no minimum in either parameter, then the GOOF parameters decline rapidly at first and then reach an asymptotic condition as a function of the smoothing parameter. The apparent inflection point at which this asymptotic behavior occurs can be considered the optimum smoothing point, provided that it occurs in a region in which the solution is non-negative.

In earlier simulation calculations with similar codes, the optimum smoothing point nearly always has occurred at a smoothing level such that all parameters of interest (including the solution vector) vary slowly with the smoothing parameter. Thus, the necessity for subjective judgments regarding when to stop smoothing has been somewhat alleviated in this code, as compared to its predecessors.

This appendix explains the use of the code and gives several examples of successful deconvolutions, some of which include the insertion of simulated "experimental error."

## A2.0 GENERAL THEORY

### A2.1 LIGHT-SCATTERING RATIOS

For a single-species, polydisperse ensemble of dielectric spheres, the ratio of power scattered from a localized focal volume (determined by the collection optics of the



experiment) to the incident power can be written (Refs. A-1 through A-4) in each orthogonal polarization state as follows:

$$\frac{\Phi_1(\theta_s, \phi_s, \eta)}{\Phi_0} = \frac{n\ell\Delta\psi_s}{k^2} \langle \sin^2 \psi_s \rangle \int_0^\infty f(x) \langle i_1(x, \theta_s, \eta) \rangle dx \quad (\text{A-1a})$$

$$\frac{\Phi_2(\theta_s, \phi_s, \eta)}{\Phi_0} = \frac{n\ell\Delta\psi_s}{k^2} \langle \cos^2 \psi_s \rangle \int_0^\infty f(x) \langle i_2(x, \theta_s, \eta) \rangle dx \quad (\text{A-1b})$$

where  $n$  is the number density of the particles,  $\ell$  is the projection of the focal volume on the incident laser axis (scattering length),  $k$  is the incident light wave number (inverse centimeters),  $f(x)$  is the normalized size distribution function, and  $x$  is the size parameter (ratio of circumference to wavelength) for a sphere of diameter  $D$ . The angles  $\theta$  and  $\psi$ , defined in the context of Fig. A-1, are, respectively, the polar scattering angle and the azimuthal angle for a particle that is located at the origin and illuminated from below (along the  $z$ -axis) by a laser whose electric field is polarized along the  $x$ -axis.  $\eta$  is the particle's complex index of refraction.

For purposes of analysis, computer-generated Mie scattering functions, integrated over the appropriate subtended angular range, are defined by the relations

$$\langle i_1(x, \theta_s, \eta) \rangle = \int_{\theta_s - \Delta\theta/2}^{\theta_s + \Delta\theta/2} i_1(x, \theta, \eta) \sin \theta d\theta \quad (\text{A-2a})$$

$$\langle i_2(x, \theta_s, \eta) \rangle = \int_{\theta_s - \Delta\theta/2}^{\theta_s + \Delta\theta/2} i_2(x, \theta, \eta) \sin \theta d\theta \quad (\text{A-2b})$$

with averaged azimuthal functions defined as

$$\begin{aligned} \langle \sin^2 \psi_s \rangle &= \frac{1}{\Delta\psi_s} \int_{\psi_s - \Delta\psi_s/2}^{\psi_s + \Delta\psi_s/2} \sin^2 \psi d\psi = \sin^2 \psi_s - \frac{\cos 2\psi_s}{2} \left( \frac{\sin \Delta\psi_s}{\Delta\psi_s} - 1 \right) \end{aligned} \quad (\text{A-2c})$$

$$\begin{aligned} \langle \cos^2 \psi_s \rangle &= \frac{1}{\Delta\psi_s} \int_{\psi_s - \Delta\psi_s/2}^{\psi_s + \Delta\psi_s/2} \cos^2 \psi d\psi = \cos^2 \psi_s + \frac{\cos 2\psi_s}{2} \left( \frac{\sin \Delta\psi_s}{\Delta\psi_s} - 1 \right) \end{aligned} \quad (\text{A-2d})$$

Although the above analysis is, strictly speaking, only appropriate for spheres, various modifications to Mie scattering theory have been developed to simulate the scattering by randomly oriented, polydisperse nonspherical scatterers. In such cases, the appropriately modified Mie functions correspond to the use of surface-equivalent diameters.

Because of the occurrence of the (unknown) number density in Eq. (A-1) and the difficulty of obtaining accurate absolute intensity measurements, deconvolutions are performed by using ratios of experimental scattering signals. Specifically, the data inputs are deconvolution ratios (DECRATS) which are defined as the ratio of the scattering signal in a given angular channel in each separate polarization state to the unpolarized 90-deg scattering signal. The 90-deg signal was chosen as a reference denominator because of its comparative insensitivity to the particle distribution function (PSDF) of the sample size. The implications of this form of DECRAT are explored in Ref. A-4.

## A2.2 CONSTRAINED LINEAR INVERSION

Insofar as the size dependence of the reference denominator can be ignored (thus treating the 90-deg signal as a normalization constant), Eq. (A-1) has the form, with respect to the size parameters, of Fredholm equations of the first kind. Phillips (Ref. A-5) and Twomey (Refs. A-6 through A-8) have developed a basic procedure for inverting such equations, taking full account of computational errors and random experimental "noise" in the measured inputs (DECRATS). Without allowance for these errors, the PSDF solutions of Eq. (A-1) are unstable and exhibit physically unrealistic oscillations and negative values. If the vector of input DECRAT values is denoted as  $\vec{G}$ , then Eq. (A-1) can be rewritten, allowing for error, in matrix form as (using the Einstein summation convention for repeated subscripts)

$$Q_{ki} (G_k + \epsilon_k) = M_{ij} F_j, \quad G_i = G(y_i), \quad F_j = \int_{x_{j-1}}^{x_j} f(x) dx \quad (A-3)$$

In Eq. (A-3),  $M$  is the symmetric scattering kernel matrix, defined as

$$M_{ij} = Q_{ki} Q_{kj}, \quad Q_{ij} = \int_{x_{j-1}}^{x_j} K(x, y_i) dx \quad (A-4)$$

The vector  $\vec{\epsilon}$ , introduced in Eq. (A-3), is comprised of the residual error associated with each DECRAT. These errors are computed from Eq. (A-3) after the solution vector  $\vec{F}$  has been computed. The norm of the residuals is also computed.

In Eq. (A-4), variables  $y$  and  $x$  represent, respectively, the angular variables and the size parameter. The specific relations that relate these equations to the light-scattering deconvolution problem are the following:

$$G_i = \frac{\Phi_1(\theta_i, \psi_i, \eta)}{\Phi_{ref}(\eta)}, \quad \Phi_{ref}(\eta) = [\Phi_1(\theta_o, \psi_o, \eta) + \Phi_2(\theta_o, \psi_o, \eta)], \quad \theta_o = 90 \text{ deg} \quad (\text{A-5})$$

$$\text{For } i = 1, 2, \dots, N$$

and

$$G_i = \frac{\Phi_2(\theta_i, \psi_i, \eta)}{\Phi_{ref}(\eta)}, \quad \theta_o = 90 \text{ deg} \quad \text{For } i = N+1, N+2, \dots, 2N \quad (\text{A-6})$$

where  $N$  is the number of angular channels. The associated scattering kernels are defined as

$$K(x, y_i) = \left( \frac{x_{max} - x_{min}}{x_j - x_{j-1}} \right) \quad (\text{A-7})$$

$$\times \frac{\frac{\Delta\psi_i}{\Delta\psi_o} \langle \sin^2 \psi_i \rangle \langle i_1(x, \theta_i, \eta) \rangle}{\int_{x_{min}}^{x_{max}} [\langle \sin^2 \psi_o \rangle \langle i_1(x, \theta_o, \eta) \rangle + \langle \cos^2 \psi_o \rangle \langle i_2(x, \theta_o, \eta) \rangle] dx}$$

$$\text{For } i = 1, 2, \dots, N$$

and

$$K(x, y_i) = \left( \frac{x_{max} - x_{min}}{x_j - x_{j-1}} \right) \quad (\text{A-8})$$

$$\times \frac{\frac{\Delta\psi_i}{\Delta\psi_o} \langle \cos^2 \psi_i \rangle \langle i_2(x, \theta_i, \eta) \rangle}{\int_{x_{min}}^{x_{max}} [\langle \sin^2 \psi \rangle \langle i_1(x, \theta_o, \eta) \rangle + \langle \cos^2 \psi_o \rangle \langle i_2(x, \theta_o, \eta) \rangle] dx}$$

$$\text{For } i = N+1, N+2, \dots, 2N$$

For practical reasons, the semi-infinite limits on the integrals in Eq. (A-1) have been replaced by minimum and maximum size parameters in Eqs. (A-7) and (A-8). Although these equations include general azimuthal forms, it is assumed henceforth that the incident laser polarization axis is oriented at 45 deg with respect to the scattering plane and that the subtended azimuths (but not subtended scattering angles) are the same for all angular channels. If such is not the case, the deconvolution code must be modified accordingly.

Twomey (Ref. A-5) has shown that the constrained least-squares solution of Eq. (A-3) can be stated for a given level of mean-square residual error as

$$\begin{aligned} F_i &= R_{ik}^{-1} Q_{jk} G_j, \\ R_{ik} &= M_{ik} + \gamma H_{ik} \end{aligned} \tag{A-9}$$

The function of the constraint is to select one of the infinite manifold of solutions which are possible as a result of the occurrence of error in Eq. (A-3). Here,  $\gamma$  is a Lagrange multiplier (the smoothing parameter); the matrix  $H$  is determined by the form of the constraint chosen, which, in this case, is maximum smoothness of the solution and is internally generated in the code. The matrices  $Q$ ,  $M$ , and  $R$  represent, respectively, the unsymmetric scattering kernel, symmetric scattering kernel, and smoothed symmetric scattering kernel matrices.

Twomey originally intended that the optimum value of the smoothing parameter be determined by increasing it from zero until the computed mean-square error equaled its corresponding experimental value. It turns out that the computed error is not monotonic in its variation with respect to the smoothing parameter (Ref. A-9), and simulated deconvolutions with included "noise" in the inputs show that the optimum smoothing parameter corresponds to a level of computed mean-square error that is considerably smaller than the simulated "experimental" noise input. Nevertheless, when a known distribution function is deconvolved from computed scattering data, a distinct minimum in the variance of the distribution is found (Ref. A-9). It is fortunate that optimum smoothing generally occurs in a region in which the variation of the deconvolution solution with  $\gamma$  is relatively slow. An approximate procedure for locating the optimum smoothing level will be discussed later.

The need for smoothing arises because of the sensitivity of Eq. (A-3) to error. Twomey (Ref. A-7) has shown that whenever any eigenvalue of the symmetric kernel matrix is not significantly larger than the ratio of the norm of the computed error to the norm of the solution vector, then the kernel is, for practical purposes, singular, and the number of independent measurements must be reduced by one for each eigenvalue for which this is true. The smoothing process systematically suppresses the eigenvectors

corresponding to eigenvalues that are approximately equal to the current value of the smoothing parameter; this can be seen by observing the change of the eigenvalues printed out by the code at each value of the smoothing parameter.

Twomey's criterion for the degree of independence of the measurements can be exploited to yield an indication of the resolution attainable in a given series of measurements (i.e., the number of size bins which can be accurately deconvolved in a solution histogram). In scattering experiment simulations performed at AEDC, 15-, 30-, 45-, 135-, 150-, and 90-deg angles have been used; both polarization states have been used, and the particles have been assumed to be  $Al_2O_3$ , illuminated by 0.5145- $\mu$  light. For these conditions, the eigenvalue criterion indicated that good deconvolutions could be obtained for a maximum of six bins, and the simulated deconvolutions, even including input "noise" obeyed this rule of thumb. For eight bins, non-physical behavior was manifested by the tendency of the solution to change rapidly with smoothing parameter from a form having negative mole fraction values to an asymptotic "monotonic staircase," declining form. Whenever physical information is present in the solution, there is a wide range of smoothing parameters in which the solution exhibits a slow transition between the extremes mentioned above.

A family of codes denoted as SIZSIM was previously constructed on the basis of the constrained linear inversion technique. In all these codes, error propagation was considered only for the computation of residual errors. In one of these codes, experimental limitations prevented the use of the 90-deg reference signal. In this code, the reference signal was taken to be a composite of the unpolarized signals from all of the angular channels. Results of this analysis are reported in Ref. A-4.

### A2.3 MODIFICATIONS TO INCLUDE DECRAT ERRORS

In constructing code SIZFRED, use has been made of three statistical modifications of the basic constrained linear inversion technique. These modifications permit SIZFRED to weight the DECRATS inversely proportional to the level of imprecision associated with each DECRAT. In addition, upper bound output imprecision bands associated with each size bin are computed from a statistical error propagation analysis. Finally, goodness-of-fit parameters have been devised to minimize the subjectivity associated with determination of the optimum smoothing level of the deconvolutions.

The first modification was reported, in the context of constrained linear inversion, in Ref. A-10, although similar techniques are discussed in standard statistical references such as Ref. A-11. This modification is implemented in SIZFRED by redefining the symmetric kernel matrix as shown below:

$$M_{ij} = \sum_k Q_{ki} Q_{kj} / (\delta G_k)^2 \quad (A-10)$$

In Eq. (A-10) the set of quantities  $\{\delta G_k\}$  denotes the input imprecision values associated with each DECRAT, and the input errors are assumed to be uncorrelated (i.e., it is assumed that the input covariance matrix has only diagonal terms, and these are the squares of the input imprecision values). The imprecision-weighted solution is

$$F_i = \sum_j R_{ik}^{-1} Q_{jk} G_j / (\delta G_j)^2 \quad (A-11)$$

The second modification of the basic inversion technique is also a simple generalization of standard statistical procedures presented in Ref. A-11; however, the implications of this generalization are subtle and far reaching, as discussed in detail in Ref. A-12.

If the input errors are assumed to be statistically independent, then the upper bounds on the output imprecision bands can be computed for each size bin from the square roots of the variances written below:

$$\delta^2 F_i = \sum_k M_{ij}^{-1} Q_{kj} (\delta G_k)^2 Q_{ki} M_{ii}^{-1} \quad (A-12)$$

(Note that this equation is not summed over "i".) Upper and lower bound estimates to the solution histogram are obtained by adding the square roots of the above variances to — or subtracting these quantities from — the solution histogram in each size bin.

Reference A-12 shows that, because of the use of constraints in the deconvolution procedure, the extent to which these relations overestimate the true output imprecision bands cannot be assessed. Therefore, a conservative estimate on the confidence limits is provided with which the histogram solutions should be associated. For example, if the DECRAT imprecision values specified as inputs to SIZFRED correspond to 1-sigma values (68-percent confidence level), the code will yield output imprecision bands with the following nature: The probability exceeds 0.68 that solutions which have random input error falling within the stated imprecision bands will lie within the computed output imprecision bands.

In reality, there is little certainty that an input Gaussian error distribution will propagate as an output Gaussian error distribution. Hence, the precise meaning of the output imprecision bands can be determined only by performing a statistically significant number of simulated deconvolutions of computer generated scattering data with various levels of Gaussian distributed error, the standard distribution of which corresponds to the imprecision value stated for each DECRAT and the mean of which corresponds to each DECRAT. Ideally, at least 20 such computer runs should be made for each of the three

types of size distribution functions considered here. However, such a comprehensive study is beyond the scope of this report.

The third statistical modification to the basic deconvolution technique is an attempt to determine goodness-of-fit parameters that will reduce the subjectivity associated with determining the optimum value of the smoothing parameter. Using strictly heuristic arguments, goodness-of-fit parameters have been derived by considering the propagation of the residual error and including the magnitude of the smoothing parameter, relative to the eigenvalues of the smoothed, symmetric kernel matrix. Since it is not known a priori how much to weight each eigenvalue, the goodness-of-fit parameters are defined as shown below for two different ways of incorporating the eigenvalues:

$$\Delta_{A,B}^2 = \sum_k R_{ij}^{-1} Q_{ki} \epsilon_k^2 Q_{kl} R_{li}^{-1} f(y) \quad (A-13a)$$

$$f_A(y) = \ln \left[ \frac{y^M}{\left( \prod_{i=1}^M \lambda_i \right)} \right]^{1/M} \quad (A-13b)$$

$$f_B(y) = \left[ \prod_{i=1}^M \ln(y/\lambda_i) \right]^{1/M} \quad (A-13c)$$

Here  $M$  is the number of size bins in the histogram. Equations (A-13b) and (A-13c), which introduce weighted geometric means of the smoothing parameter/eigenvalues ratios, are used in the goodness-of-fit parameters respectively denoted GOOF A and GOOF B.

### A3.0 DETAILS OF CODE SIZFRED

A flow chart of code SIZFRED is shown in Fig. A-2. The program requires that precomputed Mie intensity functions be read in at equal subintervals of size parameter for each of the  $N+1$  angles at which experimental data are to be entered. These functions must have the form shown in Eq. (A-2). The code assumes that the last angle is the reference angle (presumably 90 degrees). The tape files (which are generated by using code MIESTEP) must fit the following format: The first variable is the scattering angle, the second is the size parameter, the third is the perpendicular Mie function, and the fourth is the parallel Mie function. It is assumed that the Mie functions have been integrated over the experimental range of subtended scattering angle. If the trapezoidal rule is used for the angular integration, numerical instabilities prevent the use of scattering kernels with subtended scattering angles greater than about one degree. Angular integration by means of Gaussian quadrature, however, allows larger subtended angles to be used, and it is recommended that the kernels be computed using 16-point Gaussian

quadrature. No attempt has been made to determine the maximum permissible subtended angles, but, clearly, the greatest accuracy is obtained by limiting the subtended angles to the smallest values consistent with adequate counting statistics and signal-to-noise ratio.

Table A-1 shows the nomenclature for the variables that the code user requires, and Table A-2 shows the order in which inputs to the code must be made. Subroutine MIEFILE—a binary search routine—extracts the appropriate Mie functions from the tape file and sends them to the numerical integration subroutines, which then return values from which the elements of the unsymmetric scattering kernel matrix are constructed. MIEFILE includes a variety of error tests; Table A-3 defines the resulting error messages that the code will print if various conditions are not met.

Once the unsymmetric kernels have been constructed, the code symmetrizes these matrices and, if the input imprecision values have been stated, weights them according to the DECRATS having the least imprecision. The symmetric scattering kernel matrix is then added to the product of the smoothing parameter and an internally generated smoothing matrix, and the resultant smoothed kernel matrix is inverted with use of Cholesky's method. In addition, eigenvalues of the smoothed kernels are computed. The matrix inversion routine includes a test to determine at which step in Cholesky's factorization process significant digits may have been lost. This test is necessary because Cholesky's method requires that the matrix being inverted be positive definite, and loss of significant digits can cause the matrix to lose its positive definite nature. To use this error check correctly, one must determine the error criterion, EPS, by trial and error. Generally, a value on the order of 0.000001 works fairly well.

A much more definitive error test is provided by multiplying the original and inverted matrices and by then testing pairs of elements along the diagonal. When the code indicates inaccuracies in the  $n$ th significant digit, off-diagonal elements of the product matrix (which should be the identity matrix) have magnitudes on the order of the  $n+1$ th significant digit. Thus, the inversion error criterion is conservative.

After matrix inversion, the code computes the solution histogram, the residual error vector, the norm of the residuals, and the relative norm of the residuals (the residuals' norm is divided by the DECRATS' norm). If the input imprecision values have been stated, then the code computes output imprecision bands and prints the upper and lower bounds, as well as the computed histogram, for each diameter bin. As an additional check on the occurrence of computational error, the code also computes the solution corresponding to zero smoothing level, even if the starting value of the smoothing parameter is nonzero. Finally, the two goodness-of-fit parameters, GOOF A and GOOF B, are computed and printed. This process is repeated until value of the smoothing



parameter equals or exceeds its stop value, EPST. At this point the computer generates a histogram plot. The last card of the input deck specifies the plot parameters. The first variable on this card is the minimum diameter that will be plotted and the second is a scale factor. For six-bin histograms this factor should be 0.25.

#### A4.0 ILLUSTRATIVE SIZING CALCULATIONS

Simulated PSDF deconvolutions have been performed on the three types of distribution functions shown in Figs. A-3 through A-5. The polarized angular scattering distributions corresponding to the size distribution of Fig. A-3 are shown in Fig. A-6. The corresponding DECRATS for the previously given scattering angles are listed in Tables A-4 through A-6 for the three size distributions shown in Figs. A-3 through A-5.

When a deconvolution of the data in Table A-4 is attempted without specifying the (arbitrarily chosen, but presumably typical) set of imprecision values stated in Table A-4, no minimum is found in either GOOF parameter. Plotting these parameters against the smoothing parameter,  $\gamma$ , however, reveals that a value in the range from 0.004 to 0.006 should be nearly optimum; the solution changes negligibly within this range. The resulting deconvolution is shown in Fig. A-7 and can be compared with the original size distribution function in Fig. A-3 by dividing the computed size histogram mole fractions by the histogram bin size.

The result of deconvolution involving the stated imprecision values (of Table A-4) is shown in Fig. A-8. The histogram corresponds to a minimum in the GOOF B parameter, which occurred when the smoothing parameter just exceeded the smallest eigenvalue of the smoothed kernel matrix. Because of the dominance of the scattering functions by larger particles, the imprecision of the smallest size bin is rather large. A dramatic improvement occurs, however, when the magnitude of all the input imprecision bands is halved, as shown in Fig. A-9. Similar but even more dramatic improvement in output imprecision is shown in the deconvolution of the simulated bimodal distribution (Figs. A-4, A-10, and A-11). The DECRATS corresponding to this case were obtained by averaging the scattering functions obtained from two narrow Deirmendjian distribution functions. A previous attempt to resolve bimodal distributions with closely spaced peaks was unsuccessful. Minima in both GOOF parameters were found in the successful bimodal deconvolutions. The solution histograms differed very little for the two minima.

Figures A-5 and A-12 are included to illustrate the ability of the deconvolution procedure to treat a very narrow distribution function. It was feared that the technique would attempt to "fill up" empty bins, but Fig. A-12 shows that this did not happen. For the smoothing parameter increment used, it was not possible to find a solution in which there were no negative mole fractions (though the magnitude of the negative mole

fractions is quite small). Although Fig. A-12 does correspond to an optimum smoothing level, it is likely that a smaller increment of smoothing parameter could have located histograms near the optimum smoothing level for which only positive mole fraction values occurred. Nevertheless, Fig. A-12 shows that SIZFRED will not fill up empty size bins unless the smoothing parameter is allowed to become so large that clearly unphysical results occur.

As previously stated, it is beyond the scope of this work to perform a detailed test of the propagation of error distribution shapes through the deconvolution procedure. However, a few test cases have been investigated that had simulated error included in the DECRATS. Figure A-13 shows the deconvolution resulting from simulating error occurrence only in DECRAT 1, as shown in Table A-7. A more stringent test is afforded by simulating Gaussian distributed errors as shown in Table A-8. For this set of errors (corresponding to the imprecision values in Table A-4), the eigenvalue criterion shows that a six-bin deconvolution cannot be obtained; this is confirmed by the behavior of the solution histogram as  $\gamma$  is increased. The same criterion indicates that a five-bin histogram can be obtained. The result corresponding to a minimum in GOOF A is shown in Fig. A-14. Better results are obtained by increasing the smoothing parameter until the two GOOF parameters agree to within about 20 percent, as shown in Fig. A-15. However, this result must be regarded as fortuitous until more extensive tests with other distribution functions and other error distributions can be conducted.

Decreasing the input imprecision by a factor of two and recomputing a Gaussian error distribution (Table A-9) result in a six-bin deconvolution that is marginally allowed by the eigenvalue criterion (Fig. A-16). Again, the histogram corresponding to near equality of the GOOF parameters is superior to that corresponding to a minimum in either parameter.

## A5.0 CONCLUDING REMARKS

The primary objectives of this study were to incorporate error propagation analysis into AEDC's size deconvolution codes and to develop a means of identifying the optimum smoothing level with as little subjectivity as possible. Code SIZFRED has been developed to accomplish these objectives. Although some judgement must still be exercised in determining the optimum smoothing level and in determining whether the results are physically meaningful, progress toward minimizing the subjectivity has been achieved by the introduction of two goodness-of-fit parameters. Extensive testing of the code must yet be undertaken to determine the extent of transformation of a Gaussian error distribution by error propagation and to determine how such error propagation transformations affect the characteristics and usefulness of the existing error criteria.

The effects of other uncertainties, such as particle nonsphericity and complex refractive index uncertainty, have not been addressed. Ideally, the deconvolution procedure should be tested further by simulating polydisperse multispecies scattering, perhaps using approximate nonspherical scattering functions. The code should also be tested in laboratory scattering experiments with polydispersions of scatterers with known properties, such as commercially available latex spheres.

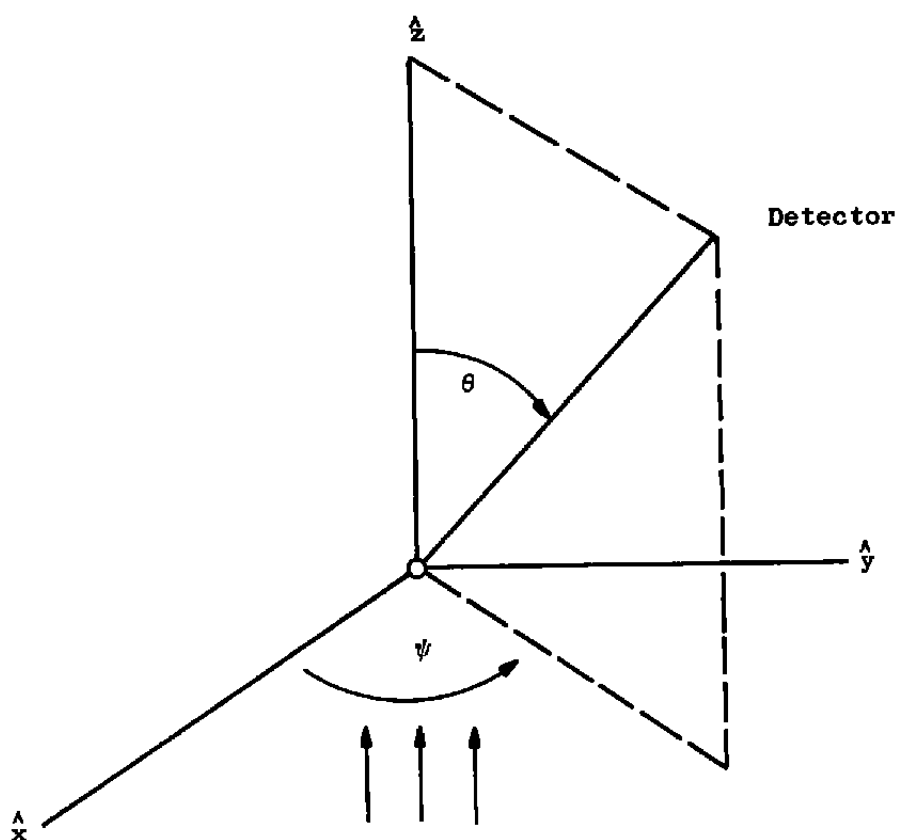
As configured presently, code SIZFRED can accept inputs from 21 scattering angles (in both polarization states) and will produce deconvolutions with up to 30 size bins (depending on angular detector locations, error levels, etc.). Whether such experimental complexity is justified, in terms of attainable size resolution, has not been addressed. Parametric studies should be carried out with various size distributions and varying error levels to attempt to optimize the number of detector channels needed and their angular locations.

These preliminary results show that the deconvolution procedure is stable for errors as large as  $\pm 3$  to 5 percent in each DECRAT and at the expense of loss of histogram resolution (i.e., number of bins). Moreover, if the input errors are restricted to  $\pm 1$  to 3 percent, then these studies also suggest that deconvolution can be achieved without significant loss of size resolution and with substantial decrease in output imprecision in small particle size mole fractions. To the extent that it is practical, experimental applications should be directed toward achieving these detection imprecision levels.

## REFERENCES

- A-1. Hulst, Hendrik Christoffel van de. Light Scattering by Small Particles. John Wiley and Sons, Inc., New York, 1957.
- A-2. Kerker, Milton. The Scattering of Light, and Other Electromagnetic Radiation. Academic Press, New York, 1969.
- A-3. Born, Max and Wolf, Emil. Principles of Optics: Electromagnetic Theory of Propagation, Interference and Diffraction of Light. Pergamon Press, New York, 1959.
- A-4. Lewis, J. W. L., Curry, B. P., and Weaver, D. P. "Determination of the Size Distribution Function for Particles in a Hypersonic Flow Field." AEDC-TR-77-101 (AD-A056923), July 1978.
- A-5. Phillips, David L. "A Technique for the Numerical Solution of Certain Integral Equations of the First Kind." Journal of the Association for Computing Machinery, Vol. 9, 1962, pp. 84-97.

- A-6. Twomey, S. "On the Numerical Solution of Fredholm Integral Equations of the First Kind by the Inversion of the Linear System Produced by Quadrature." Journal of the Association for Computing Machinery, Vol. 10, 1963, pp. 97-101.
- A-7. Twomey, S. "The Application of Numerical Filtering to the Solution of Integral Equations Encountered in Indirect Sensing Measurements." Journal of the Franklin Institute, Vol. 279, 1969, pp. 95-109.
- A-8. Twomey, S. and Howell, H. B. "Some Aspects of the Optical Estimation of Microstructure in Fog and Cloud." Applied Optics, Vol. 6, No. 12, December 1967, pp. 2125-2131.
- A-9. Shaw, Glenn E. "Inversion of Optical Scattering and Spectral Extinction Measurements to Recover Aerosol Size Spectra." Applied Optics, Vol. 18, No. 7, April 1979, pp. 988-993.
- A-10. King, Michael D., Byrne, Dale M., Herman, Benjamin M., and Reagan, John A. "Aerosol Size Distributions Obtained by Inversion of Spectral Optical Depth Measurements." Journal of the Atmospheric Sciences, Vol. 35, No. 11, November 1978, pp. 2153-2167.
- A-11. Mathews, John and Walker, R. L. Mathematical Methods of Physics. W. A. Benjamin, Inc., New York, 1964.
- A-12. Burrus, W. R. "Utilization of A Priori Information by Means of Mathematical Programming in the Statistical Interpretation of Measured Distributions." Oak Ridge National Laboratory, ORNL Report 3743, June 1965.



Incident light propagates along  $z$ -axis.  
Incident electric field polarization is along  $x$ -axis.

**Figure A-1. Schematic diagram for scattering by a single sphere at the origin.**

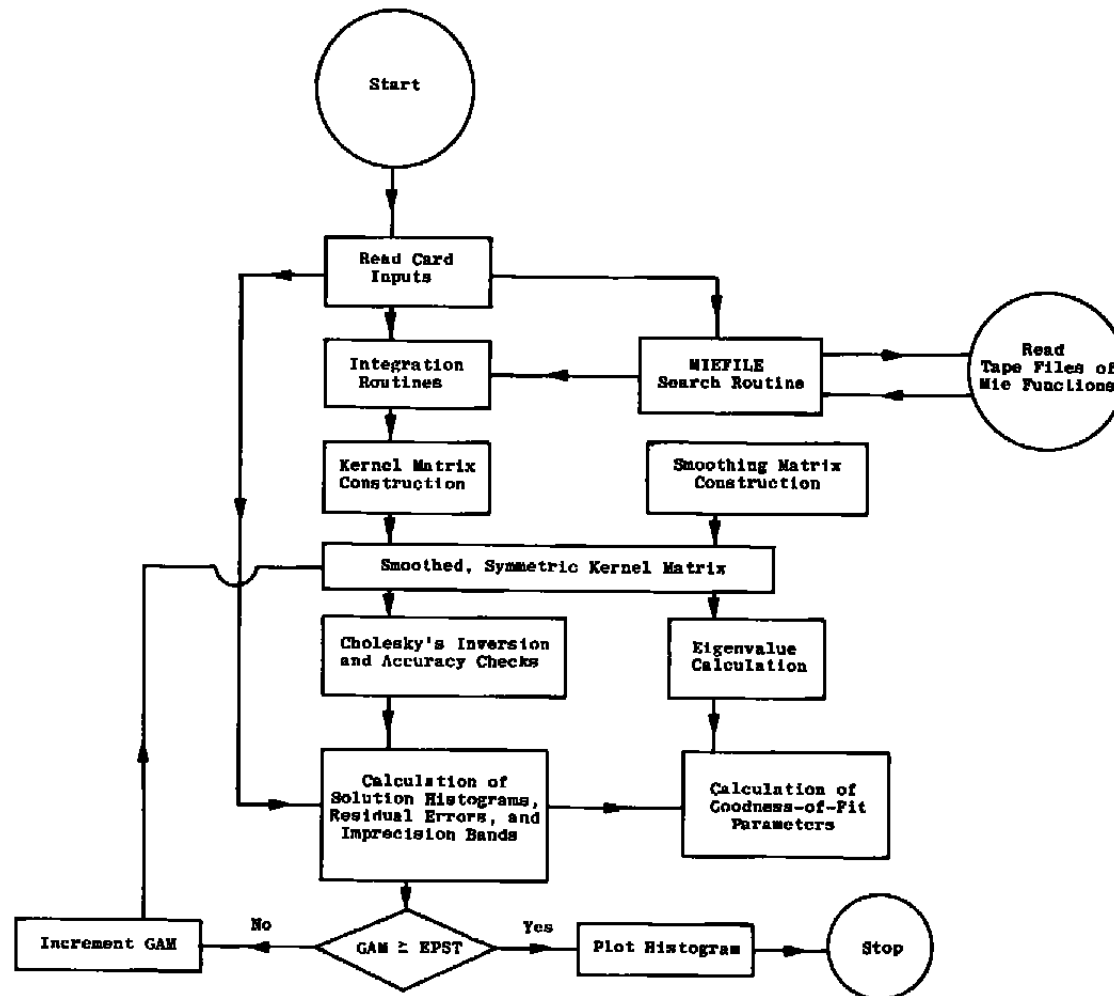
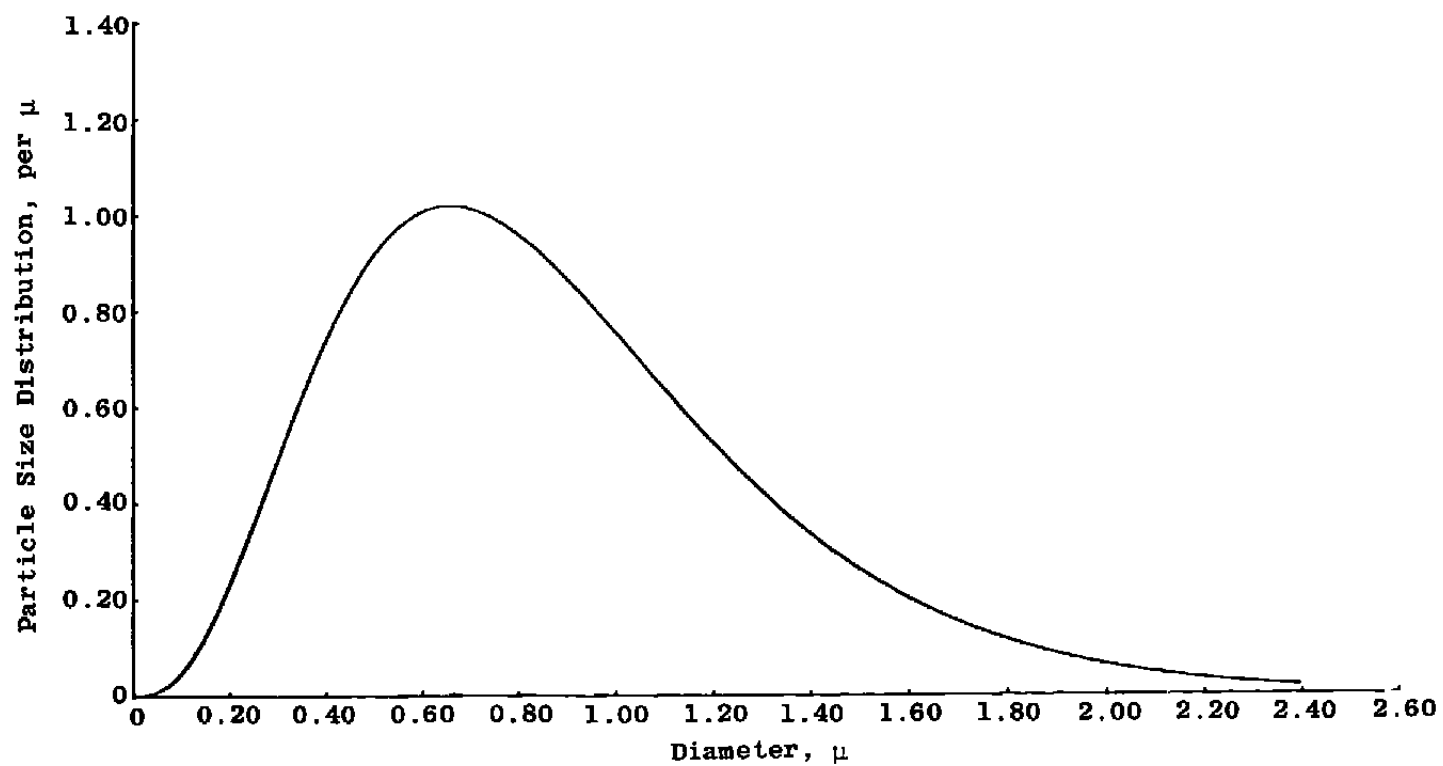
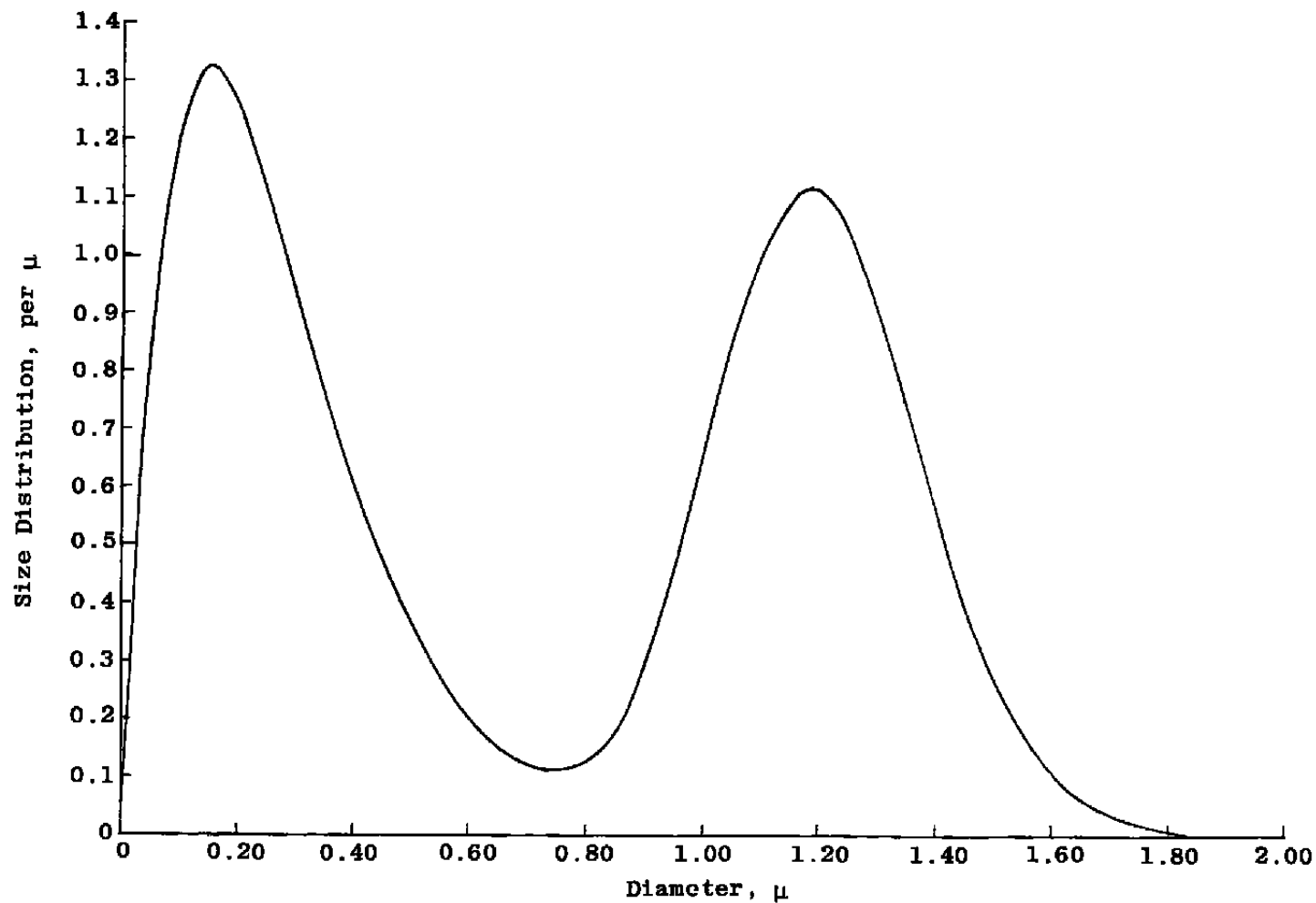


Figure A-2. Flow chart of code SIZFRED.



**Figure A-3. Standard size distribution function for test of deconvolution procedure.**



**Figure A-4. Bimodal size distribution function for test of deconvolution procedure.**



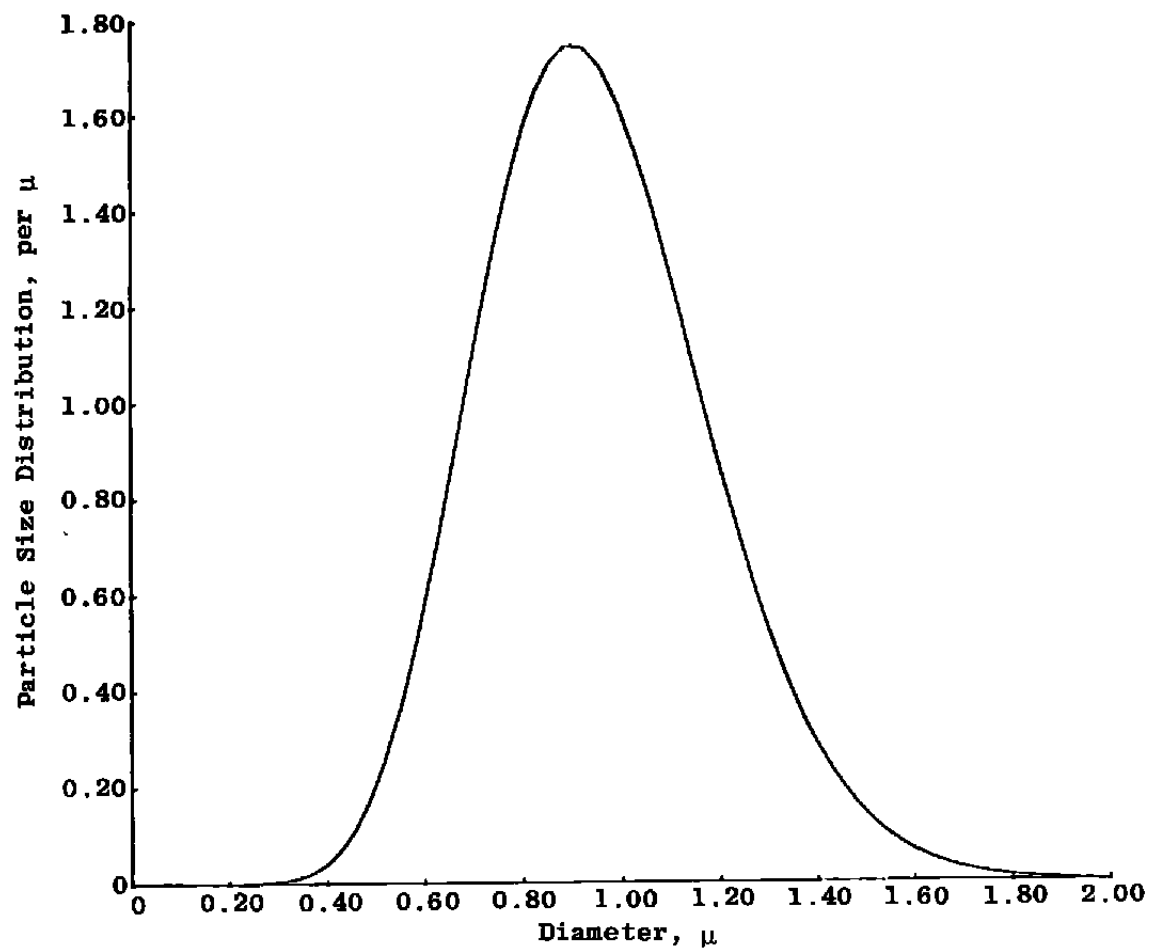
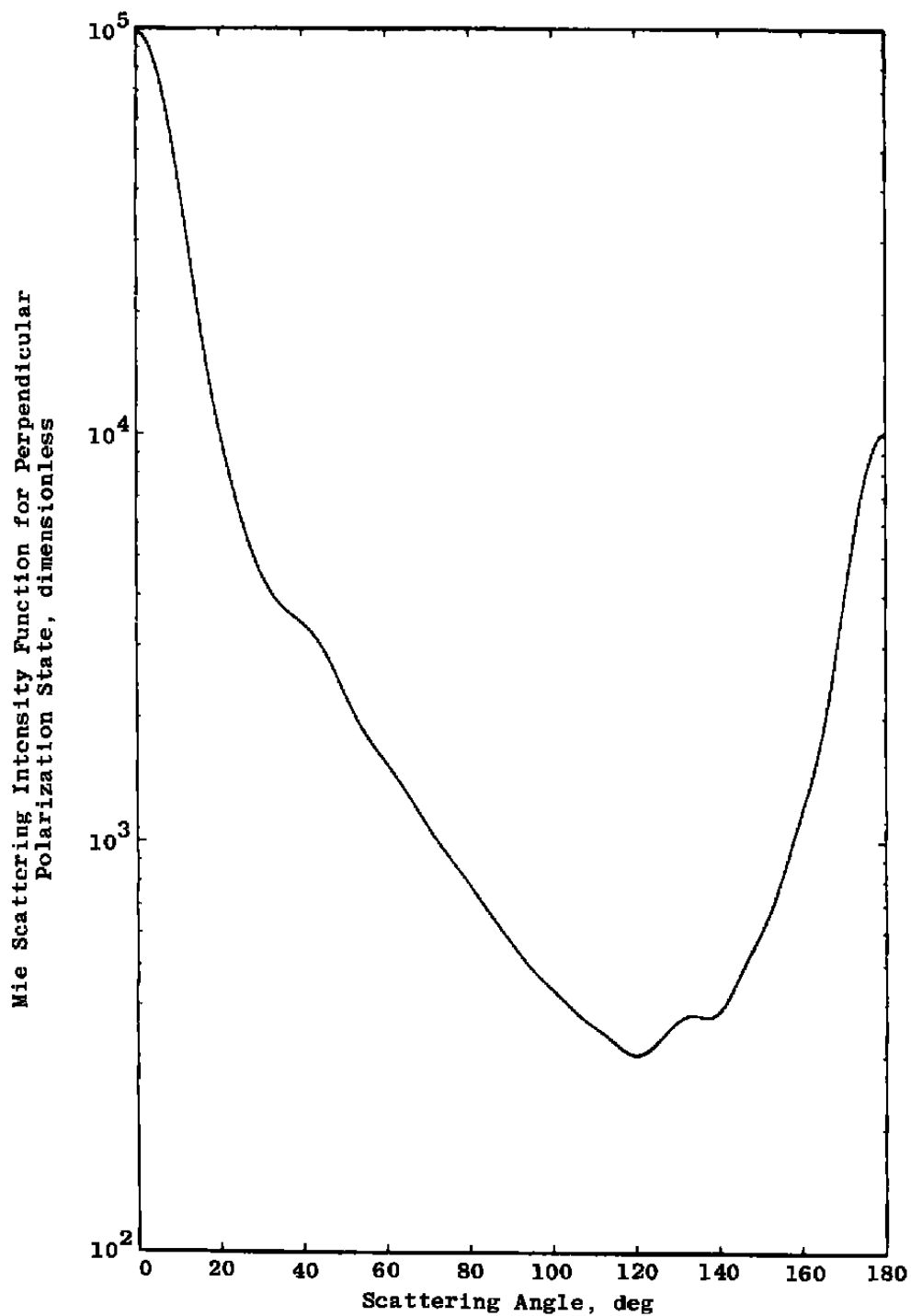
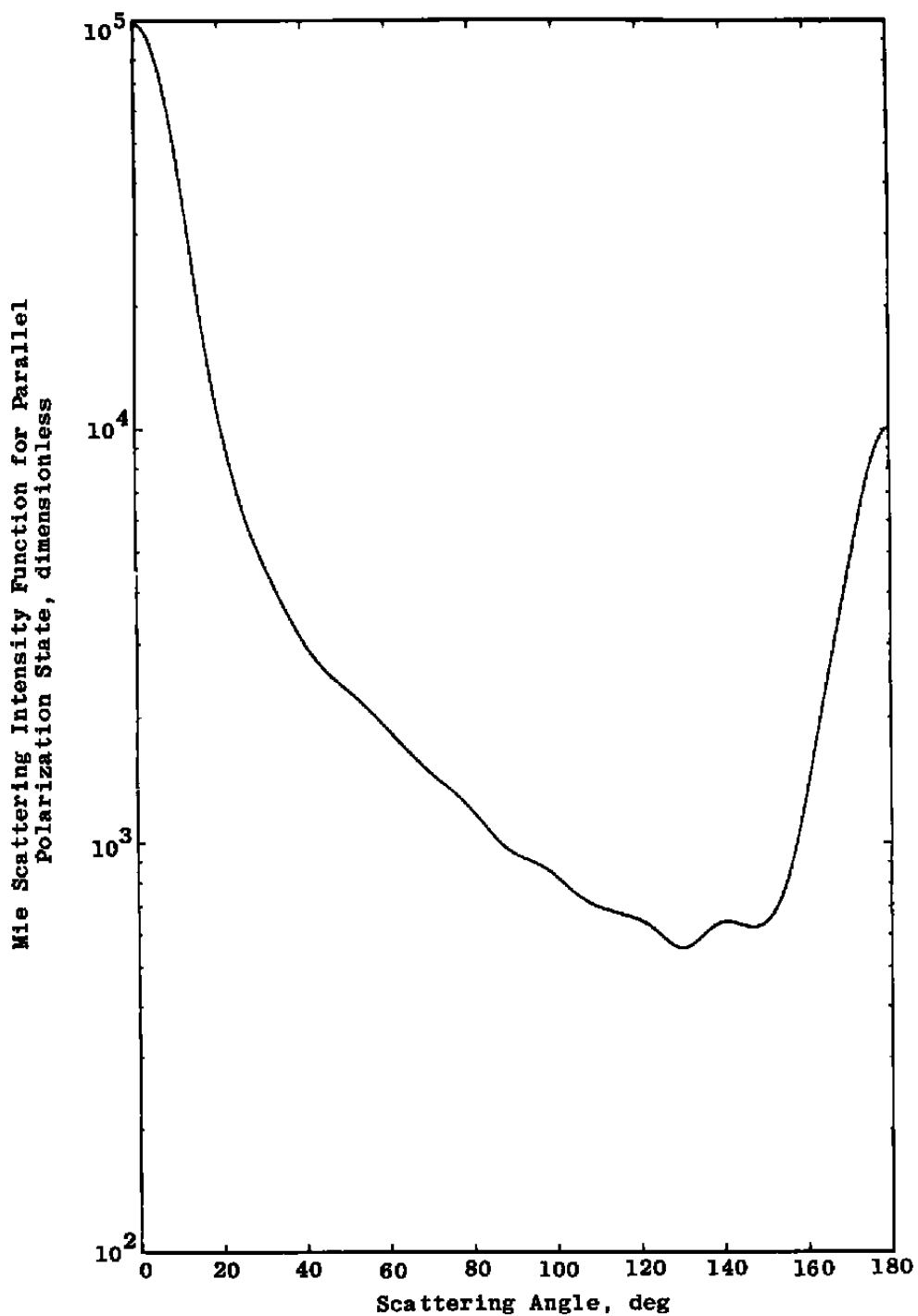


Figure A-5. Center-peaked size distribution function for test of deconvolution procedure.



a. Perpendicular

**Figure A-6.** Angular scattering distribution of Mie intensity functions for the standard size distribution (Fig. A-3) of aluminum oxide particles.



b. Parallel  
Figure A-6. Concluded.

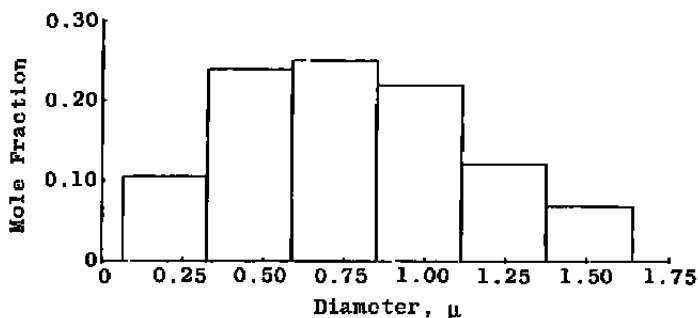


**Figure A-7. Deconvolution histogram obtained from DECRATS in Table A-4 without using stated input imprecision values (corresponds to standard size distribution function).**

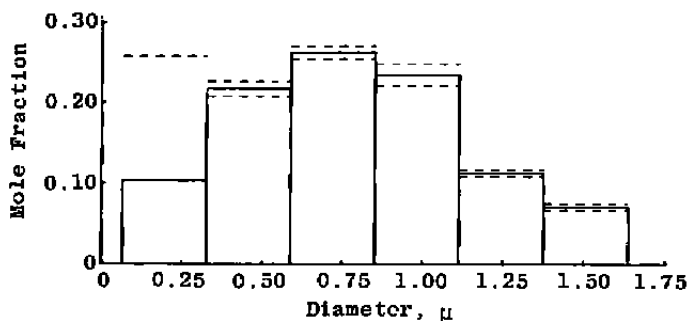


**Figure A-8. Deconvolution histogram obtained from DECRATS in Table A-4 using stated input imprecision values (corresponds to standard size distribution function).**

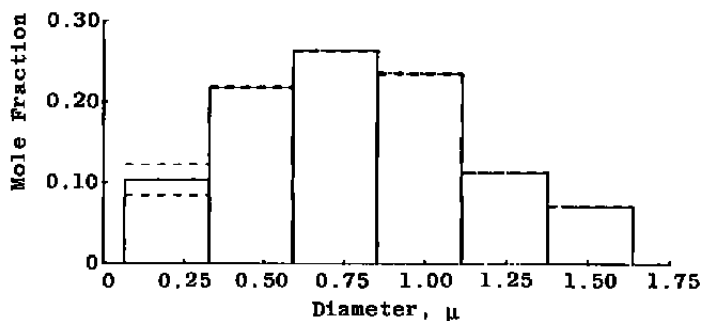


**Figure A-9. Deconvolution histogram obtained from DECRATS in Table A-4 using  $\frac{1}{2}$  stated input imprecision values (corresponds to standard size distribution function).**

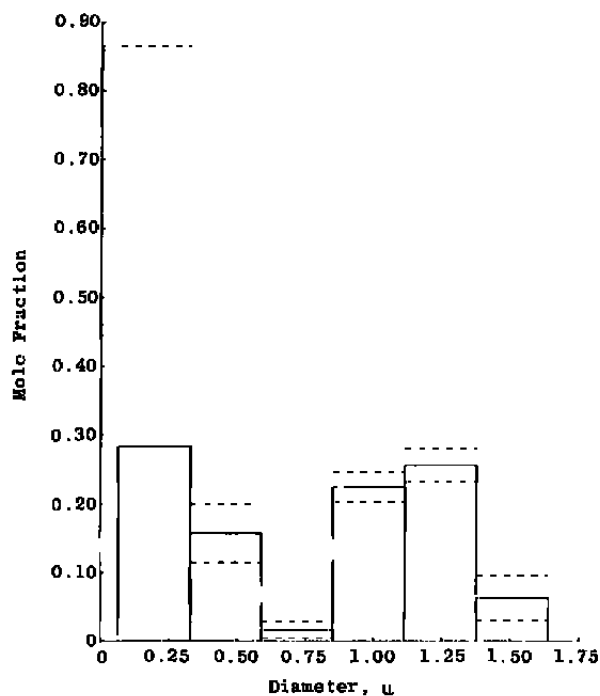


**Figure A-10. Deconvolution histogram obtained from DECRATS in Table A-5 using stated Imprecision values (corresponds to bimodal size distribution function).**

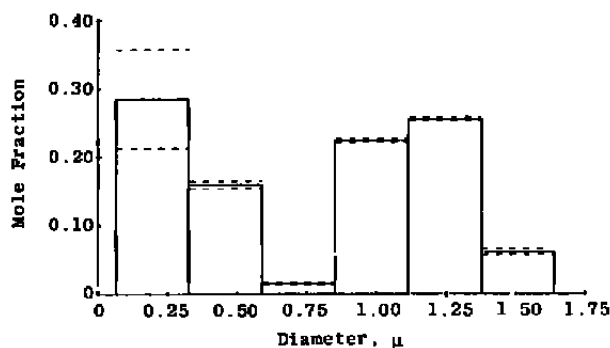


**Figure A-11. Deconvolution histogram obtained from DECRATS in Table A-5 using ½ stated input imprecision values (corresponds to bimodal size distribution function).**

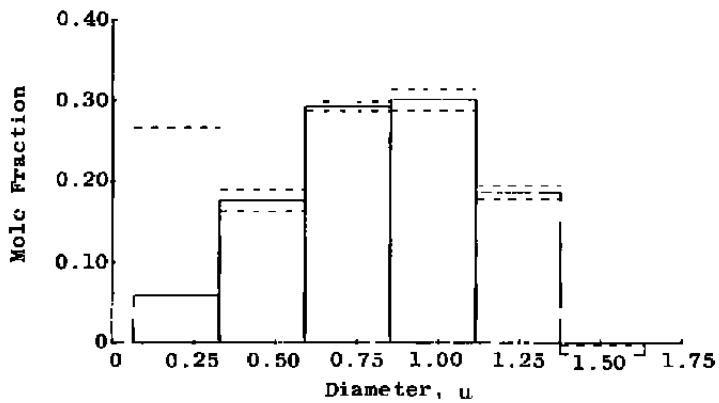


**Figure A-12.** Deconvolution histogram obtained from DECRATS in Table A-6 using stated input imprecision values (corresponds to center-peaked distribution).

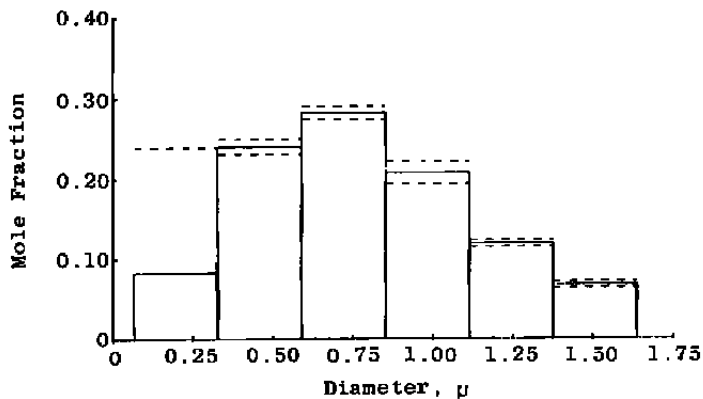


**Figure A-13.** Deconvolution histogram obtained from DECRATS in Table A-7 using stated input imprecision values (corresponds to standard size distribution function with 8.6-percent error inserted into DECRAT 1 only).

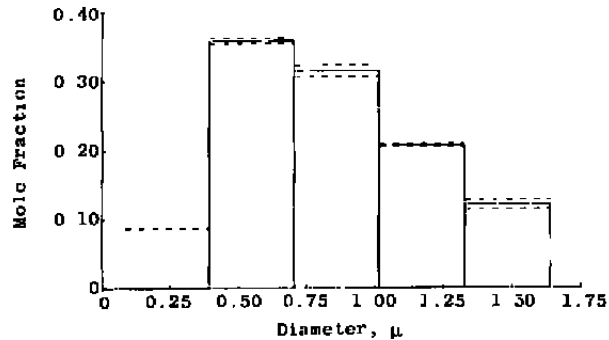


**Figure A-14.** Five-bin deconvolution histogram obtained from DECRATS in Table A-8 using optimum solution based on minimum in GOOF A (corresponds to standard size distribution function with Gaussian error distribution inserted into all DECRATS)

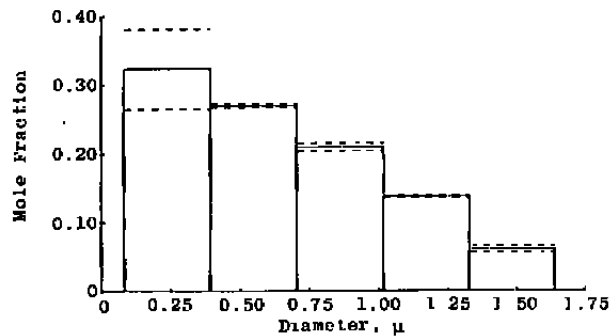


**Figure A-15.** Five-bin deconvolution histogram obtained from DECRATS in Table A-8 using optimum solution based on equivalence of GOOF A and GOOF B to 20-percent (corresponds to standard size distribution function with Gaussian error distribution inserted into all DECRATS)

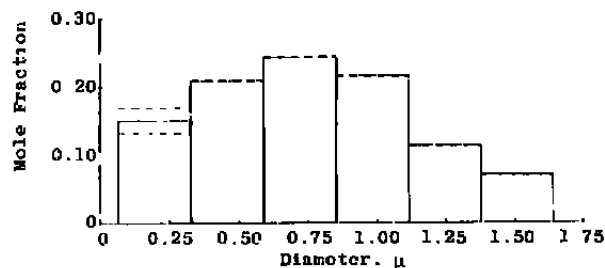


**Figure A-16.** Six-bin deconvolution histogram obtained from DEGRATS in Table A-8 using optimum solution based on equivalence of GOOF A and GOOF B to 20-percent (corresponds to standard size distribution function with Gaussian error distribution inserted into all DECRATS).

**Table A-1. Nomenclature Used in Code SIZFRED**

THETA (I); I=1,N	Scattering angle, deg
THETAR = Theta (n+1)	Reference angle, deg
DMAX	Maximum particle diameter, $\mu$ , considered for histogram
DMIN	Minimum particle diameter, $\mu$ , considered for histogram
HSIZ	Size parameter increment at which Mie functions have been recorded on tape called by code SIZFRED
HDIAM	Diameter increment, $\mu$ , corresponding to HSIZ
SIZMAX	Size parameter corresponding to DMAX
SIZMIN	Size parameter corresponding to DMIN
DELBIG	SIZMAX - SIZMIN
$L = \frac{SIZMAX-SIZMIN}{HSIZ}$	Number of size parameter increments between SIZMIN and SIZMAX
M	Number of bins in histogram
DELSIZ	Size parameter range corresponding to one bin
$NDIM = \frac{DELSIZ}{HSIZ}$	Number of size parameter increments in one bin
$DEL = \frac{DMAX-DMIN}{M}$	Diameter range, $\mu$ , corresponding to one bin
D(J); J=1,M+1	Diameters, $\mu$ , spaced at intervals of DEL from DMIN to DMAX
S(K); K=1,L	Size parameters spaced at intervals of HSIZ from SIZMIN to SIZMAX
A(I,J); I=1,2N; J=1,M	Mie functions averaged over DELSIZ, returned by subroutine INTEGS
AREF	Reference Mie functions averaged over DELBIG, returned by subroutine INTEGR
$Q(I,J) = \frac{A(I,J)}{AREF}$ ; I=1,2N; J=1,M	Unsymmetric scattering kernel matrix
AM(I,J); I=1,M; J=1,M	Symmetric scattering kernel matrix



Table A-1. Concluded

H(I,J); I=1,M; J=1,M	Smoothing matrix
R(I,J); I=1,M; J=1,M	Smoothed, symmetric kernel matrix (Note: This matrix is redefined in calculation of goodness-of-fit parameter.)
AR(I,J);BR(I,J)	Dummy matrices used to prevent destruction of R(I,J) in inversion and eigenvalue calculations. Inverse matrix is returned in place of AR; diagonalized matrix is returned in place of BR.
G(K);K=1,2N	Vector of input deconvolution ratios (DECRATS)
DG(K);K=1,2N	Vector of input imprecision estimates
EPPS(K); K=1,2N	Vector of residual errors
ERR	Norm of EPPS(K) vector
ERREL	Ratio of ERR to norm of G(K) vector
GAMO	Initial value of smoothing parameter
DELGAM	Smoothing parameter increment
EPST	Final value of smoothing parameter
EPS	Input constant used in accuracy check in Cholesky's matrix inversion routine
IER	Error parameter returned if loss of significant digits occurs in matrix inversion
F(I); I=1,M	Solution histogram (mole fraction in each bin)
FH(I); I=1,M	Unsmoothed solution histogram
AN	Normalization constant for F(I)
CN	Normalization constant for FH(I)
V(I); I=1,M	Solution imprecision bands
DELF(I); I=1,M	Temporary vector used, separately, in computation of FH(I) and in determination of goodness-of-fit parameters
GOOF A	Goodness-of-fit parameter based on propagation of residual error and on the logarithm of the ratio of the smoothing parameter to the geometric mean of all kernel eigenvalues
GOOF B	Goodness-of-fit parameter based on propagation of residual error and on geometric mean of the logarithms of the ratios of the smoothing parameter to each kernel eigenvalue

Table A-2. SIZFRED Inputs

<u>Card Number</u>	<u>Parameter</u>	<u>Columns</u>
1.	Name for plot cover sheet	1 through 16
2.	Title for plot and print-out	1 through 72
3.a)	Initial smoothing parameter GAMO	1 through 10
b)	Smoothing parameter increment DELGRAM	11 through 20
c)	Final smoothing parameter EPST	21 through 30
d)	Tolerance parameter used in determining step at which matrix inversion lost accuracy - EPS	31 through 40
4.a)	Initial size parameter - SIZMIN	1 through 10
b)	Light wavelength in microns - XLAM	11 through 20
c)	Size parameter increment - HSIZ	21 through 30
5.a)	Number of size parameter increments between minimum and maximum size parameters - L	1 through 4 Right Justified
b)	Number of scattering angles (excluding reference angle) at which data will be entered - N	5 through 8 Right Justified
c)	Number of size parameter increments in each size bin - NDM	9 through 12 Right Justified
6.a)	Deconvolution ratios G(I); I=1,2N	1 through 10
b)	Imprecision values DG(I); I=1,2N There are 2N cards of this type.	11 through 20
7.	Scattering angles (in degrees) THETA(I); I=1,N+1 There are N+1 cards of this type. The last card specifies the reference angle	1 through 10
8.a)	Minimum diameter plotted on histogram (microns)	1 through 10
b)	Scale factor for histogram	11 through 20

**Table A-3. Error Messages Generated by Subroutine Miefile**

<u>Flag</u>	
0	Everything is OK
1	Either the angle THETA was not found or the size parameters sought were larger than the largest size parameter in the files
2	The first size parameter was smaller than the smallest in the files
3	The correct angle and range of size parameters were found but the first size parameter did not coincide with any of the size parameters in the file
4	The correct angle, range of size parameters, and the first size parameter were found, but some other size parameter sought was not found in the file
5	Same as above, but the search continued into subsequent files
6	Same as above, but the search ran into the end of the tape

**Table A-4. Deconvolution Ratios and Input Imprecision Values Corresponding to the Standard Size Distribution Function (Shown in Fig. A-3)**

<u>DECRATS</u>	<u>Standard Deviations</u>
6.894	0.6
3.203	0.3
2.388	0.2
0.3657	0.04
0.4197	0.04
7.093	0.3
3.082	0.2
2.3805	0.2
0.5769	0.06
0.451	0.1

Relative Standard Deviation = 0.0722

**Table A-5. Deconvolution Ratios and Input Imprecision Values Corresponding to the Bimodal Size Distribution Function (Shown in Fig. A-4)**

<u>DECRATS</u>	<u>Standard Deviations</u>
9.157	0.9
3.566	0.4
2.672	0.3
0.3305	0.03
0.4224	0.04
9.723	0.9
3.578	0.4
2.721	0.3
0.5192	0.05
0.3325	0.03

Relative Standard Deviation = 0.0985

**Table A-6. Deconvolution Ratios and Input Imprecision Values Corresponding to the Center-Peaked Size Distribution Function (Shown in Fig. A-5)**

<u>DECRATS</u>	<u>Standard Deviations</u>
8.017	0.6
2.771	0.3
2.227	0.2
0.3744	0.04
0.4486	0.03
8.157	0.6
2.433	0.1
1.994	0.2
0.504	0.05
0.406	0.04

Relative Standard Deviation = 0.0767

**Table A-7. Deconvolution Ratios and Input Imprecision Values Corresponding to the Standard Size Distribution Function but Having 8.6-percent Error in DECRAT 1**

<u>DECRATS</u>	<u>Standard Deviations</u>
6.3	0.6
3.203	0.3
2.388	0.2
0.3697	0.04
0.4197	0.04
7.093	0.3
3.082	0.2
2.3805	0.2
0.5769	0.06
0.451	0.1

Relative Standard Deviation = 0.0745

**Table A-8. Original and Gaussian Distributed Deconvolution Ratios (Corresponding to the Standard Deviations in Table A-4)**

<u>DECRATS</u>	<u>Gaussian Distributed Vectors</u>
6.894	6.715
3.203	2.917
2.388	2.360
0.3657	0.3629
0.4197	0.4377
7.093	6.811
3.082	3.289
2.3805	2.207
0.5769	0.5281
0.451	0.3633

Relative Error Level = 0.0463

**Table A-9. Original and Gaussian Distributed Deconvolution Ratios  
(Corresponding to One-Half the Standard Deviations in  
Table A-4)**

<u>DECRATS</u>	<u>Gaussian Distributed Vectors</u>
6.894	6.805
3.203	3.060
2.388	2.374
0.3657	0.3643
0.4197	0.4287
7.093	6.952
3.082	3.185
2.3805	2.294
0.5769	0.5526
0.451	0.4072

Relative Error Level = 0.0231

## **APPENDIX B**

### **MEASUREMENT OF PARTICLE SIZES AND COMPLEX REFRACTIVE INDICES BY USE OF MIE SCATTERING TECHNIQUES**

(Presented at Smoke Symposium II, Harry Diamond Laboratory,  
Adelphi, Maryland, April 25 -26, 1978).

B. P. Curry, D. P. Weaver, and J. W. L. Lewis.  
ARO, Inc.

Recently, an experiment was carried out to determine the size distribution, number density, and chemical identity of particles present in the flow of the Arnold Engineering Development Center (AEDC)-von Kármán Gas Dynamics Facility (VKF) Tunnel F, a hypervelocity, arc-drive, intermittent-flow wind tunnel. This appendix describes the results of that experiment and the techniques used in the analysis. In addition, a procedure is described for obtaining the complex indices of refraction of particles at wavelengths at which these indices are uncertain.

Copper particles and/or tungsten particles were suspected to be present in the flow, since these materials comprise the electrodes between which the arc is struck. Also, iron particles might have been present because steel baffles and burst diaphragms were used. In addition, the expansion of the flow through the hypersonic nozzle was expected to produce condensation of both water vapor and nitrogen present in the ambient air. Although all of the particles were potential sources of the observed light scattering, subsequent analysis showed that the data could be explained in only two ways: (1) of single species present, only copper could explain the scattering data and (2) of dual species combinations, copper and tungsten with no more than 21-percent mole fraction (44-percent mass fraction) of tungsten present could explain the analysis of the chosen data point — which was in the middle of a 150-msec run. Later, chemical analysis of the mass loss from the electrodes during the entire run showed the overall mass fraction to be 50-percent tungsten. Analysis of other data points during the run is currently in progress. The tungsten/copper ratio is expected to change progressively during the run.

Figure B-1 shows the experimental configuration. The particle flow is from left to right at about  $10^5$  cm/sec speed. A pulsed argon ion laser ( $0.5145 \mu$  wavelength) polarized at 45 deg to the scattering plane illuminated the particles. A detector was located opposite the laser to monitor transmission, and two spectrometers were used to monitor scattered light. (During the course of the experiment it became obvious that spectrometers were unnecessary and that ordinary phototubes would work just as well.) A chopper was interposed in each scattering channel, the plan of which is shown in Fig. B-2. Each chopper was divided into groups of three segments. The first segment in each group was blank, to provide a marker pulse of unpolarized light. The second and third segments of each group consisted, respectively, of vertically and horizontally oriented polarizers. The chopper speed was such as to provide 10-msec time resolution. Thus, about 10 data points could be obtained during the "good flow"\* portion of each short run. The transmission data indicated that only single scattering was occurring during the good flow period, though multiple scattering clearly occurred prior to the establishment of the flow and after flow breakdown, as indicated by the nearly complete obscuration

---

\*The "good flow" period is defined by "smooth decline" of the tunnel pressure versus time.



of the transmitted light. Because of geometrical constraints imposed by the tunnel observation ports, the scattering angles used were, respectively, 146.5 deg with subtended angles of 2.65 deg, and 161.9 deg with subtended angles of 6.6 deg. Subsequent computer simulations have determined that better accuracy can be achieved by use of smaller subtended angles, and future experiments will be planned accordingly.

Average particle size, species identification, and size histograms were determined from various scattering ratios in order to avoid the difficulties associated with absolute intensity measurements involving unknown particle number density. The first of these ratios is the degree of polarization shown (for copper) for the two scattering channels in Figs. B-3 and B-4. The theoretical curves shown have been numerically integrated over the appropriate subtended angles. The experimental imprecision bands correspond to one standard deviation in the scattered intensities. Figures B-3 and B-4 eliminate much of the non-uniqueness in the determination of average particle size. In addition, the transmission data can be combined with the scattering data to provide "angular/extinction" ratios — shown in Fig. B-5 for a single polarization state of 146.5 deg. These ratios are proportional to the Mie phase functions for each separate polarization state.

These ratios are obtained experimentally as follows: (1) From the transmission data, one obtains the product of particle number density times extinction cross section times length over which scattering and absorption occur, (2) From the angular scattering data, one obtains the product of number density times scattering cross-section times length of scattering volume (determined entirely by the collection optics). The total length over which extinction occurs could only be estimated to lie between the nozzle exit diameter and the flow-field diameter obtained from method-of-characteristics calculations. The overlapping experimental imprecision bands shown in Fig. B-5 were thus obtained. For each particle species there are four different plots of the type shown in Fig. B-5. Comparison of these results with the results of the polarization analysis completely removes the non-uniqueness in the average size and shows that the average diameter is  $0.8 \pm 0.1$  micron. Using the calculated extinction cross section in conjunction with the transmission data shows the particle number density to be equal to  $2 \times 10^4 \text{ cm}^{-3} \pm 10$  percent. The limiting factor in average size determination is the accuracy with which the extinction length can be determined.

The above procedure was repeated for the other particle species, and all species except copper and tungsten were systematically eliminated. During this analysis, it became apparent that the degree of polarization is insensitive to the imaginary part of the refractive index but is very sensitive to the real part of the index of refraction, especially near the "rainbow angle" (which is not very sensitive to size). In contrast, the magnitude of the phase function plots is very sensitive to the imaginary index, but relatively

insensitive to the real part. Hence, the following procedure is proposed for determining unknown complex refractive indices of aerosols in the infrared spectral region:

1. With use of the visible wavelengths at which the refractive indices are known for a given aerosol species, the average size and size distribution histograms are determined (by the method to be described shortly.)
2. The real refractive index is iteratively determined by measuring degree of polarization in the infrared at angles near the suspected rainbow angle and by then adjusting the real index until polydisperse Mie calculations made with the previously determined particle sizes agree with the experimental data.
3. Similarly, the imaginary index is determined by adjusting it until the polydisperse Mie phase functions agree with the experimental results.

This procedure, while admittedly somewhat non-unique, should yield valuable information if it is judiciously applied.

Our procedure for determining particle size histograms is a modification of Twomey's constrained linear inversion procedure. Computer simulations, such as that of Fig. B-6, have shown that accurate deconvolutions can be obtained for a limited number of size bins by deconvolving ratios of angular scattered intensities in separate polarization states to the unpolarized 90-deg scattered signal. In Fig. B-6, the stated polydisperse distribution has been integrated over the size bins shown — the results being the dashed line histogram. The solid line histogram is the result of deconvolving computer simulated scattering measurements. The accuracy indicated requires subtended angles no larger than 1 deg. In addition, at the stated small refractive indices\* and the indicated forward scattering angles, no more than three bins could be deconvolved accurately. Larger indices and/or larger scattering angles permit more bin deconvolutions.

Because of the unavailability of a 90-deg reference channel, the experimental deconvolutions were obtained as follows: The angular scattering intensities for each angle and each polarization state were ratioed to the sum of the data taken at both angles and at both polarization states. These ratios were then used as inputs into the constrained linear inversion program, and the smoothing parameter was adjusted until the computed average diameter approximately equaled the average diameter determined previously. Computer simulation showed three-bin deconvolutions obtained in this fashion to be quite accurate. The four-bin deconvolutions proved to be marginal by Twomey's criterion

---

\*Deliberately chosen as a "worst case."

regarding the size of the smallest eigenvalue of the scattering kernel matrix relative to the magnitude of the square error. Nevertheless, as Fig. B-7 shows, the experimental deconvolutions are reasonable in comparison with the deconvolution of a computer-simulated polydispersion which yields about the same average diameter.

The limits of these techniques are currently being established at AEDC in a series of laboratory experiments and in other computer-simulation studies. All indications to date are that these techniques should prove to be a valuable tool in establishing aerosol size and optical property data.

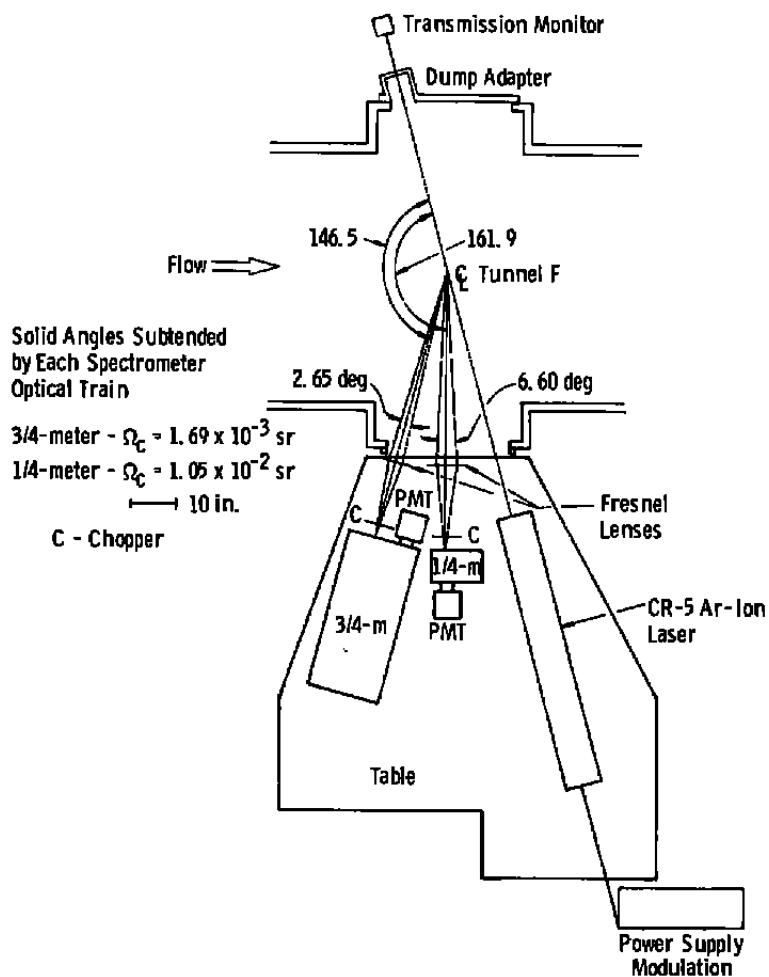


Figure B-1. Schematic diagram of apparatus placement.

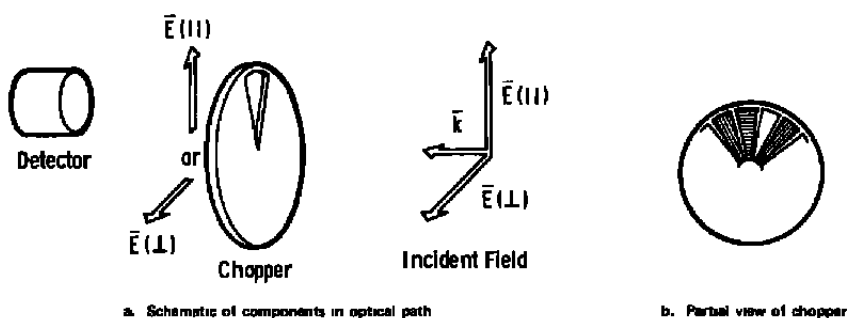


Figure B-2. Schematic of components in optical path.

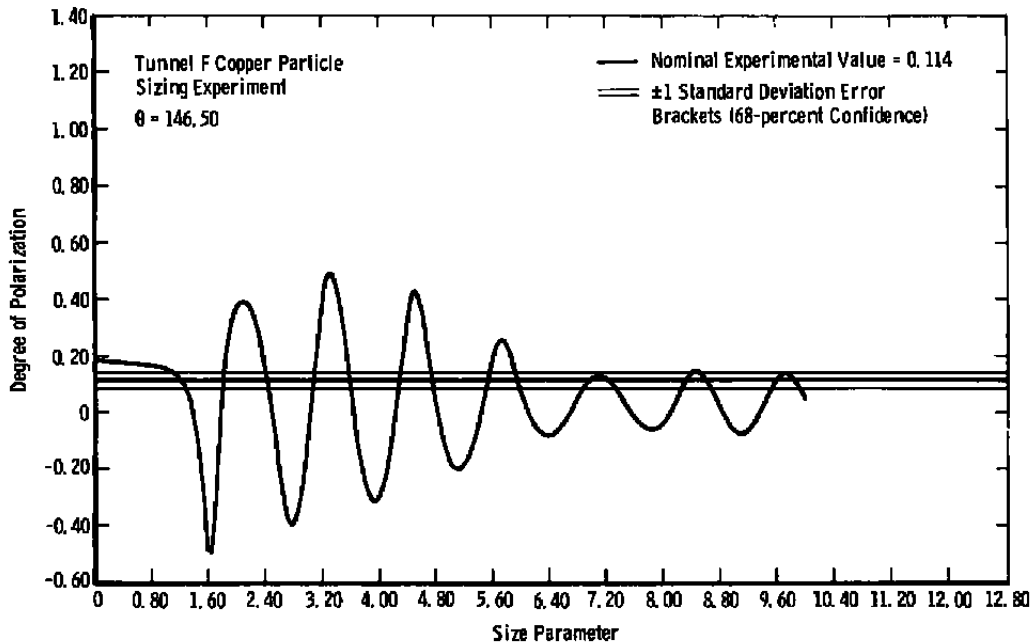


Figure B-3. Degree of polarization at 146.5 deg.

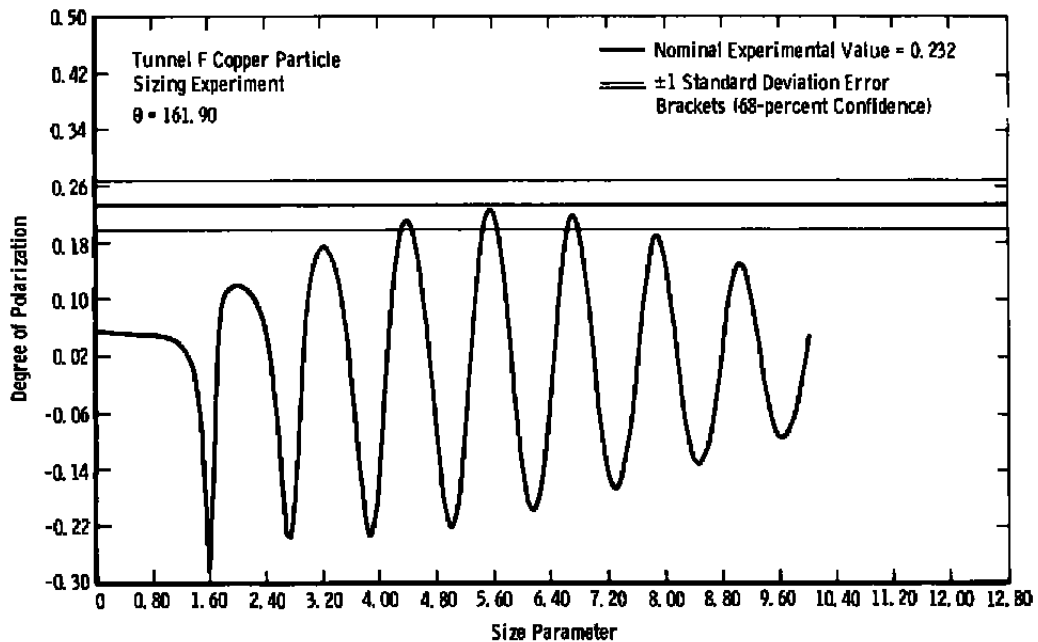


Figure B-4. Degree of polarization at 161.9 deg.

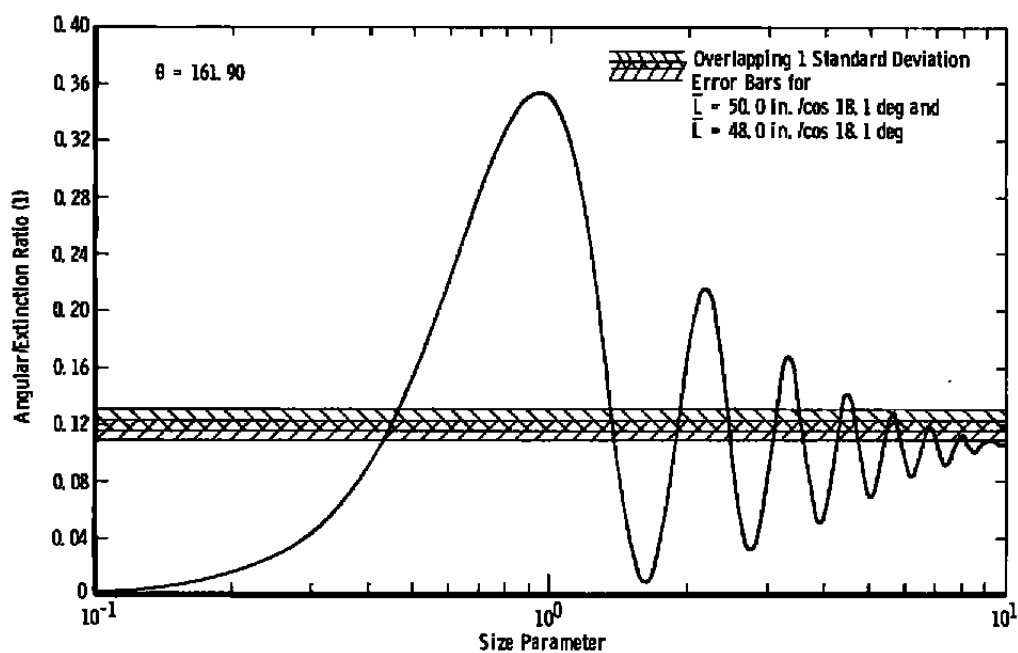


Figure B-5. Typical angular/extinction ratio plot.

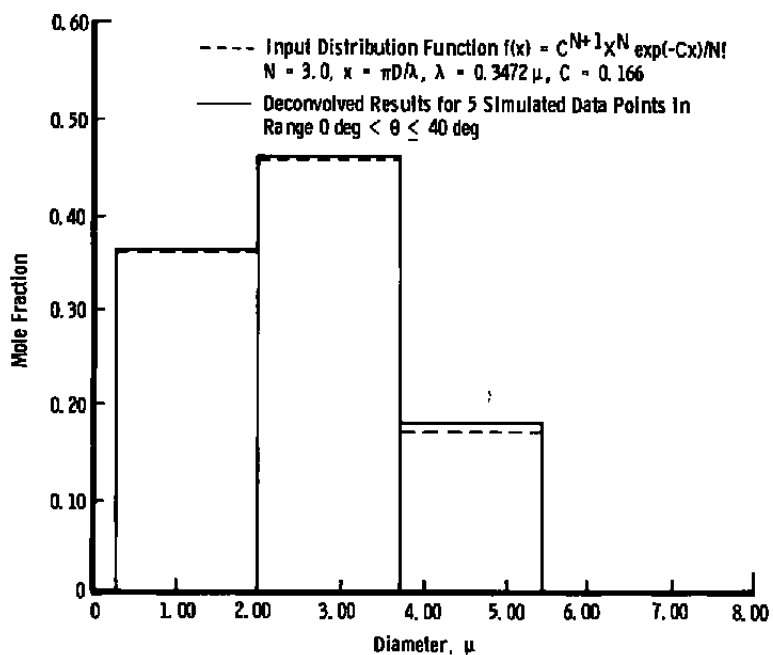
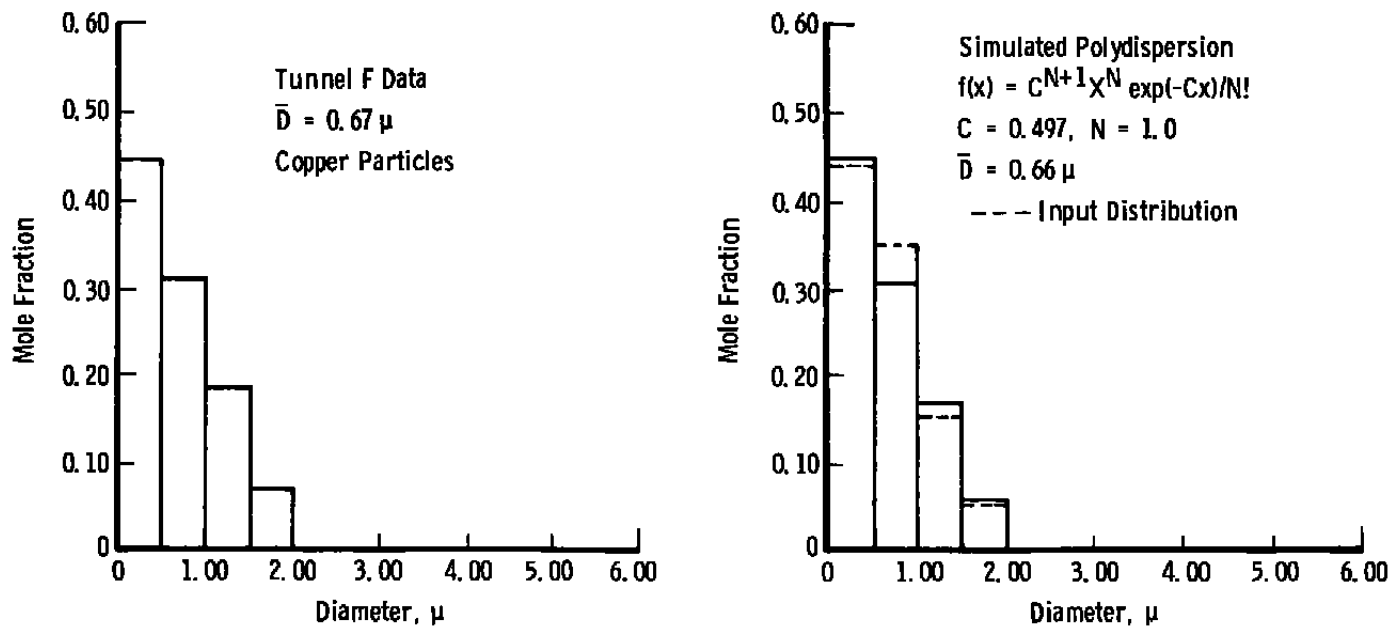


Figure B-6. Deconvolution of a simulated polydispersion.



**Figure B-7. Comparison of deconvolved sizing measurements with simulated polydispersion deconvolution.**

# **NOMENCLATURE** (For Main Text Only)

$A = \Phi_1(\theta_i, \psi_i)/\Phi_0$	Perpendicular scattering ratio for <i>i</i> th detector channel
$B = \Phi_2(\theta_i, \psi_i)/\Phi_0$	Parallel scattering ratio for <i>i</i> th detector channel
$D$	Particle diameter
$f(x)$	Normalized particle size distribution function, PSDF
$\tilde{I}$	Matrix defined in Eq. (19)
$i(x, \theta, \eta)$	Mie angular scattering intensity functions for particles of diameter <i>D</i> and complex refractive index
$\tilde{J}$	Matrix defined in Eq. (19)
$k = 2\pi/\lambda$	Propagation wave number of incident radiation
$L-1$	Number of subintervals in the size parameter interval $x_{min} \leq x \leq x_{max}$
$\tilde{L}$	Line-of-sight extinction distance in Eq. (3)
$\ell$	Scattering length of the focal volume [i.e., projection of the focal volume (subtended by the collection optics associated with any given detector) along the incident laser axis]
$M_1^{(k)}$	Function defined by Eq. (24)
$N$	Number of scattering angles at which measurements are made
$n$	Number density of particles (i.e., number of particles per unit volume)
$P$	Degree of polarization of scattered radiation [Eqs. (6) through (9)]
$P_{is}^{(k)}$	Function defined by Eq. (24)
$Q(x, \eta)$	Efficiency factor (dimensionless) for scattering, absorption, or extinction by particles of diameter <i>D</i> and complex refractive index $\eta = \eta_r - iK$



$R_{1,2}$	Angular/Extinction Ratios (ANGER functions) for perpendicular and parallel polarization states, respectively
$R_{B1,2}$	Angular/Backscattering Ratios (ANGBAR functions) for perpendicular and parallel polarization states, respectively
$T$	Ratio of transmitted radiation flux to incident flux
$\tilde{T}$	Matrix defined in Eq. (21)
$x = \pi D/\lambda$	Size parameter for particle of diameter $D$ (dimensionless)
$a$	Particle chemical species mole fraction
$\Delta\theta$	Range of scattering angles subtended by the collection optics of any given detector
$\Delta\psi$	Range of azimuthal angles subtended by the collection optics of any given detector
$\Delta\Omega$	Solid angle subtended by the collection optics of any given detector
$\delta$	Estimated imprecision in a measured quantity
$\epsilon$	Tolerance parameter used in multispecies average size determination
$\eta = \eta_r - i\kappa$	Complex refractive index of particles
$\eta_r$	Real (or dispersive) refractive index component
$\theta$	Polar scattering angle of spherical coordinate scattering geometry shown in Fig. 5
$\kappa$	Imaginary (or absorptive) refractive index component
$\lambda$	Wavelength of incident radiation
$\sigma$	Cross section for scattering, absorption, or extinction
$d\sigma/d\Omega$	Differential cross section per unit solid angle for scattering radiation into a particular direction specified by the infinitesimal solid angle $d\Omega$

$\Phi$	Scattered radiation flux into specified solid angle
$\Phi_0$	Indicent radiation flux
$\psi$	Azimuthal angle of spherical coordinate scattering geometry shown in Fig. 5
$\langle \rangle$	Denotes integration over specified subtended angular range
$\bar{\phantom{x}}$	Bar over a quantity denotes average (of unspecified weighting) over the particle size distribution function (PSDF)
$\{ \}$	Denotes a set of parameters

## SUBSCRIPTS

1	Pertains to quantities with polarization vector perpendicular to scattering plane
2	Pertains to quantities with polarization vector parallel to scattering plane
B	Pertains to directly backscattered radiation
i	Denotes specific angular scattering direction
s	Denotes particle chemical species
Tr	Pertains to transmitted radiation
U	Unpolarized

## SUPERSCRIPTS

exp	Denotes measured quantity after all calibration corrections have been applied
k	Denotes a particular set of size parameters, each element of which is associated with a given particle species
lo	Pertains to lower limit of experimental imprecision band
up	Pertains to upper limit of experimental imprecision band

j Denotes a particular set of experimental values of the degree of polarization, each element of which lies between the estimated imprecision limits of the scattering data from a given angular channel